Nano Research

Open Access

Review Article

Asymmetric diatomic electrocatalysts: Design, synthesis and applications

Yan Gao[1] ✉, Jinlong Ge[1], Tingting Chao[2], Jingjing Jiang[2], Yanmin Hu[3], Huishan Shang[4] ✉, and Xiangwen Liu[2] ✉

[1] AnHui Provincial Engineering Research Center of Silicon-Based Materials, Bengbu University, Bengbu 233030, China
[2] Institute of Analysis and Testing, Beijing Academy of Science and Technology, Beijing 100094, China
[3] Center of Advanced Nanocatalysis (CAN), Department of Chemistry University of Science and Technology of China, Hefei 230026, China
[4] School of Chemical Engineering, Zhengzhou University, Zhengzhou 450001, China

Cite this article: *Nano Research*, **2026**, *19*, 94908391. https://doi.org/10.26599/NR.2026.94908391

ABSTRACT: Asymmetric diatomic catalysts (ADCs) represent a promising class of sustainable electrocatalysts, featuring exceptional atom efficiency and dual active sites with asymmetric coordination environments. The asymmetric charge distribution in ADCs generates a local built-in electric field, enhancing charge separation/transfer and facilitating synergistic multi-step catalysis. This inherent structural complexity boosts catalytic performance by modulating the adsorption orientation and electronic configuration of intermediates. Importantly, the establishment of precise structure-activity correlations and the elucidation of underlying reaction mechanisms are of critical significance. This review provides a comprehensive overview of recent advancements in ADCs, with particular emphasis on classification methodologies, the application of artificial intelligence (AI), advanced characterization techniques, and their applications in key electrocatalytic reactions, such as oxygen reduction (ORR), oxygen evolution (OER), hydrogen evolution (HER), and carbon dioxide reduction (CO_2RR). Finally, the unresolved challenges and proposes potential research directions to advance the implementation of ADCs in energy systems are discussed.

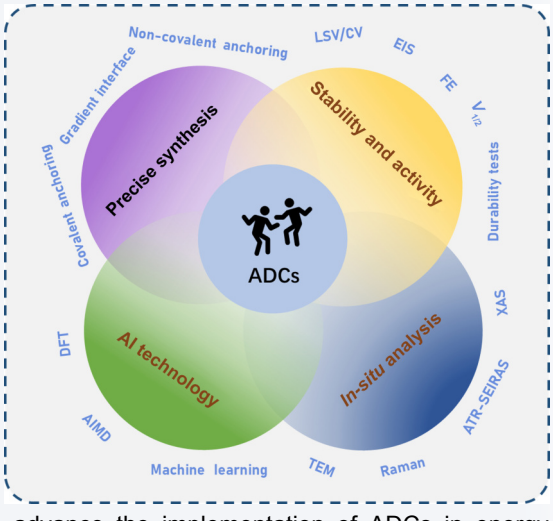

KEYWORDS: diatomic electrocatalysis, asymmetric charge distribution, structure-activity relationships, artificial intelligence

1 Introduction

The accelerating industrialization of society, heavily dependent on fossil fuels, necessitates sustainable energy conversion technologies [1–3]. Electrocatalysis offers a promising route, converting abundant molecules like CO_2, O_2, H_2O, and N_2 into value-added chemicals while mitigating fossil fuel reliance [4–7]. However, widespread deployment is hampered by dependence on precious-metal catalysts and sluggish reaction kinetics. Intensive research focuses on developing cost-effective, scalable alternatives [8–12]. Single-atom catalysts (SACs) represent a significant advance, offering maximized atom utilization and tunable, unsaturated coordination environments that enhance activity and selectivity for energy applications [13–25].

Asymmetric dual-atom catalysts (ADCs), extending the SACs concept, feature synergistic dual active sites that break adsorption energy scaling relationships, often surpassing SACs performance [26–31]. Compared to SACs, the core advantage of ADCs lies in their creation of a synergistic catalytic environment that achieves a "1 + 1 > 2" effect, enabling precise modulation of catalytic reactions at the atomic scale. Their unique electron redistribution and spatial proximity enable cooperative mechanisms that lower reaction barriers. The coordination of asymmetric dual-atom sites promotes local charge separation and charge transfer, which in turn facilitates flexible multi-electron pathways in electrocatalysis. In many reactions, a linear correlation exists between the adsorption

Received: November 4, 2025; **Revised:** December 24, 2025
Accepted: December 30, 2025

✉Address correspondence to Yan Gao, gaoyan@bbc.edu.cn; Huishan Shang, shanghs@zzu.edu.cn; Xiangwen Liu, liuxiangwen@bcpca.ac.cn

strengths of key intermediates on single-atom sites, imposing a fundamental constraint on the theoretical maximum catalytic activity. In contrast, the dual metal centers in asymmetric dual-atom catalysts (ADCs) can independently modulate the adsorption energies of different key intermediates. This capability allows them to break the linear scaling relationship and achieve an optimal adsorption balance, thereby significantly boosting the catalytic performance. ADCs, a distinct subclass of SACs, offer further advantages through their inherent structural asymmetry: (1) optimized electronic configurations via axial heteroatom doping or heterometallic coordination, tuning intermediate adsorption and lowering barriers; (2) enhanced synergy enabling activation of diverse intermediates and accelerated kinetics; (3) improved stability through direct diatomic bonding or bridging ligands suppressing migration; and (4) greater design flexibility via axial/lateral heteroatom coordination (e.g., N, O, S, and Cl) expanding beyond symmetric constraints. In short, the synergistic dual active sites in ADCs are designed to achieve precise control over local geometric configurations and electronic structures. This enables the optimization of complex multi-step reaction pathways, helps overcome the limitations of SACs, and holds strong promise for advancing green electrocatalysis applications.

As the structural core feature of ADCs, "asymmetric coordination" necessitates a clear structural description regarding the origin of the asymmetry (such as heteronuclear asymmetry, heteroatom doping, and spatial isomerism). Heteronuclear asymmetry represents the most intuitive asymmetry mode of ADCs, where two distinct metal atoms are bonded to surrounding atoms either via direct linkage or through bridging atoms. Due to differences in the types, electronegativity, and valence electron configurations of the two metal active sites, their "pulling forces" on the surrounding atoms differ, leading to an uneven charge distribution. Heteroatoms (such as N, O, S, P, B, etc.), due to their differing electronegativity, atomic radius, and electron-donating/accepting capabilities compared to C, can locally polarize the electron cloud around the metal center. Heteroatom doping creates a differentiated coordination environment for the metal active atom. For instance, S, with its distinct coordination behavior compared to N, can appropriately modulate the d-band center of the metal, making the adsorption energy for specific reaction intermediates (e.g., *OOH) closer to the optimal value, thereby enhancing the activity of ORR. For example, Chen and coworkers employed the reverse-micelle assembly-pyrolysis strategy to synthesize Cu_2-SNC catalyst with a uniquely asymmetrical coordinated CuN_2-CuNS site, which shows high ethanol selective in electrochemical CO_2RR [32]. Spatial isomerism can occur even when the central atom and the ligand types are identical, as differences in the three-dimensional spatial arrangement of ligands or the central atom may lead to molecular asymmetry. For example, Chen and coworkers employed a simple atomic printing strategy to synthesize non-coplanar Cu_2-C_2N, where Cu atoms share identical coordinating atoms, yet the asymmetry arises from the distinct spatial positions of the Cu atoms [33]. Heteroatom doping creates asymmetry in charge and energy levels at the chemical bonding level, while spatial isomerism generates asymmetry in position and orientation at the three-dimensional structural level. Heteronuclear asymmetry, heteroatom doping, and spatial isomerism can exist individually or simultaneously, collectively influencing the asymmetric configuration of ADCs. This meticulously designed asymmetry enables M_1 and M_1/M_2 from a simple summation of two independent single atoms into a functionally complementary and synergistically enhanced "active dimer", thereby achieving precise customization and significant enhancement of catalytic performance at the atomic scale.

Since the pioneering report of superior oxygen reduction reaction (ORR) activity on FeCo/N-C by Wang et al. in 2017 [34], ADCs research has rapidly expanded to encompass diverse heteronuclear (e.g., Fe-Sn, Fe-Ni, Fe-Mn, Fe-Co, Fe-Pt, Fe-Nb, Fe-Ru, Fe-Se, Fe-Cu, Co-In, Co-Zn, Co-Cu, Co-Ni) and homonuclear configurations (e.g., Cu_2 ADC, Fe_2 ADC, Co_2 ADC, Ni_2 ADC) (Fig. 1) [32, 35–56]. This diversity, stemming from varied synthesis strategies, supports, and precursors, yields distinct spatial configurations and catalytic properties, enriching yet complicating mechanistic understanding.

Atomically dispersed catalysts (ADCs) consist of two adjacent homonuclear or heteronuclear metal active atoms that enable

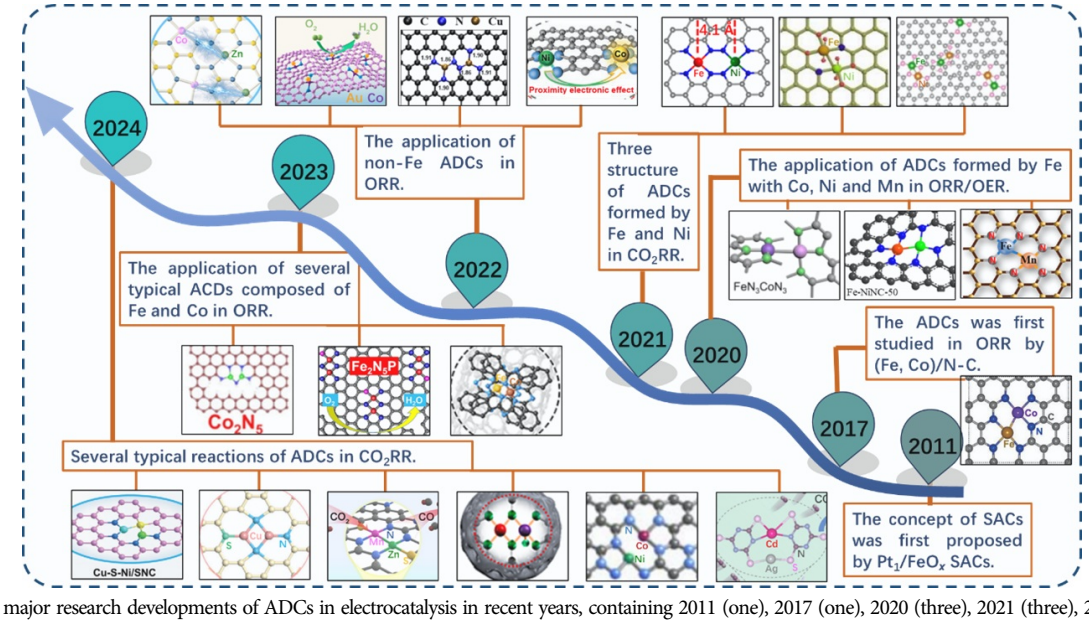

Figure 1 The major research developments of ADCs in electrocatalysis in recent years, containing 2011 (one), 2017 (one), 2020 (three), 2021 (three), 2022 (four), 2023 (three), and 2024 (six).

highly efficient and selective asymmetric electrocatalytic performance. These dual active sites are typically anchored to a stable support, forming a robust coordination structure that prevents metal atom migration or aggregation, thereby extending the catalyst's lifespan. Leveraging unique advantages, ADCs represent an emerging electrocatalysis frontier. This review explores ADCs development across three dimensions (Fig. 2) [35, 37, 57–62]: (1) asymmetric coordination design principles, (2) advanced characterization techniques, (3) electrocatalytic applications. We introduce a novel ADCs classification framework (homologous/heterologous systems; direct-bonded, single-bridged, double-bridged, multiatomic-interval structures). Synthesis-structure relationships for each type are analyzed, correlating methodologies with characterization data. ADC performance in key reactions of ORR, CO_2 reduction reaction (CO_2RR), oxygen evolution reaction (OER) and hydrogen evolution reaction (HER) is critically assessed, focusing on enhancement mechanisms. Finally, challenges and future research directions are outlined.

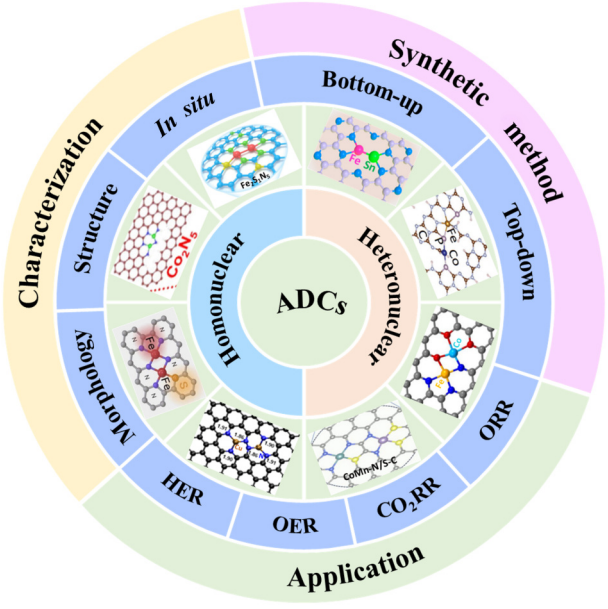

Figure 2 An overview of the main content for the review.

2 Classification of asymmetric diatomic catalysts

The rational classification of electrocatalysts is essential for elucidating the relationship between structure and properties. The identification of diatomic sites in asymmetric environments is particularly significant, as these sites can serve as potential active centers in electrocatalytic reactions. Based on the coordination type of diatomic sites, ADCs can be broadly categorized into homonuclear ADCs and heteronuclear ADCs (Fig. 3). Each category encompasses diverse bonding configurations, including direct metal-metal bonds, single non-metallic bridges, double non-metallic bridges, hybrid bridges and multi-atom-interval arrangements. The bridging non-metal atoms may be identical or distinct. Notably, for the formation of asymmetric coordination in M–M ADCs, it can be achieved either through the asymmetric coordination of non-metals or through the spatial isomerism of the two metal atoms. Additionally, the distance effect plays a crucial role, where the proximity of the two metals leads to synergistic interactions.

Based on the different coordination environments of bimetallic sites in homonuclear and heteronuclear ADCs, their specific structures can be categorized as follows (Fig. 4): (1) direct-linked by chemical bonds (A1 and B1). Structures such as FeSn-C_2N, SeFe-C_2N, A-$Fe_2S_1N_5$/SNC, FeCo-N-C, Fe/Cu-N-C, NiMn@V-g-C_3N_4, Cu/Ni-NC and others exemplify this category. (2) Single-bridged by one non-metal (A2 and B2). Examples include Cu-S-Ni/SNC, Co-N-Mn/NC, Hex-2Cu-O, FeCu-NC, Co_2-N-HCS-900 and so on. (3) Double-bridged by identical or different non-metals (A3 and B3). This motif is represented by structures like Cu_2-SNC, Fe_2-S_1N_5/SNC, $MnCoN_6$, CoFe-N-C, Fe,Mn/N-C, NiFe-DAC, RuFe-N-C, PtFe-DAC, FeNb/c-SNC, Fe/Cu-N-C DAC, CoIn-N-C, CoCu-DASC, FeCo-N_3O_3@C, etc. (4) Hybrid-linked by identical or different non-metals (B4). No cases of Hybrid link of homonuclear dual metal sites have been found so far. This motif is represented by structures like Fe-Mn-N-C, FeN_3O-CuN_4, NiFe-DASC, IrCo-N-C, FeAl-RNC, $FeMoN_6$, FeNi DASs/HOPSNC etc. Each structure may

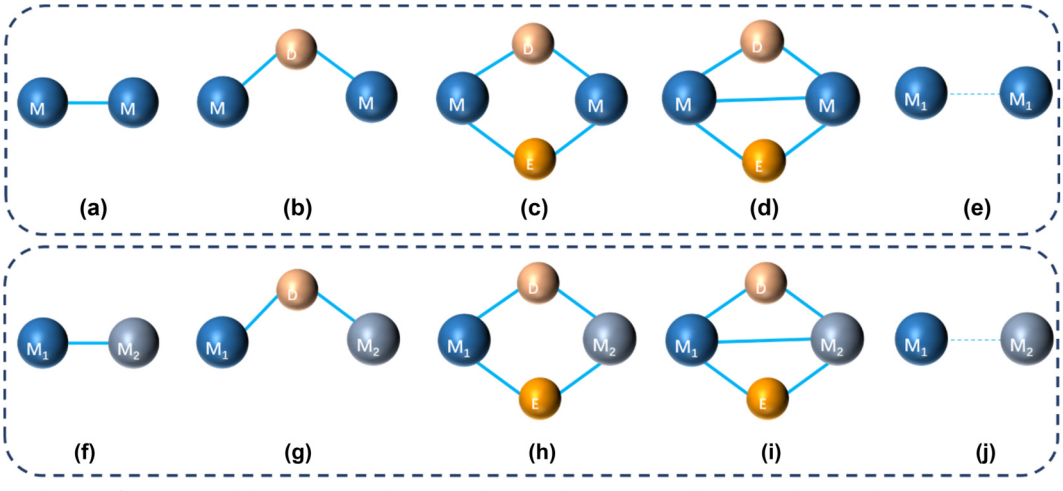

Figure 3 Schematic diagram of structure model in ADCs. (a)–(d) represent homonuclear ADCs, (e)–(h) represent heteronuclear ADCs. M, M_1 and M_2 stand for the metal atoms. D and E stand for the nonmetallic atom. Note the following instructions: (a) and (f) represent the direct formation of chemical bonds between metal-metal atoms. (b) and (g) represent a single bridge between metal-metal atoms via a non-metal. (c) and (h) represent double bridge between metal-metal atoms via identical or different non-metals. (d) and (i) represent the coexistence of double bridges and single bridges between metal-metal atoms. (e) and (j) represent metal-metal atoms are indirectly connected through three or more identical or different non-metals and that there is an asymmetric relationship between the two metals.

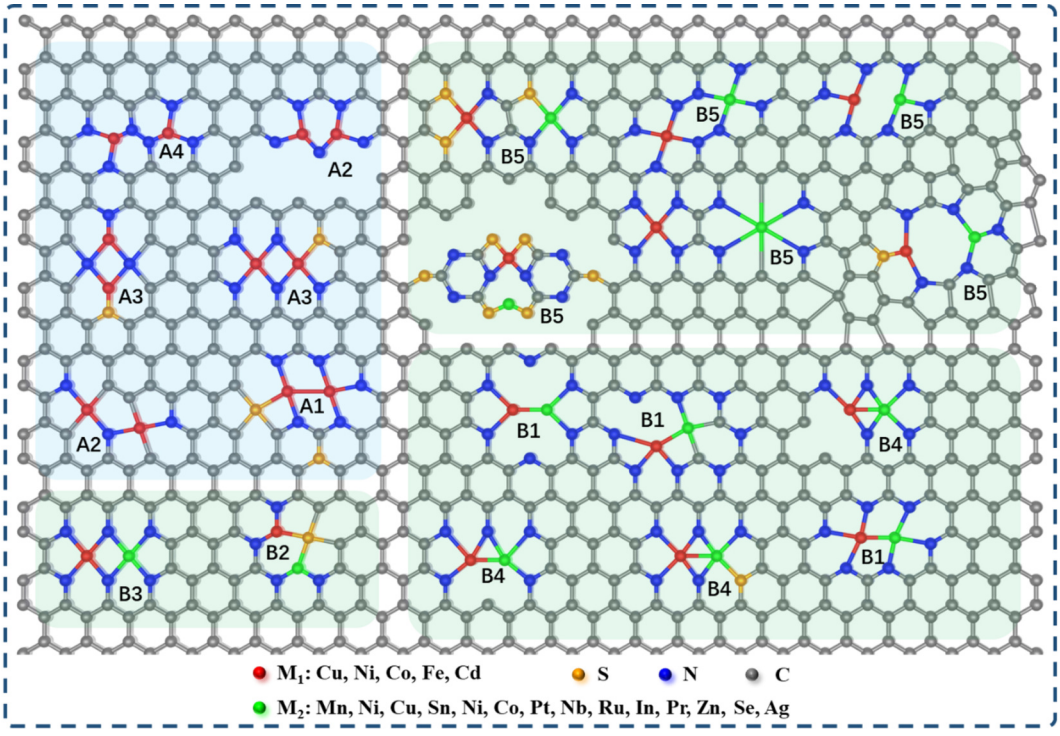

Figure 4 Schematic illustration for the possible structure of carbon-based ADCs. Typically, A1, A2, A3 and A4 represent homonuclear ADCs. B1, B2, B3, B4 and B5 represent heteronuclear ADCs.

also encompasses complex hybrid configurations. These include combinations of direct connections with single bridges [63] and direct connections with double bridges [46, 64–66]. Additionally, some catalysts feature a mixed presence of asymmetric diatomic sites and isolated single atomic sites [67, 68]. (5) Not directly connected, separated by two or more non-metallic bridges (A4 and B5). Structures falling into this category comprise Fe,Cu DAs-NC, Fe_1-Ni_1-N-C FeRu-N-C, Cu-Co/NC, Fe-Co DSAC, Co/Fe-SNC800, ZnCo-NC-II among others.

Table 1 summarizes the asymmetric reaction mechanisms of ADCs with different connection types. The distance between metal atoms in the direct connection is within the range of 0.23 to 0.27 nm, which is close to the distance of a metal bond or a strong coupling. Strong coupling promotes the co-adsorption and coupling of multiple intermediates. The difference in electronegativity of heteronuclear metals, the different non-metallic ligands of homonuclear metals, and the spatial isomerism of the bonds all contribute to the asymmetry. They mainly achieve the direct orbital overlap of heteronuclear metals through the hybridization of the d orbitals. The newly formed bonding/antibonding orbitals significantly alter the electronic state density of the metal centers and the difference in electronegativity of the coordinating atoms in homonuclear metals, thereby influencing the asymmetric distribution of intermetallic charges. The distances between metal atoms in single-bridge connection are significantly greater than those in the direct connection, ranging from 0.32 to 0.50 nm. The specific distances between metal atoms are determined by the bond angles of the single bridges (M_1–X–M_1/M_2). The fundamental cause of the asymmetry still depends on the electronegativity of the metal centers and the coordinating atoms, as well as the spatial isomerism. The bridge-atoms can conduct electron transfer, regulate the spin state of the metal centers, and optimize the adsorption energy of the intermediate species. The double-bridge connection through the double-electron channels enhances the cooperative effect between metal centers, which belongs to strong electronic coupling. The distance between metal atoms is 0.24 to 0.29 nm, which is shorter than that of a single bridge and is close to the configuration of direct connection. The rigid ring-like structure formed by two bridges precisely fixes the adsorption configuration of reaction intermediate, facilitating the specific pathway. The mixed connection is usually a combination of direct connection with single bridge or double bridge. The specific bridging creates a local microenvironment that enables two metal centers to assume different roles, thereby achieving cooperative catalysis. The mixed connection makes the metal centers more closely linked and the bond lengths shorter, within the range of 0.23 to 0.27 nm. The multi-atom intervals are weakly electronically modulated through conjugated π systems or space charge transfer to form long-range electronic communication. The distance between two metal centers is relatively far, ranging from 0.4 to 0.6 nm. The coordinating atoms of metal centers are often independent of each other, and the isolated space helps to catalyze different steps of multi-step reactions separately, avoiding interference from intermediates. Despite significant advances in ADCs, the inherent complexity and variability of their structures, spatial configurations, and vacancy defects present substantial challenges for precise synthesis and effective electrocatalytic application. Thus, further comprehensive investigation is imperative to address these challenges.

3 Synthetic methods of ADCs

ADCs exhibit a more complex and asymmetric coordination structure compared to symmetrical diatomic catalysts, posing greater challenges in precisely controlling the spatial distribution of diatomic sites [91]. To develop rational and controllable

Table 1 Summary of different connection types and of asymmetric mechanism ADCs

Structure type	Bonding method	Distance of metals (nm)	Specific example	Coordination environment	Application	Asymmetric mechanism	Ref.
Direct-link	M_1–M_1/M_2	0.25–0.26	FeSn-C_2N	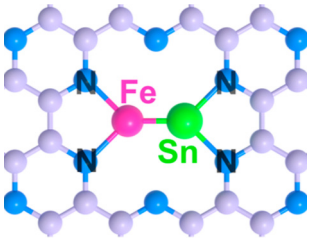	ORR		[59]
		0.22–0.23	SeFe-C_2N	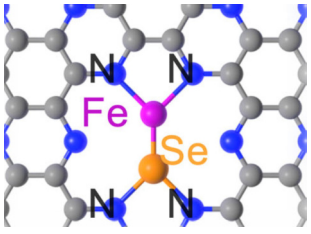	ORR		[5]
		~ 0.25	A-$Fe_2S_1N_5$/SNC	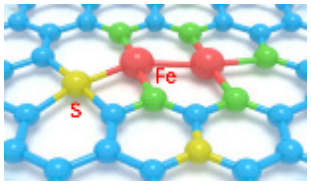	OER		[57]
		~ 0.263	FeCo-N-C	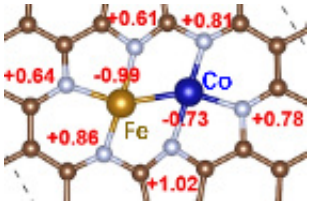	ORR/OER	The difference in electronegativity of heteronuclear metals, the different non-metallic ligands of homonuclear metals, and the spatial isomerism of the bonds all contribute to the asymmetry.	[69]
		0.26	Fe/Cu-N-C	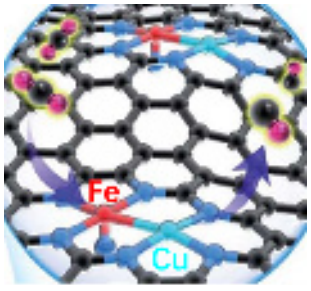	CO_2RR		[70]
		0.233	NiMn@V-g-C_3N_4	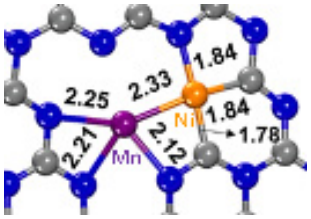	CO_2RR		[71]
		0.26–0.27	Cu/Ni-NC	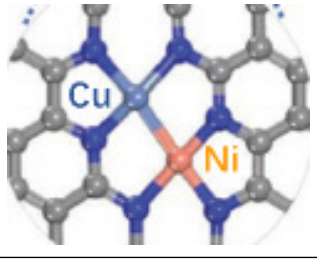	CO_2RR		[72]

(Continued)

Structure type	Bonding method	Distance of metals (nm)	Specific example	Coordination environment	Application	Asymmetric mechanism	Ref.
		~ 0.32	Cu-S-Ni/SNC	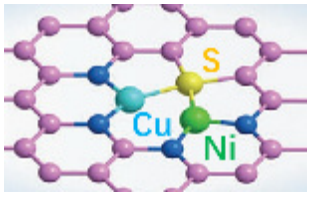	CO_2RR		[52]
		0.356	Co-N-Mn/NC	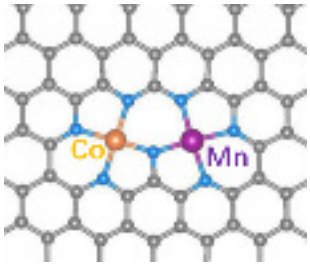	ORR		[73]
Single-bridge	$M_1–X–M_1/M_2$	0.371	Hex-2Cu-O	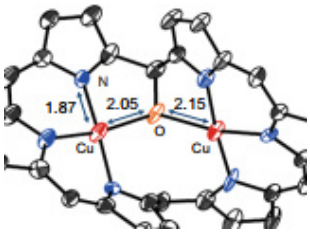	CO_2RR	The spatial distortion of the bonds, heteronuclear metals leads, and homonuclear metals with different coordinating atoms leads to asymmetry.	[74]
		—	FeCu-NC	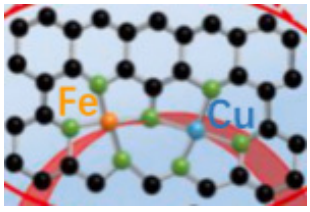	ORR		[75]
		0.30–0.50	Co_2-N-HCS-900	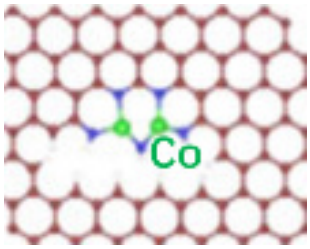	ORR/OER/HER		[37]
Double-bridge	$M_1–X_2–M_1/M_2$	0.289	Cu_2-SNC	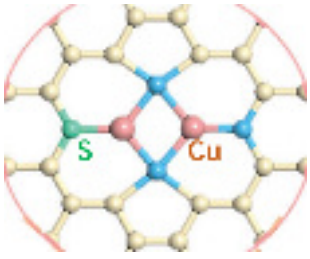	CO_2RR	Double-bridge enhanced asymmetric orbital coupling compared with single-bridge.	[32]
		0.246	Fe_2-S_1N_5/SNC	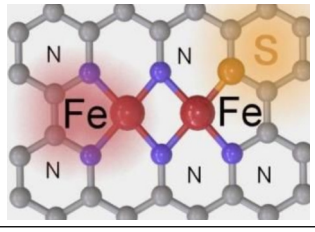	ORR		[58]

(Continued)

Structure type	Bonding method	Distance of metals (nm)	Specific example	Coordination environment	Application	Asymmetric mechanism	Ref.
		~ 0.25	$MnCoN_6$	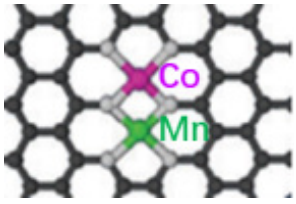	ORR		[76]
		0.258	CoFe-N-C	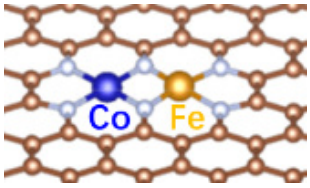	ORR/OER		[77]
		0.25 ± 0.02	Fe,Mn/N-C	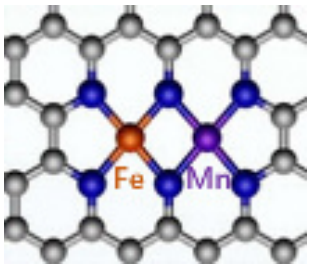	ORR		[78]
		~ 0.27	NiFe-DAC	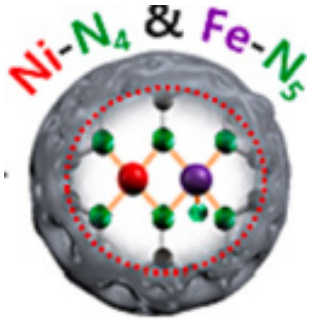	CO_2RR		[54]
		0.237	RuFe-N-C	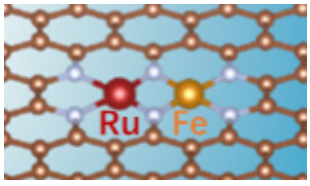	ORR/OER		[79]
		0.257±0.067	PtFe-DAC	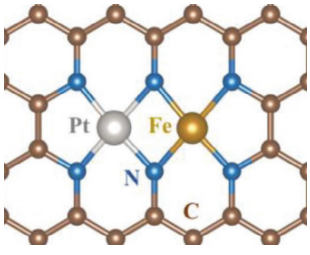	ORR		[80]
		0.26	FeNb/c-SNC	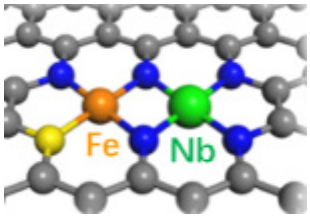	ORR		[81]

(Continued)

Structure type	Bonding method	Distance of metals (nm)	Specific example	Coordination environment	Application	Asymmetric mechanism	Ref.
		0.272	CoIn-N-C	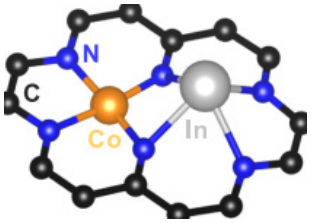	ORR		[82]
		0.24–0.25	CoCu-DASC	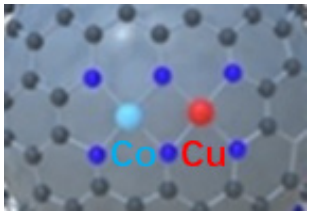	CO_2RR		[83]
		~ 0.25	FeCo-N_3O_3@C	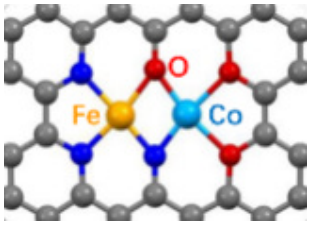	ORR/OER		[61]
		~ 0.24	Fe-Mn-N-C	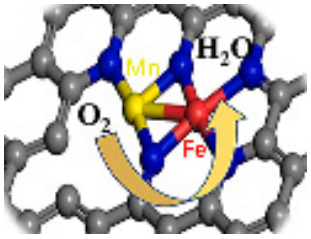	ORR		[64]
		~ 0.24	FeN_3O-CuN_4	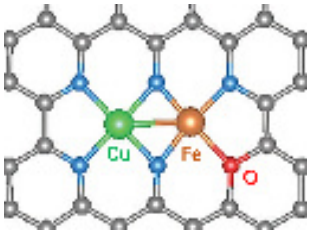	ORR		[65]
Hybrid-link	M_1–X–Y–M_1/M_2	~ 0.24	NiFe-DASC	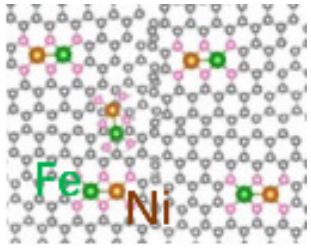	CO_2RR/OER	The mixed bridging atoms generate an asymmetric coordination environment.	[46]
		~ 0.23	IrCo-N-C	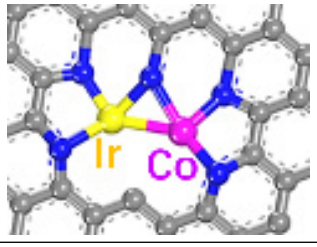	ORR/OER		[63]

(Continued)

Structure type	Bonding method	Distance of metals (nm)	Specific example	Coordination environment	Application	Asymmetric mechanism	Ref.
		~ 0.23	FeAl-RNC	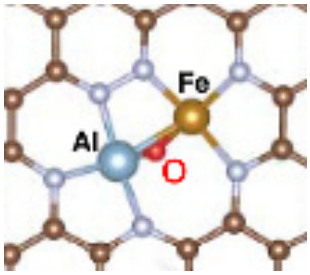	ORR		[84]
		~ 0.27	$FeMoN_6$	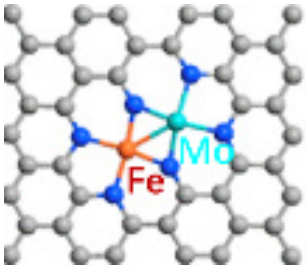	ORR		[66]
		0.25 ± 0.003	FeNi DASs/HOPSNC	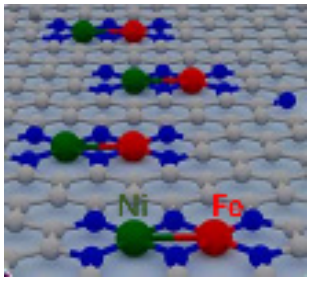	CO_2RR		[85]
		0.41	Fe,Cu DAs-NC	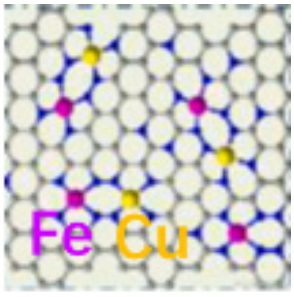	ORR		[86]
Multi-atom-interval	$M_1…(X_n)…M_1/M_2$	~0.41	Fe_1-Ni_1-N-C	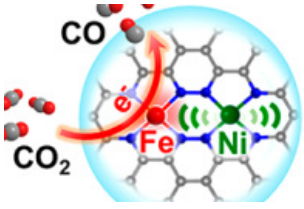	CO_2RR	Asymmetry is generated by long-range electronic coupling or spatial coordination.	[44]
		0.405	FeRu-N-C	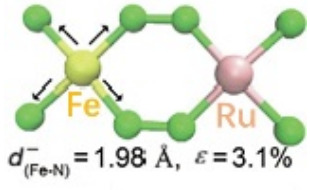	ORR		[87]

(Continued)

Structure type	Bonding method	Distance of metals (nm)	Specific example	Coordination environment	Application	Asymmetric mechanism	Ref.
		~ 0.5	Cu-Co/NC	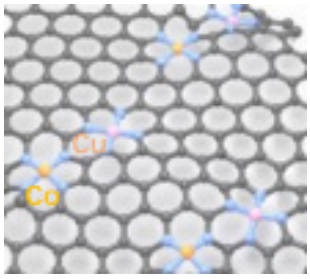	ORR/OER		[88]
		~ 0.5	Fe-Co DSAC	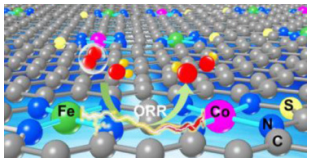	ORR		[89]
		0.3–0.6	Co/Fe-SNC800	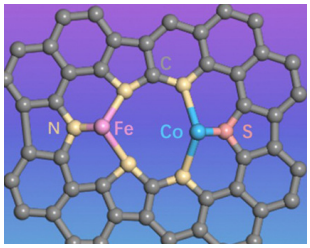	OER		[90]
		0.532	ZnCo-NC-II	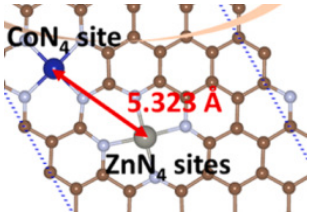	ORR		[47]

experimental synthesis techniques, it is crucial to address the aggregation of atoms at dual sites while ensuring the stability of asymmetric configurations. Efficient synthetic pathways can facilitate the regulation of asymmetric diatomic site positions and enhance the interaction between metal species and supports. Wang and colleagues, for instance, have pointed out that isolated single-atom sites (SASs) lack sufficient adsorption centers, while well-designed dual-atom sites (DASs) featuring two active centers can enhance adsorption capacity and thus accelerate reaction coupling steps (Fig. 5) [92]. First, two adjacent metal active centers with asymmetric coordination environments can achieve an optimized electronic structure through long- or short-range electron coupling, thereby modulating the adsorption interactions between the dual-atom sites and key reaction intermediates. Subsequently, these neighboring active sites cooperate to adsorb, bind, and convert intermediates efficiently—lowering the reaction energy barriers and facilitating intermediate coupling. Although recent years have seen rapid advances in the precise synthesis of DASs, their rational design and efficient preparation remain significant challenges.

Synthesis methods for ADCs encompass both bottom-up approaches (e.g., coordination anchoring [49, 93], co-precipitation [94], atomic layer deposition [95–98], impregnation [75]), and top-down strategies (e.g., pyrolysis [34, 99–102] and ball milling [103]). Bottom-up synthesis involves directly anchoring metal precursors onto carriers to form dispersed atomic sites, enabling gradually and precisely assemble the target product at atomic level and thus being more suitable for the precise control design of asymmetric double-site electronic structures. The bottom-up approaches typically utilize pre-designed "anchor sites" (such as nitrogen-doped vacancies, individual holes, specific functional groups) on substrates (such as graphene, MOFs, COFs) to stepwise "install" the target metal atoms at the designated positions. Furthermore, by controlling the spatial relationship between two anchor sites, the distance and relative orientation between the two asymmetric metal atoms can be precisely determined, thereby determining the degree of orbital overlap and the strength of electron coupling. In the bottom-up synthesis approach, the local structure of the carrier (such as the arrangement of atoms like C, N, O, S) is meticulously designed to serve as a "solid ligand" for metal atoms. By precisely controlling the type (e.g., N/O/S), quantity (e.g., pyridine N/graphitic N) and geometric configuration (e.g., planar/pleated) of doped atoms, it directly influences the electron density, d-band center position and frontier orbital distribution of asymmetric metal active centers. Introducing templates, steric hindrance agents or conducting post-treatment (such as mild pyrolysis) during the bottom-up synthesis process can immobilize the metal atoms while shaping the carbon layer structure, porosity and hydrophilicity/hydrophobicity around them. This modulation of the

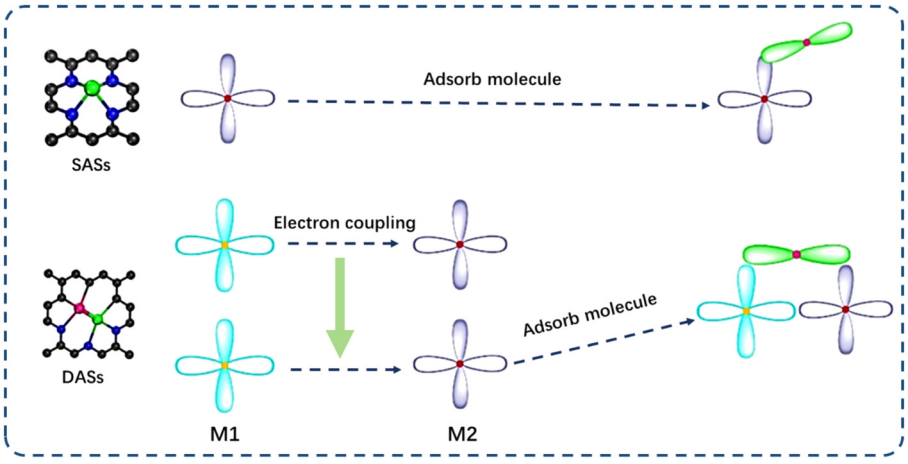

Figure 5 The electronic coupling process of DASs and SASs by a specific tailoring the binding mode. Reproduced with permission from Ref. [92], © Tsinghua University Press 2024.

microenvironment also affects the mass transfer, reactant enrichment and intermediate stabilization during the reaction process, thereby indirectly yet profoundly influencing the catalytic electronic behavior exhibited by the catalyst. In conclusion, the bottom-up synthesis approach achieves the "programmable construction" of catalytic active sites starting from the atomic level by precisely controlling the spatial configuration and customizing the coordination microenvironment. In contrast, top-down synthesis entails decomposing metal particles or clusters into dispersed atoms via physical or chemical means and stabilizing them on supports. In the top-down synthesis approach, the initial bulk precursors (e.g., alloys, metal-organic frameworks) typically exhibit a high metal content. Theoretically, if all the metal species in these precursors could be completely converted into single-atom active sites, an exceptionally high loading capacity would be attainable in ADCs. However, synthetic catalysts via top-down methods often feature non-uniform active phases despite their high metal content. The "high loading" in this context probably refers to the coexistence of a heterogeneous mixture of species, including single atoms, mononuclear and heteronuclear diatomic moieties, clusters, and nanoparticles. Notably, the majority of these species are likely to be ineffective or low-efficiency metal aggregates, indicating that "high loading" does not equate to "high active site density". Moreover, the randomness of the top-down preparation process results in low reproducibility of the synthesized catalysts. This lack of reproducibility hinders the establishment of accurate structure-performance relationships and prevents the utilization of the unique, precisely tunable electronic structure of ADCs. Consequently, the top-down synthesis method primarily serves as an exploratory and proof-of-concept supplementary strategy. It may occasionally yield the target structures in specific systems (e.g., certain layered precursors), but is not an ideal model for investigating precise catalytic mechanisms. Furthermore, it faces substantial challenges in being scaled up as an industrial catalyst with predictable performance.

3.1 Homonuclear ADCs

Research on homonuclear ADCs remains relatively scarce, largely due to the significant challenges in identifying homonuclear active sites within diverse coordination environments. These catalysts, even with pure nitrogen coordination, can achieve structural asymmetry through spatial configuration adjustments. For instance, Cu_2-C_2N exemplifies an asymmetric homonuclear structure formed by direct chemical bonding between dual Cu atoms [33]. The asymmetric structure Cu_2-C_2N synthesized by leveraging the edge N atoms in the layered 2D network C_2N cavity as anchoring "pincers" to capture metal atoms (Fig. 6(a)). The stable dual-Cu sites, confirmed by an interatomic distance of ~ 2.32 Å (Fig. 6(b)), exhibit an asymmetric coordination geometry where the two Cu atoms reside above and below the molecular plane, despite identical N_2 coordination (Fig. 6(c)). This atomic configuration, probed by hard X-ray absorption fine structure (XAFS) including X-ray absorption near-edge structure (XANES) and extended X-ray absorption fine structure (EXAFS) analysis, facilitates C–C coupling during CO_2RR, achieving high guarantees $FE_{C_{2+}}$ (90.8%) and $FE_{C_2H_4}$ (71.7%) at 1.10 V vs RHE.

Recent advances demonstrate precise synthesis of asymmetric homonuclear dual-atom catalysts (DACs). Chen and co-workers ingeniously engineered Fe_2-S_1N_5/SNC catalysts featuring double N-bridges [58]. The researchers first constructed a special core-shell structure on the metal precursor of a specific compound Bis(dicarbonylcyclopentadienyliron) (CDD) containing Fe diatom, and then precisely constructed an asymmetric homonuclear DAC with N and S coordination on the hollow structure formed by pyrolysis of the core-shell structure. The optimized pyrolysis process in the preparation ensures the complete elimination of the CDD derived organic ligands, while simultaneously preventing the accumulation of the Fe diatoms. The doping of non-metals produces more defects, which provides more possibilities for Fe double anchoring. The main elements of the catalyst are uniformly dispersed throughout the sample. The resulting Fe_2-S_1N_5/SNC catalyst displayed remarkable stability and superior catalytic performance in ORR. The same group also synthesized a directly linked Fe-Fe homonuclear catalyst, *A*-$Fe_2S_1N_5$/SNC, with an N-C-N bridge via a two-step pyrolysis and carbonization approach [57]. While both Fe_2-S_1N_5/SNC and *A*-$Fe_2S_1N_5$/SNC share Fe_2 active centers coordinated by N/S, their distinct micro-coordination environments lead to divergent catalytic behaviors (e.g., *A*-$Fe_2S_1N_5$/SNC excels in OER). Similarly, the asymmetric Cu_2-SNC catalyst (CuN_2-CuNS coordination), synthesized via reverse-micelle-assembly-pyrolysis, exhibits high ethanol selectivity in CO_2RR [32].

Further examples highlight the role of heteroatom coordination in asymmetry. The synthesis process of two other Fe diatomic ADCs was shown in Figs. 6(d) and 6(e) [36, 50]. The synthesis

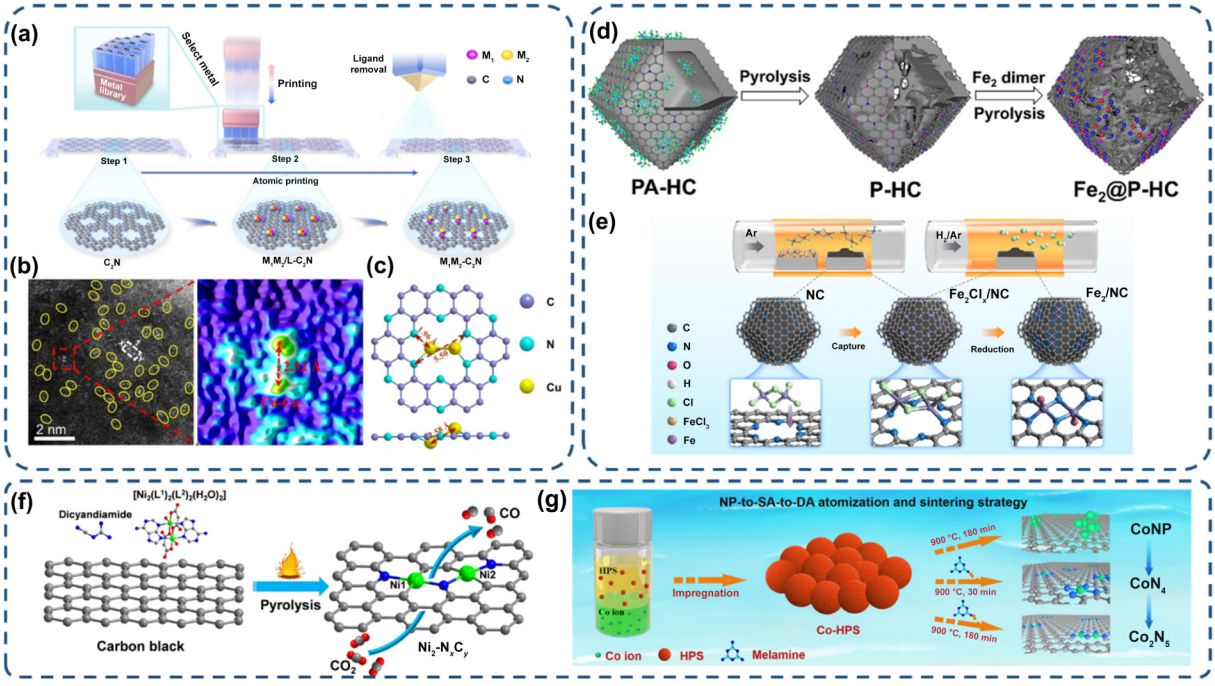

Figure 6 (a) Schematic illustration of the synthesis of the Cu_2-C_2N. (b) The enlarged HAADF-STEM image shows the dual atoms (yellow circles) dispersed in the C_2N substrate and the intensity profiles highlighted along the red circle. (c) Top and side views of the atomic interface structure model for Cu_2-C_2N. Reproduced with permission from Ref. [33], © Wiley-VCH GmbH 2024. (d) Schematic illustration for the two-step pyrolysis synthesis of the Fe_2@P-HC catalyst from PA-NC. Reproduced with permission from Ref. [50], © American Chemical Society 2023. (e) Schematic illustration of Fe_2/NC ADC catalyst by a sublimation transformation strategy. Reproduced with permission from Ref. [36], © Wiley-VCH GmbH 2024. (f) Schematic illustration of the one-step pyrolysis strategy for the fabrication of Ni_2-N_xC_y catalysts. Reproduced with permission from Ref. [104], © Wiley-VCH GmbH 2022. (g) Schematic diagram of CoSA-N-HCS-900 by the atomization and sintering strategy. Reproduced with permission from Ref. [37], © Wang, X. K. et al. 2023.

process of an asymmetric dual-atomic iron catalyst with N/P coordination in Fe_2@P-HC (Fig. 6(d)) [50]. The catalyst shares a similar double bridge structure with the previously described catalyst Fe_2-S_1N_5/SNC, which is formed through the same nonmetal-N linkage. The difference is that the formation of the dual-atom asymmetric coordination structure Fe_2N_5P of the catalyst Fe_2@P-HC is achieved through N and P coordination. The precursor of the catalyst Fe_2@P-HC was obtained by impregnation and adsorption of the metal precursor of cyclopentadienyl iron dicarbonyl dimer (Fe_2 dimer) on the P-HC obtained from the carbonization of COF@MOF. Then, the Fe_2@P-HC catalyst is finally obtained by pyrolyzing the precursor of loaded Fe_2 dimer. Despite sharing a double N-bridge motif with Fe_2-S_1N_5/SNC, the P-coordination in Fe_2@P-HC significantly enhances its ORR activity ($E_{1/2}$ = 0.89 or 0.75 V vs. RHE in alkaline or acidic media, respectively). The density functional theory (DFT) calculations revealed that the asymmetric Fe_2N_5P sites lower the free energy change (ΔG) for the O_2 to *OOH conversion (rate-determining step) compared to symmetric Fe_2N_6 sites (0.37 vs. 0.48 eV), explaining its superior activity. Fe_2/NC (Fig. 6(e)) was formed via a sublimation-transformation strategy using $FeCl_3$ on ZIF-8-derived N-doped carbon (NC) with high N-content (~ 10%) [36]. This catalyst possesses an asymmetric structure stabilized by double N-bridges and axial O-coordination on the Fe_2 site. Its simple synthesis using inexpensive precursors yields an outstanding ORR catalyst ($E_{1/2}$ = 0.90 V vs. RHE in 0.1 M KOH), demonstrating the strategy's universality. The differing fine structures and ORR performances of Fe_2@P-HC and Fe_2/NC underscore the critical influence of precursors, supports, and synthesis conditions.

Beyond Fe-based catalysts, temperature-controlled one-step pyrolysis of a dinuclear Ni complex precursor yielded Ni_2-N_xC_y catalysts (Ni_2N_7, $Ni_2N_5C_2$, and $Ni_2N_3C_4$) (Fig. 6(f)) [104]. Among these, $Ni_2N_3C_4$ exhibited the highest CO_2RR activity for CO production (FE_{CO} = 98.9% at −0.88 V vs. RHE). Its optimal performance stems from a unique coordination involving a double C-bridge (indirect) and a single N-bridge (direct). Finally, an atomization-sintering strategy enabled the controlled synthesis of Co_2N_5 on N-doped hollow carbon spheres (CoSA-N-HCS-900, Fig. 6(g)) [37]. This approach facilitated the evolution from Co nanoparticles to single atoms and finally to asymmetric homonuclear diatomic sites. The Co_2N_5 structure, featuring both an N-C-N indirect bridge and a direct N-bridge, promotes charge transfer between Co atoms and stabilizes the asymmetry. The short Co-Co distance (~ 0.12–0.25 nm) and the low-spin state of Co_2N_5 optimize the adsorption/desorption of O* and H* intermediates, endowing the catalyst with exceptional multifunctional activity for ORR, OER, and HER.

3.2 Heteronuclear ADCs

ADCs have garnered significantly more research attention and exhibit greater diversity in synthesis methodologies compared to their homonuclear counterparts, reflecting the broader scope for tailoring active sites [27, 29, 105]. Extensive investigations have focused on their synthesis and structure-performance relationships. Heteronuclear ADCs can be classified into three structural types: direct metal-metal bonding, non-metal bridged structures, and non-bridged asymmetric pairs.

Direct metal-metal bonding is a prominent strategy involves forming direct chemical bonds between heteronuclear metal pairs. For example, Wang and co-workers synthesized SeFe-C_2N via a

multi-step pyrolysis approach [5]. Pre-C_2N with well-defined N_6 cavities was first formed from cyclohexanone and urea/$MgCl_2$, followed by acid washing. Sequential introduction and pyrolysis of SeO_2 (yielding Se-C_2N) and then Fe^{3+} precursors anchored the SeFe pairs within the cavities (Fig. 7(a)). XAS confirmed an asymmetric SeN_2-FeN_2 coordination structure with direct Se–Fe bonding (~ 2.3 Å distance). A similar "Y-type" SeN_2-FeN_2 structure (FeSn-C_2N) was achieved via two-step pyrolysis (Fig. 7(b)), leveraging strong Sn(p)-Fe(d) orbital overlap for stability [59]. The asymmetric Ni/Fe N/O C APCs was synthesized by adsorbing Ni^{2+}/Fe^{2+} onto carbon black followed by pyrolysis/acid leaching. This catalyst features direct Ni–Fe bonding, two axial O ligands per metal, and O-C-N bridging ligands (Fig. 7(c)). It demonstrated exceptional durability and CO selectivity in CO_2RR [45]. Furthermore, another 3d-metal based heteronuclear ADCs IrCo-N-C and FeCu-NC catalysts were constructed. Utilizing advanced precursor strategies, IrCo-N-C (via bimetallic MOF encapsulation) with a single N bridge modulated the Co d-orbital, achieved outstanding ORR activity ($E_{1/2}$ = 0.911 V) [63]. FeCu-NC prepared by anchoring metals on 2D IISERP-MOF27 nanosheets followed by pyrolysis, exhibited synergistic ORR activity in its FeN_3O-CuN_4 structure [65]. Other directly bonded heteronuclear pairs like FeNi ADSs/HOPSNC [85], Fe-Mn-N-C [64], Fe_1Co_1-CNF (N-C-C-N bridged) [106], f-FeCo-NC (N-C-N bridged) [107], and NCAG/Fe-Co carbon aerogel [41] further exemplify the diversity of directly bonded heteronuclear ADCs and their varying ORR activities, underscoring the critical role of precise coordination environment control through tailored synthesis.

Non-metal bridged structures are characterized by heteronuclear pairs that are interconnected through shared non-metallic bridging atoms. An illustrative example is FeCo-N_3O_3@C (Fig. 7(d)), in which Tang et al. employed a "one-pot" low-temperature pyrolysis strategy on 2D MOF nanosheets to create FeCo-N_3O_3@C, featuring Fe and Co doubly bridged by N and O atoms (Janus sites) [61]. AC-HAADF-STEM indicated ~ 85% dimer pairs, contributing to superior bifunctional ORR/OER activity. Hu and co-workers prepared FeMn-N-C via electrospinning and *in situ* pyrolysis/acid etching, resulting in double N bridges (Fig. 7(e)). This structure facilitates direct O–O bond dissociation in ORR [108]. Analogous catalysts like Fe/Mn-N_x-C (double N bridge + axial OH on Fe) [109] and Fe,Mn/N-C (double single N bridge) [78] achieved high ORR performance ($E_{1/2}$ up to 0.928 V in alkaline, 0.804 V in acid). The Fe/Mn-N_x-C catalyst was synthesized using ZnO@PDA-FeMn precursor and ZnO nanorods template. During the high temperature carbonization process, polydopamine (PDA) adsorbed metal ions and anchored to the defect site of graphitized carbon [109]. In addition, the Fe,Mn/N-C catalyst containing double single N bridge was synthesized on N-doped defect carbon using iron phthalocyanine (FePc) and manganese nitrate ($Mn(NO_3)_2$) as metal precursor by polymerization and pyrolysis processes [78]. Similar, analogous catalysts like the N-coordinated Fe-Sn-N/C [34] and CoFe-N-C [77] catalyst containing double single N bridge can be synthesized by pyrolysis strategy for ORR.

The final category, non-bridged asymmetric pairs, encompasses heteronuclear ADCs where catalytic synergy arises from spatially proximate yet independently coordinated metal atoms, without direct metal-metal bonds or shared bridging ligands. As demonstrated in Fig. 7(f), Tang and co-workers developed a modified precipitation-pyrolysis strategy using Pr and Ni nitrates on carbon black to synthesize Pr/Ni-NC [110]. Despite the absence

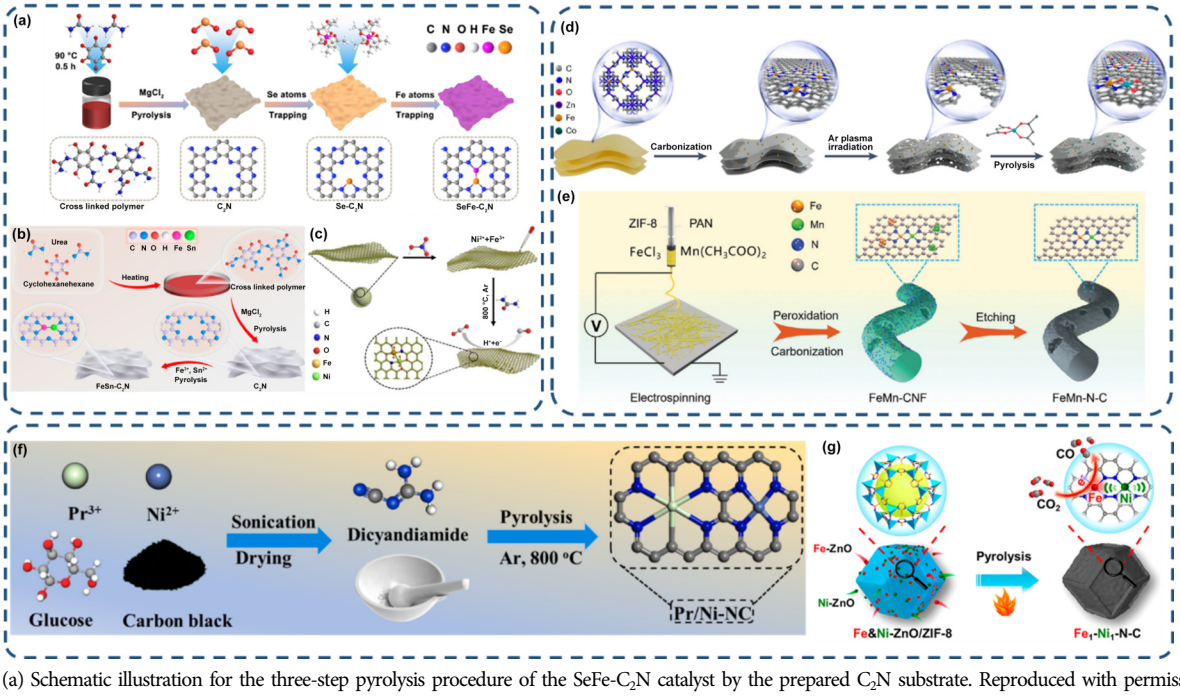

Figure 7 (a) Schematic illustration for the three-step pyrolysis procedure of the SeFe-C_2N catalyst by the prepared C_2N substrate. Reproduced with permission from Ref. [5], © Wang, X. C. et al. 2025. (b) Schematic illustration of the synthesis for the FeSn-C_2N Catalyst. Reproduced with permission from Ref. [59], © American Chemical Society 2024. (c) Schematic of synthesis of single- and dual-atom M-N/O-C catalysts. Reproduced with permission from Ref. [45], © Wiley-VCH GmbH 2021. (d) Synthetic scheme for the simple "one-pot" method of the FeCo-N_3O_3@C catalyst from MOF. Reproduced with permission from Ref. [61], © Tang, B. et al. 2024, under exclusive licence to Springer Nature Limited. (e) Schematic of the synthesis process with FeMn-N-C. Reproduced with permission from Ref. [108], © Wiley-VCH GmbH 2024. (f) Schematic illustration of two-step preparation process of Pr/Ni-NC catalyst. Reproduced with permission from Ref. [110], © Elsevier B.V. 2024, all rights reserved. (g) Schematic illustration for construction of Fe_1-Ni_1-N-C with neighboring Fe and Ni single-atoms based on ZIF-8. Reproduced with permission from Ref. [44], © American Chemical Society 2021.

of direct bonding or bridges, Pr and Ni atoms are indirectly linked via N-C-N moieties within a complex N/C coordination environment. Overlapping EELS signals confirm the atomic pair proximity, correlating with the catalyst's excellent CO_2RR activity. FeCo-N-C, featuring a similar indirect linkage motif, exhibits outstanding ORR performance [111]. The Fe_1-Ni_1-N-C catalyst (Fig. 7(g)) synthesized via an assembly-pyrolysis approach, this catalyst positions Fe and Ni sites connected by two identical N-N indirect linkages [44]. The resulting The Fe_1-Ni_1-N-C demonstrates superior CO_2RR performance, characterized by excellent CO selectivity and exceptional durability in Zn-CO_2 batteries. Furthermore, Co-Ni-N-C employ a strategy involving cation exchange into Co-doped ZIF-8 followed by Ni incorporation and pyrolysis. The obtained Co-Ni-N-C features Co and Ni atoms connected by two N-C-N bridges anchored within N-doped graphitic carbon [55]. These N-coordinated bimetallic sites deliver exceptional CO_2RR activity. Additionally, ZnCo-NC-II catalyst prepared via carbonization, adsorption, and thermal activation, contains Zn and Co sites linked by a single N-N indirect bridge [47]. Such precise coordination design is crucial for establishing robust structure-activity relationships and facilitating in-depth catalytic mechanism investigation.

3.3 The application of AI in ADCs

In recent years, with the rapid development of computing hardware and cutting-edge machine learning (ML) algorithms, artificial intelligence (AI) has provided a new paradigm of automated and intelligent transformation for the precise and efficient synthesis of catalysts [112, 113]. Unlike traditional methods, AI techniques leveraging density functional theory calculations excel at solving complex synthesis challenges by facilitating catalyst structure design and selection, screening optimal synthesis routes, and establishing structure-activity relationships [114–119]. As the core engine of AI, ML algorithms uncover latent patterns within complex experimental and computational datasets. This capability allows rapid prediction of novel catalyst compositions/structures and accelerates high-performance candidate screening [120–123]. Beyond performance prediction, ML further optimizes synthesis protocols, identifies efficient preparation strategies, and streamlines characterization data interpretation [124–126]. Traditional catalytic descriptors (e.g., d-band center, adsorption energy) suffer from scalability limitations due to their heavy reliance on DFT computations [127]. Conversely, DFT-ML integrated high-throughput screening harnesses ML's power in mechanistic analysis to rapidly discover high-performance, selective ADCs, significantly shortening development cycles and reducing research costs [128–131].

Cao and co-workers established an accurate high-throughput screening strategy based on the dynamic axial adsorption of the active site of ADCs at the working potential and the adsorption of reactants as the rate-determining step [76]. The ORR of 42 kinds of 3d-3d metal ADCs by DFT calculations are systematically investigated and demonstrated. Theoretical calculations of free energy (O*, OH*, and H_2O*) through the surface Pourbaix diagrams combined with experimental characterizations of pre-adsorption of O* or OH* intermediates and H_2O on ADCs were used to evaluate the dynamic structural evolution on the catalyst surface under ORR working conditions. The most stable form $MnZnN_7$-$(OH)_2$ is determined by the onset potential (U^{ORR}). The availability of gradient boosting regression (XGBR) algorithm was highly used to assess the number of axial preadsorption of OH (n_{OH}) and activity descriptor ($\Delta G_{OH^*}/\Delta G_{O_2*}$). The ORR polarization curve was simulated by theoretical model, and the kinetic feasibility of pre-adsorption of O* or OH* intermediates on the ADCs was deeply insighted. Based on the observation that the electrode microkinetic model is consistent with the surface Pourbaix diagram, it can be concluded that when evaluating the theoretical ORR activity of ADCs, the dynamic reconstruction of active sites should be given sufficient attention. DFT results revealed that the kinetics of ORR can be limited by the adsorption of O_2* besides the proton-electron transfer step, and the active centers of DACs can be reconstructed by axial pre-adsorption of intermediates under working potential. The authors proposed using both O_2* and OH* adsorption as active descriptors for the ORR volcano plot, and thereby developed a high-throughput screening framework to screen out 38 promising ORR DACs from 267 DACs containing 3d, 4d or 5d metals (Fig. 8(a)). The entire screening process includes: first, screening out 152 kinds of stable DACs (step 1), then calculating the adsorption-free energies and average adsorption-free energy of OH* to determine the real configuration of DACs (step 2), followed by predicting the thermodynamic U^{ORR} using the linear relationship between ΔG_{OH^*} and ΔG_{OOH^*} ($\Delta G_{OOH^*} = 0.66\Delta G_{OH^*} + 3.44$), and judging whether it was self-consistent with the identified stable surface structure according to the Pourbaix diagram (step 3), then screening out DACs with ΔG(OH*) and ΔG(O_2*) located in the range of 0.77–1.23 eV and 0.68 ΔG(OH*) + 3.75 – 0.68ΔG(OH*) + 5.50 (steps 4 and 5), calculating the adsorption-free energies of O* and 2OH* for DACs, and finally evaluating the selectivity of DACs for $4e^-$ ORR or $2e^-$ ORR (step 6). Importantly, containing 12 kinds of DACs have been verified to surpass Pt/C in available experiments by the high productivity of the high-throughput method, especially the previously unexplored $MnCoN_6$ DAC was also experimentally synthesized and demonstrated the superior alkaline ORR activity to that of Pt/C (marked in red in Fig. 8(b)). The most important electronegativity and valence electron of active sites significantly affect free energy of adsorption and ORR performance in DFT calculation and ML prediction special considering the axial pre-adsorption of OH and the adsorption of O_2 step.

Mao and co-workers demonstrate derived catalytic "hot spot map" through ML, using the geometric distance of the diatom and electron magnetic moment as axes, and proposed the geometric and electron coupling design strategy for optimizing the ORR performance of efficient ADCs [73]. The comprehensive workflow that integrates DFT calculations and ML has been developed to construct the geometric and electronic effects coupling of the design of diatomic ORR catalysts (Fig. 8(c)). The machine learning assisted high-throughput screening method can be used to generate and preprocess the key parameters (geometric parameters, electronic properties and systematic parameters) for DFT calculations, and then to establish a robust dataset for machine training can be employed to predict the optimal catalyst. According to four electronic dynamic transfer steps: * + O_2 → *OOH → *O → *OH → * + H_2O of Gibbs free energy variation in M_1-N-M_2/NCs, the OOH*, OH* formation, and OH* desorption were possible potential determination steps. Choosing the overpotentials as the targeted variables for ML enables an effective analysis of the dynamic structure of the catalysts in the whole ORR steps. Apart from the selection of the optimal catalyst, the key factor affecting catalytic performance was explained by the geometric and electronic descriptors. The predicted optimal catalyst (Co-N-Mn/NC) was

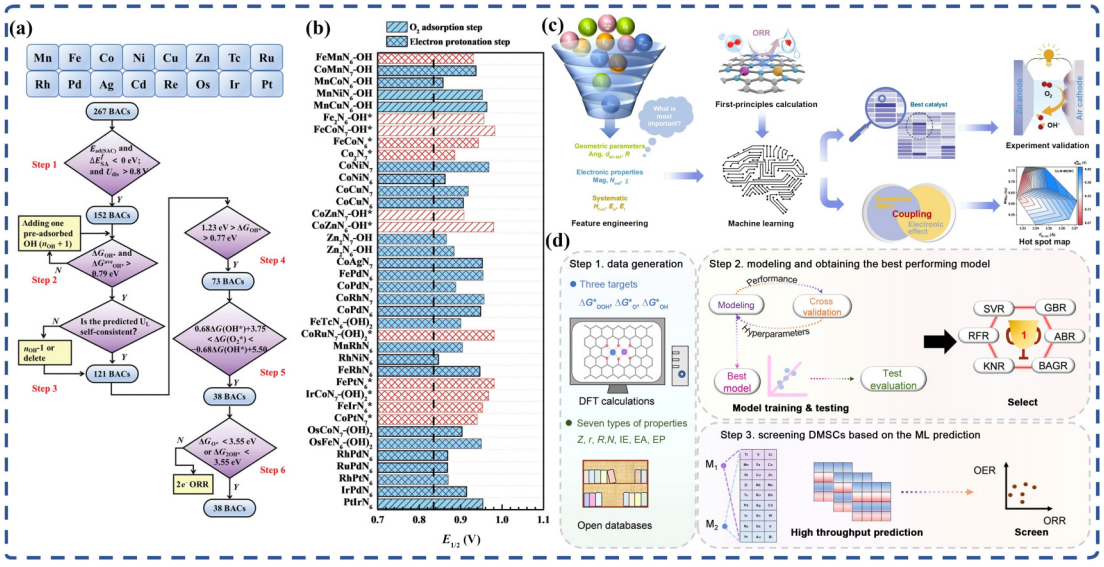

Figure 8 (a) High-throughput screening flow diagram for DACs with promising ORR activity. (b) The $E_{1/2}$ and rate-determining step of identified DACs with higher ORR activity than Pt(111). Reproduced with permission from Ref. [76], © American Association for the Advancement of Science 2025. (c) Schematic of the workflow based on the DFT-ML-experiment method to achieve a principle coupling of geometric and electronic parameters for the design of M_1-N-M_2/NCs. Reproduced with permission from Ref. [73], © Liu, Y. et al. 2025. (d) Schematic of the machine learning workflow on ORR/OER catalytic activity for DACs. Reproduced with permission from Ref. [132], © American Chemical Society 2024.

synthesized and characterized. GBR algorithm and DFT calculation predicted selected the predicted top 10 M_1-N-M_2/NCs, among which Co-N-Mn/NC exhibited the lowest overpotential of 0.27 V. Co-N-Mn/NC with excellent structural stability preferred the four-electron transfer catalytic mechanism to the two-electron transfer path for H_2O_2 generation by DFT calculations and ab initio molecular dynamics simulation. The LSV curve indicated that Co-N-Mn/NC exhibited the highest ORR activity, featuring a $E_{1/2}$ of 0.900 V, which is superior to CoNC (0.871 V), MnNC (0.839 V), NC (0.768 V), and Pt/C (0.883 V).

Sun and co-workers proposed an advanced high-throughput screening method that combines DFT with ML, which solves the problems of high cost and low efficiency encountered by traditional experiments or DFT calculations when dealing with large design models [132]. By constructing the best-performing and well-trained gradient boosting regression (GBR) regression model compared with support vector regression (SVR), random forest regression (RFR), adaboost regression (ABR), k nearest neighbors regression (KNR) and bagging regression (BAGR), the adsorption free energy and catalytic performance of 729 DACs composed of 27 metal elements (Ti, V, Cr, Mn, Fe, Co, Ni, Cu, Zn, Zr, Nb, Mo, Tc, Ru, Rh, Pd, Ag, Cd, In, Sn, W, Re, Os, Ir, Pt, Au, and Bi) in pairs for the ORR or OER were rapidly predicted, significantly improving the efficiency of discovering high-performance catalysts (Fig. 8(d)). A well-trained GBR model can accurately predict the adsorption free energy to a large extent, and it is consistent with the values calculated by DFT. The research not only identified 30 ADCs with better ORR performance than Pt(111), 10 catalysts with better OER performance than RuO_2(110), and 4 bifunctional electrocatalysts by DFT-ML method, but also revealed the key mechanisms between the metal electronic structure and the adsorption behavior. The overpotentials predicted by ML are very close to the true value, which is benefit for efficiently discovering potential high-performance dual metal active sites catalysts. Four bifunctional electrocatalysts ($RuCoN_6$, $RuIrN_6$, $OsRhN_6$ and $OsCoN_6$) were identified for both the ORR and OER. The fast and efficient DFT-ML high-throughput screening method have extensive application scenarios and will drive the development of catalysis science in the future.

4 Characterization of ADCs

4.1 Morphological and structural characterization

The synergies of diatomic asymmetric catalytic sites and the diversity of coordination environments in ADCs increase the difficulty of their design. The characterization of the precise structure of the successfully synthesized ADCs at atomic scale is beneficial to the study of structure-activity relationship of asymmetric bimetallic sites in electrocatalysis. Here, we briefly summarize the characterization of ADCs morphology and coordination structure by advanced instrumental analysis techniques (Fig. 9). Due to XPS is sensitive to the local structure and chemical environment of the central absorbing atom, it is an indispensable characterization method in the study of single dual atom catalysis, and can provide key information about the chemical state, electronic structure and interaction with the carrier of the metal single atomic sites. X-ray diffraction (XRD) can be used in the analysis of ADCs to determine the crystal form of the support, indirectly infer the dispersion form of the metal sites through the diffraction peaks of characteristic particles, and assist in analyzing the interaction between the metal and the support by the shift of peak positions. However, XRD and powder XRD (PXRD) cannot directly characterize single atoms and has limited sensitivity. Electron microscopic techniques including scanning electron microscopy (SEM), transmission electron microscopy (TEM), scanning TEM (STEM), Aberration-corrected STEM (AC-STEM), electron energy loss spectroscopy (EELS), energy dispersive X-ray spectroscopy (EDS) and *in situ* electron microscopy (*in situ* EM) have been widely used for the morphological characterization of catalysts with atomic dispersed sites. The inductively coupled plasma optical emission spectrometry (ICP-OES) has a high

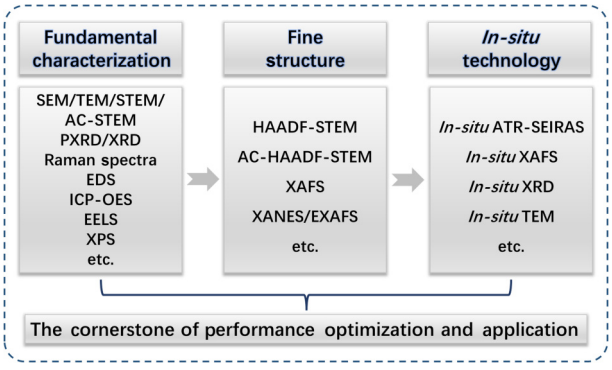

Figure 9 Schematic illustration of morphological and structural characterization for ADCs.

sensitivity (in the ppb range) and can quantitatively determine the total content of metal elements (such as Pt, Fe, Co, etc.) in the catalyst, thereby confirming the theoretical density of single-site. It is an indispensable quantitative tool in the study of ADCs, playing a key role especially in load control, stability assessment, and synthesis optimization. However, its data needs to be combined with structural characterization techniques (such as XAS, STEM) to fully reveal the true characteristics of dispersed atom catalysts. The methods used for basic characterization also include EDS, EELS, Raman spectra, etc. These provide a solid research foundation for the characterization of the fine structure of ADCs.

The characterization of the fine structure of the ADCs involves ultra-high precision TEM analysis and X-ray absorption spectroscopy (XAS) analysis based on synchrotron radiation. The aberration-corrected HAADF-STEM (AC-HAADF-STEM) have the advantage of sub-angstrom spatial resolution and atomic number sensitivity, enabling direct observation of the diatomic dispersed sites. Subsequently, the coordination structure of the ADCs was characterized by XANES and EXAFS in XAFS. Synchrotron radiation light possesses excellent characteristics such as good collimation, high flux, high brightness, wide and continuous spectral range, and polarization. These features enable it to be widely applied in the field of nano-material structure analysis. The XAFS method based on synchrotron radiation measures the variation of the absorption coefficient of materials to X-rays with energy, providing information such as the electronic structure, local geometry and chemical state of elements. As an important characterization technique for studying the local fine structure of substances, it is one of the indispensable tools for the development of atomic dispersed catalysts. XANES, also known as near-edge X-ray absorption fine structure (NEXAFS), is sensitive to the oxidation state, coordination symmetry and unoccupied electronic states of elements. It can be used to predict the coordination environment including the electronic orbitals and valence states of the two metal atom centers. EXAFS can provide information on the type of coordination atoms, coordination number, bond length, types of neighboring elements and even the structure of the adjacent coordination shell after Fourier transformation. The dynamic structural changes of ADCs during electrocatalytic reactions can be analyzed using *in situ* techniques, which is elaborated in detail in Section 4.2.

A universal metal-ion recognition (MIR) strategy enables the synthesis of Fe_1Sn_1-diatomic catalysts (Fe_1Sn_1-DACs), effectively overcoming limitations associated with conventional ADCs (Fig. 10(a)) [133]. Atomic-scale characterization using AC-HAADF-STEM (Fig. 10(b)) reveals the presence of heteronuclear Fe/Sn active sites, which are further validated through three-dimensional Gaussian fitting. EXAFS, XANES and wavelet transform analyses confirm the atomic dispersion, oxidation states, and the presence of metal-N and metal-metal bonding pathways. DFT-based EXAFS modeling identifies a dual-N-bridged Fe-Sn configuration (Fig. 10(c)). The Fe_1Sn_1-DAC delivers a record peak power density of 1.218 W·cm^{-2} under 2.0 bar H_2-O_2 conditions and higher than that of Fe_1-SAC (0.514 W·cm^{-2}) and Pt/C (1.218 W·cm^{-2}) in ORR process.

DFT-guided synthesis of FeRu-N-C catalysts targets acidic ORR enhancement [87]. Theoretical screening identifies $FeMN_8$/C (Fig. 10(d)) as optimal, revealing Ru-modulated atomic strain optimizes d-band/COHP properties. Synthesized via host-guest chemistry, multimodal characterization confirms the coordination environment. XANES analysis shows that the valence state of Fe is between metallic state and +2. While the valence state of Ru is lower than +4. The fitting of FT-EXAFS and WT-EXAFS give a more detailed coordination environment (Fig. 10(e)). The morphology of the FeRu-N-C catalyst was characterized by AC-HAADF-STEM (Fig. 10(f)). The image reveals a typical atomic dispersion, with the co-presence of heteronuclear diatoms. Finally, the effective magnetic moment calculated by Curie-Weiss law and Mössbauer spectroscopy further reveal that the superior ORR activity of FeRu-N-C originated from optimized atomic strain structure.

The precise identification of dual active sites in ADCs is of great significance. Currently, the most visual testing method for characterizing bimetallic site catalysts is AC-HAADF-STEM. However, the sample images recorded by AC-HAADF-STEM are along the direction of the transmitted electron beam, which means that the two adjacent metal atoms on the surface of the sample might be two atoms distributed on the front and back sides of the carbon carrier (that is, they might be "false" bimetallic sites). Chen and co-workers developed a two-step specific-adsorption strategy (pyrolysis-free) to construct FeCo "molecular heterostructures" (FeCo-MHs) ADCs (Fig. 10(g)) [51]. In order to eliminate the existence of "false" MHs, the *in situ* rotation (by 8°, far above the critical angle of 5.3°) operation of AC-HAADF-STEM was utilized to directly identify a single "true" FeCo-MHs. As shown in Fig. 10(h), it is the test results of the *in situ* rotation of 8° rotation AC-HAADF-STEM measurements combined with STEM-EELS. The results confirmed that the apparent metal-phthalocyanine (MPc) atom-pair are adsorbed on the same side surface of carbon nanotubes (CNTs). The rotation AC-HAADF-STEM measurements provided compelling evidence for the presence of the formed a molecular heterostructure by complexes metal-phthalocyanine (MPc) molecules on the same side of CNT. Also, XAS was conducted to probe the local chemical environment of the metal centers in FeCo-MHs (Fig. 10(i)).

4.2 *In situ* characterization

In the preparation and performance analysis of catalysts, the *in situ* characterization has the advantages of real-time dynamic monitoring, revealing reaction mechanism, identification of active sites and evaluation of catalyst stability. Here, we briefly summarize several *in situ* analysis methods for ADCs. Pei and co-workers synthesized catalyst Zn_1Mn_1-SNC [53]. In the *in situ* XAFS analysis of this catalyst, the Mn absorption edge of the XANES spectrum at the Mn K-edge gradually migrates to lower energy from the open

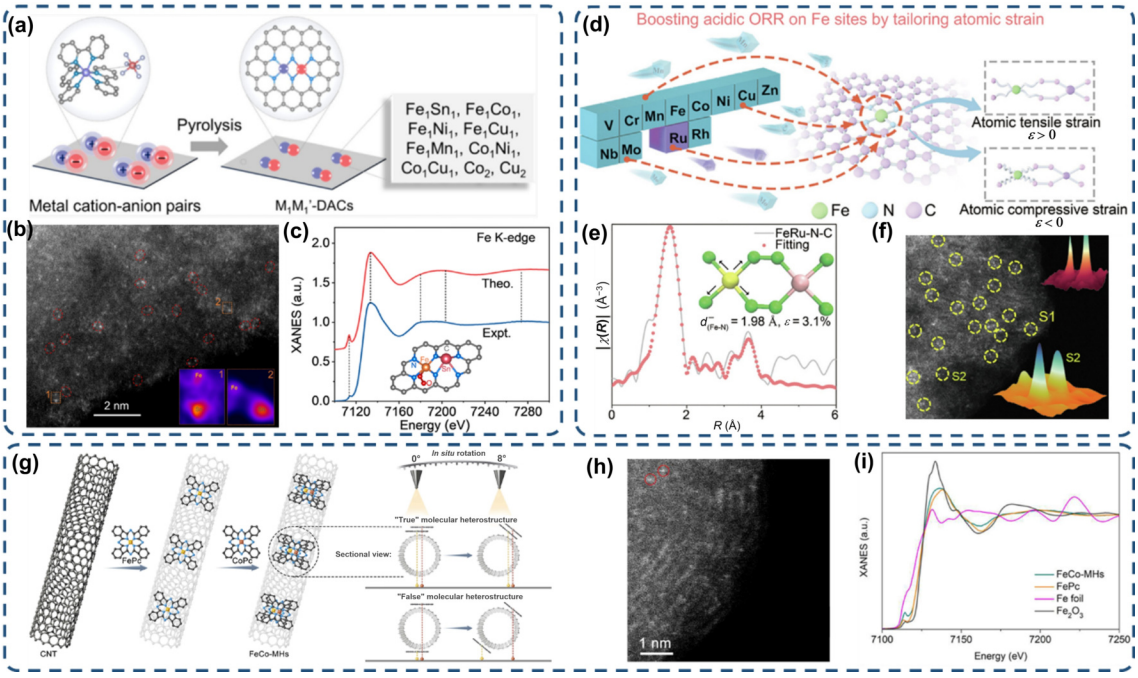

Figure 10 (a) Schematic illustration of the metal ion recognition strategy for $M_1M'_1$-DACs. (b) AC-HAADF-STEM image of Fe_1Sn_1-DAC (inset: 3D atom-overlapping Gaussian-function fitting map regions 1 and 2). (c) A comparison of the experimental XANES spectrum and the theoretical spectrum for Fe_1Sn_1-DAC (inset: The optimized the coordination structure of catalyst). Reproduced with permission from Ref. [133], © American Chemical Society 2024. (d) Diagram for tailoring atomic strain of Fe sites by second metal atoms. (e) Fitting results of the EXAFS spectra of FeRu-N-C. (f) The AC-HAADF-STEM image of FeRu-N-C. Reproduced with permission from Ref. [87], © Elsevier Inc. 2024. (g) Schematic of the molecular heterostructures design of FeCo-MHs containing specific-adsorption strategy and the determination of the "true" and "false" MH. (h) Metal-atom-pair after rotation for 8° in AC-HAADF-STEM image. (i) Structural characterization of FeCo-MHs catalyst by the Fe K-edge XANES spectra. Reproduced with permission from Ref. [51], © American Chemical Society 2023.

circuit voltage (OCV) state to 0.45–0. 55 V (Fig. 11(a)), and the conclusion of the valence state of Mn in the Zn-Mn dual site (between 0 and 2) was obtained by the analysis of the first-derivative XANES curves (Fig. 11(b)). The same valence change of Zn in catalyst Zn_1Mn_1-SNC DASC was obtained by the same analysis. This phenomenon can be attributed to the fact that the asymmetric Mn and Zn active atoms experienced a gradual reduction of valence states with the OCV state to 0.45 to 0. 55 V during the *in situ* process of CO_2RR (Fig. 11(c)). In addition, *in situ* attenuated total reflectance surface-enhanced infrared absorption spectroscopy (ATR-SEIRAS) was used to monitor the reaction intermediates in CO_2RR (Fig. 11(d)). With the increase of potential, CO_2 and H_2O were continuously consumed, and the desorption loss of CO species gradually increased, and COOH* gradually formed. The *in situ* ATR-SEIRAS analysis of the main functional groups in the CO_2RR process of Zn_1Mn_1-SNC indicated that the asymmetric Zn-Mn dual active sites played a key role in the adsorption, activation and transformation of CO_2.

Similar studies have also included Ag-CdTMT catalysts using host-guest strategies to synthesize asymmetric double-site Ag, Cd and N Bridges respectively [56]. The *in situ* Cd K-edge XANES spectral analysis revealed a reduction in the Cd valence state during CO_2RR (Fig. 11(e)). The Ag absorption edge exhibited less energy shift compared with Cd. Further K-edge XANES analysis confirmed that the valence state of Cd exhibited a notable shift (Fig. 11(f)), whereas Ag exhibited no significant changes. This behavior suggested that Cd in the Ag-Cd diatomic site may be the main active center, and the electronic structure had been changed in CO_2RR. The *in situ* EXAFS spectral analysis of Cd and Ag indicated that the local coordination structure at the Ag-Cd diatomic sites undergo dynamic changes during CO_2RR. The dynamic changes of reaction intermediates were further studied by *in situ* ATR-SEIRAS (Fig. 11(g)). It was observed that with the increase of voltage, CO_2 was gradually consumed, and the important reaction intermediates COOH* was gradually formed (Fig. 11(h)). The conclusion demonstrated that the synergistic Ag-Cd sites promoted the adsorption and activation of CO_2 and the conversion of the key intermediate COOH*, thus increasing the kinetic rate of CO_2RR.

In order to further clarify the advantages of local microstrain environments in regulating electronic structure and optimizing intermediate binding energy of catalysts in *in situ* analysis, the main structural models of Ag-CdTMT and CdTMT were established, and DFT calculations were performed (Fig. 11(i)) [56]. The free energy changes for CO_2RR during the CO_2-to-CO conversion process were calculated (Fig. 11(j)). It is obviously observed that the binding strength of *COOH intermediates at the Cd atoms of AgN_2S_2-CdN_2S_2 sites (0.39 eV) is much smaller than that of CdTMT (1.94 eV). Theoretical calculation indicated that that CO_2 was more readily activated and evolved to *COOH on AgN_2S_2-CdN_2S_2 sites of Ag-CdTMT catalyst, which is the same as the analytical conclusion of *in situ* ATR-SEIRAS spectra.

In addition, Hu and co-workers developed a high-durability PtCo nanoalloy catalyst PtCo/$P_{2.73}O_x$-KB for Polymer Exchange Membrane Fuel Cells (PEMFCs) [134]. The team developed a liquid phase *in situ* XRD cell to monitor the dynamic change of active species of catalysts during ORR (Fig. 11(k)). *In situ* XRD characterization of PtCo/$P_{2.73}O_x$-KB during the ORR process was observed in Fig. 11(l). Yoon and co-workers observed the morphological changes of Cu_2O cube at different potentials by

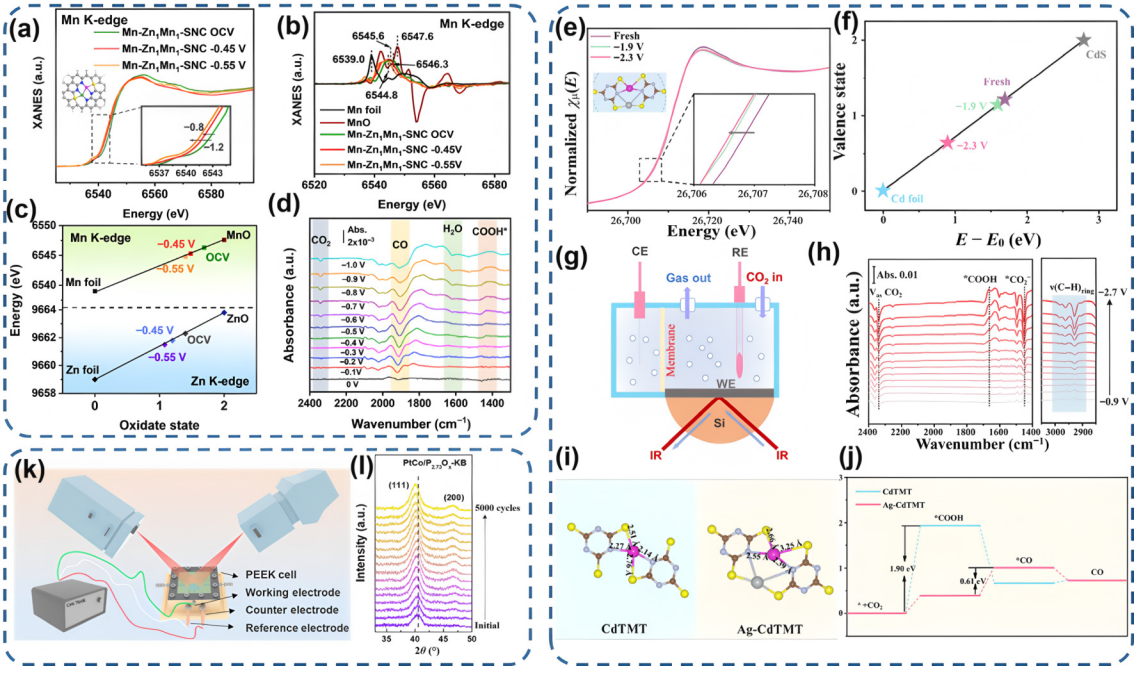

Figure 11 (a) *In situ* normalized XANES spectra at the Mn K-edge on Zn_1Mn_1-SNC at different applied potentials. (b) Corresponding first-derivative XANES curves at the Mn K-edge. (c) Oxidation state of Zn_1Mn_1-SNC at the Mn and Zn K-edge. (d) *In situ* ATR-SEIRAS spectra on Zn_1Mn_1-SNC. Reproduced with permission from Ref. [53], © Wiley-VCH GmbH 2023. (e) *In situ* XANES spectra at Cd K-edge of Ag-CdTMT. (f) Valence state of Ag-CdTMT at Cd K-edge. (g) *In situ* ATR-SEIRAS device schematic. (h) *In situ* ATR-SEIRAS spectra of Ag-CdTMT. (i) The optimized structures of CdTMT and Ag-CdTMT. (j) The calculated Gibbs free energy diagrams for CO_2RR on the two catalyst surfaces. Reproduced with permission from Ref. [56], © American Chemical Society 2024. (k) Schematic diagram of the *in situ* XRD apparatus using a home-made device. (l) *In situ* XRD patterns during potential cycling with $PtCo/P_{2.73}O_x$–KB. Reproduced with permission from Ref. [134], © The Royal Society of Chemistry 2024.

using *in situ* electrochemical liquid cell transmission electron microscopy (EC-TEM) and electrochemical liquid cell transmission X-ray microscopy (EC-TXM). And the reconstruction mechanism of Cu_2O in nitrate reduction reaction was revealed by using *in situ* Raman spectroscopy and XAS [135]. Yang and co-workers revealed active Cu nanograins for electrocatalytic CO_2RR electroreduction by using *in situ* electrochemical scanning transmission electron microscopy (EC-STEM) and four-dimensional scanning transmission electron microscopy (4D-STEM) [136]. These *in situ* analysis methods have important practical value and are expected to be developed in the study of ADCs in the future.

By definition, while "*in situ*" emphasizes conditions relevant to practical operations, "*operando*" involves observing the catalytic behavior of working catalysts during actual reaction conditions. Both of them have emerged as pivotal key tools for investigating the dynamic evolution of both microstructural changes within the active sites and concurrent changes in catalytic property by real-time monitoring in catalytic reactions [137]. The *operando* reconfiguration helps to capture active species that differ from the initial structure, thereby establishing a clear relationship among structure, property and performance [138, 139]. Kang and co-workers studied the dynamic evolution of an asymmetric N_3Sn-CoN_3 structure, which significantly improved the ORR kinetics under working conditions [140]. Sn-Co diatomic pairs in $SnCoN_6$ DA dispersed on N-doped carbon are prepared by a molten-salt-assisted hard-template method. The oxygenophilic Sn site generate stereogeometric *OH-$SnCoN_6$ by operando hydroxylation that enables greater hybridization between Co d orbitals and O_2 s/p orbitals in the sophisticated microkinetic modeling of *in situ* Raman and attenuated total reflectance Fourier transform infrared spectroscopy (ATR-FTIR). The *OH-Sn moiety serves as an electron modulator effectively tailors the 3d orbital filling degree of the neighboring Co, then, enables stronger binding with *OOH and expedites subsequent O-O cleavage. The operando hydroxylation of $SnCoN_6$ DA enhanced the half-wave potential and kinetic current density of the ORR process. Chen and co-workers deciphered a potential-dependent in-plane atomic intrinsic dynamic evolution of asymmetric atomic sites Cu-Ni in electrocatalytic CO_2RR [141]. Asymmetric coordinated Cu-Ni atomic dimers anchored on porous carbon through N/S coordination were unveiled that fully transformed into Cu_x-Ni atomic clusters (Cu_x-Ni ACs, x = 3–7) at potentials from −0.7 to −1.2 V versus RHE by operando X-ray spectroscopy and microscopy. Operando measurements and theoretical analysis pointed out that the formation of Cu-rich Cu_x-Ni atomic clusters facilitated the interaction between Cu-Cu/Ni bonds by the antibonding orbital occupancy between Cu 3d and C 2p states, thereby optimizing the adsorption energy and facilitating the occurrence of the electrocatalytic CO_2RR. The research successfully provided fundamental insights into the dynamic reconstruction and catalytic mechanism of atomic-scale active sites using the operando analysis.

5 Applications of ADCs

5.1 ORR

In recent years, scientific researchers have been actively pursuing sustainable alternative energy sources to address environmental pollution and global energy challenges. Proton exchange membrane fuel cells (PEMFCs), metal-air batteries, and other energy conversion technologies are considered promising clean energy solutions due to their high energy density and environmental

compatibility [142–145]. The ORR is a significant chemical process that takes place in the metal-air battery and fuel cell cathodes [146–148]. ORR involves multiple sequential steps such as oxygen adsorption, proton and electron transfer, bond cleavage and formation, and product desorption, presents significant challenges for its practical implementation in metal-air batteries and fuel cells. Noble metal catalysts can be used to provide high ORR activity and stability, while their high cost and scarcity restricted their industrial application [149–152]. Therefore, developing cost-effective and efficient electrocatalysts for ORR is crucial to achieving the widespread usage of these devices [153, 154].

Single-atom catalysts have attracted the attention of many researchers due to their high dispersion, high atomic utilization, and clear active sites [155–158]. Compared with the monoatomic catalyst, two adjacent metal atoms (homonuclear or heteronuclear) in the diatomic catalyst can form a unique electronic structure and synergistically activate the reactants through the interaction between atoms (such as charge transfer, orbital hybridization). In ORR, dual-atom active sites can independently adsorb reaction intermediates, thereby facilitating the cleavage of O–O bonds [54, 55, 159]. The ADCs reported for the ORR are summarized in Table 2, where five representative examples are selected to illustrate the underlying factors contributing to the superior ORR performance of ADCs. Among these, several typical examples are

Table 2 Summary of the ORR performance of carbon-based ADCs catalysts along with the corresponding synthesis method, active sites, electrolyte, E_{onset} and $E_{1/2}$

Catalyst	Active sites	Synthetic method	Electrolyte	E_{onset} (V)	$E_{1/2}$ (V)	Ref.
$ZnCoN_6$	Zn-Co	Competitive complexation stretegy	0.1 M KOH, 0.1 M $HClO_4$	1.004, 0.97	0.861, 0.796	[165]
Fe,Mn,N-FGC	Fe-Mn	High-temperature pyrolysis method	0.1 M KOH	1.03	0.89	[43]
Fe-NiNC-50	Fe-Ni	One-step dual-solvent impregnation route	0.1 M KOH	0.86	0.75	[42]
NCAG/Fe-Co	Fe-Co	Wet-chemistry approach	0.1 M KOH	1.04	0.89	[41]
Fe-Co-N-C	Fe-Co	High-temperature pyrolysis method	0.1M KOH, 0.1 M $HClO_4$	0.97, 0.85	0.87, 0.74	[166]
Ni_xFe_{100-x}-NC	Ni-Fe	High-temperature pyrolysis method	0.1M KOH	0.995	0.920	[167]
f-FeCo-CNT	Fe and Co	High-temperature pyrolysis method	0.1M KOH	1.04	0.904	[107]
AuCo-N_2C_2	Au-Co	Host-guest and chemical doping strategies	0.1 M $HClO_4$	0.918	0.82	[48]
AFeCo@NCNs	FeN_4 CoN_4 or N_3Fe-CoN_3	Hard template method	0.1 M KOH	1.03	0.87	[168]
Co_1-PNCNi_1-PNC	Co and Ni	Host-guest strategy and *in situ* phosphating method	0.1 M KOH	1	0.88	[169]
Cu/Zn@NC	Cu-N_4 and Zn-N_4	Self-assembly of colloidal nanocrystals	0.1 M KOH	0.98	0.83	[170]
Fe,Co-SA/CS	Fe and Co sites	High-temperature pyrolysis method	0.1M KOH	0.96	0.86	[171]
Fe_1Co_1-CNF	Fe-Co sites	Electrospinning method	0.1M KOH	0.96	0.87	[106]
Fe_1Pt_1-NC	Fe-N_4 and Pt-N_4	High-temperature pyrolysis method	0.1 M KOH	1.04	0.91	[172]
$FeCoN_6$	CoN_4 and FeN_4	Chemical doping and adsorption procedure	0.5 M H_2SO_4	1.00	0.85	[173]
FeCo-N-C	Fe-N_4 and Co-N_4	One-step impregnation pyrolysis	0.1M KOH, 0.1 M $HClO_4$	—, —	0.904, 0.807	[111]
FeMnN-C	Fe/Mn atomic pairs	Soft-template pyrolysis method	0.1M KOH, 0.1 M $HClO_4$	—, —	0.928, 0.804	[78]
Fe/Mn-N_x-C	Fe-N_x and Mn-N_x	High-temperature pyrolysis method	0.1M KOH	1.02	0.88	[109]
FeCo-N-HCN	Fe-N_4 and Co-N_4	High-temperature pyrolysis method	0.1M KOH	0.98	0.86	[174]
FeNi SAs/NC	Fe-Ni-N_6	Coprecipitation method	0.1 M KOH	0.98	0.84	[175]
Fe/Ni-N-C	FeNi dual-site	High-temperature pyrolysis method	0.1 M KOH	1.005	0.861	[176]
Fe-Zn-SA/NC	Fe-Zn dual-metal sites	High-temperature pyrolysis method	0.1 M KOH, 0.1 M $HClO_4$, 0.1 M PBS	0.94, 0.87, 0.94	0.85, 0.78, 0.72	[177]
MnFe-PNC	Mn-N_3P and Fe-N_3P	Metal-organic framework pyrolysis strategy	0.1 M KOH, 0.1 M $HClO_4$, 1 M PBS	—, —, —	0.923, 0.803, 0.774	[162]
Fe,Cu/N-C	Fe and Cu	High-temperature pyrolysis method	0.1M KOH, 0.5 M H_2SO_4, 0.1 M PBS	—, —, —	0.86, 0.74, 0.73	[161]
PtFeNC	Pt and Fe atoms	High-temperature pyrolysis method	0.1 M KOH	1.05	0.892	[178]
IrCo-N-C	Ir-Co site	—	0.1 M KOH	1	0.911	[63]
Pt_1Co_{100}/N-GCNT	Pt-Co dual sites	High-temperature pyrolysis method	0.1 M $HClO_4$	—	0.85	[179]
ZnCo-NC-II	ZnN_4 and CoN_4	Cavity confinement and post-adsorption method	0.1 M KOH, 0.5 M H_2SO_4	0.97, 0.94	0.86, 0.79	[47]
NiCo DASs/N-C	NiN_4 and CoN_4	Host-guest strategy	0.1 M KOH, 0.5 M H_2SO_4	—, —	0.88, 0.754	[49]
CoFe-N-C	Co and Fe site	Two-step pyrolysis process	0.1 M KOH	—	0.897	[77]
Fe_1Se_1-NC	Fe-Se	High-temperature pyrolysis method	0.1 M KOH	1	0.88	[180]
Fe-Co-DSAC	FeN_4S_1 and CoN_4S_1	High-temperature pyrolysis method	0.1 M KOH	—	0.86	[89]
Fe,Co SAs PNCF	N_3-Fe-Co-N_3	Electrostatic spinning method	0.1 M KOH, 0.1 M $HClO_4$	1.04, 0.94	0.93, 0.78	[181]
$FeCoN_5P_1$	$FeCoN_5P_1$	High-temperature pyrolysis method	0.5 M H_2SO_4	0.899	0.816	[182]
FeCo-NC	FeCo-N_6	High-temperature pyrolysis method	0.1 M KOH	1.05	0.877	[183]

(Continued)

Catalyst	Active sites	Synthetic method	Electrolyte	E_{onset} (V)	$E_{1/2}$ (V)	Ref.
Fe-Mn-N-C	Fe-Mn	High-temperature pyrolysis method	0.1 M $HClO_4$, 0.1 M KOH	1, —	0.79, 0.93	[64]
FeMo-N-C	$FeMoN_6$	subject-object strategy	0.1 M $HClO_4$	0.98	0.84	[66]
Fe&Mn/N-C	FeN_4-O-MnN_4	High-temperature pyrolysis method	0.1 M KOH, 0.1 M $HClO_4$	1.015, 0.948	0.904, 0.781	[184]
CNS_{FeZnN}	N>Fe≫Zn	High-temperature pyrolysis method	0.1 M KOH	0.95	0.84	[185]
Fe/Zn-N-C	FeN_4	High-temperature pyrolysis method	0.1 M KOH, 0.1M $HClO_4$	—, —	0.906, 0.8	[186]
FeCu NC	Fe-N_4 and Cu-N_4	High-temperature pyrolysis method	0.1M KOH	—	0.882	[75]
Cu-Se DAs	Cu-N_4 and Se-C_3	high-temperature pyrolysis method	0.1M KOH	—	0.905	[187]
DAC-Fe-Cu	Fe-Cu	High-temperature pyrolysis method	0.1M $HClO_4$	—	0.793	[188]
Fe/Zr-N-C	N_2(N)-Fe-N_2-Zr-N_2(O_2)	High-temperature pyrolysis method	0.1M $HClO_4$	—	0.872	[189]
C-Zn/Co800	Zn-Co	High-temperature pyrolysis method	0.1 M KOH	0.92	0.75	[68]
Fe_2@P-HC	Fe_2N_5P	High-temperature pyrolysis method	0.1 M KOH, 0.1M $HClO_4$	0.96, 0.82	0.89, 0.75	[50]
FeCo-MHs	FeCo	Two-step specific-adsorption strategy	0.1 M KOH	1.05	0.95	[51]
Cu-Co/NC	CuN_4 and CoN_4	High-temperature pyrolysis method	0.1 M KOH, 0.5 M H_2SO_4	1.1, 0.97	0.92, 0.85	[88]
Fe,Cu DAs-NC	FeN_4 and CuN_4	Multi-step collaborative synthesis strategy	0.1 M KOH	1.08	0.94	[86]
Ni,Fe-DSAs/NCs	Ni/Fe NCs and NiN_4/FeN_4	High-temperature pyrolysis method	—	—	0.895	[190]
RuFe-N-C	—	High-temperature pyrolysis method	0.1 M KOH	1.04	0.92	[79]
Sb-SeNC	SbN_2C_2 and SeC_2	High-temperature pyrolysis method	0.1 M KOH	—	0.865	[191]
Co_2P/CoN_4@NSC-500	Co_2P and CoN_4	High-temperature pyrolysis method	0.1 M KOH	1.06	0.94	[192]
FeCu-SAC	FeN_4 and CuN_4	Modified ligand-mediated method	0.1 M KOH	—	0.926	[193]
Fe_1Se_1-NC	Fe-N_5 and SeC_2	high-temperature pyrolysis method	0.1 M KOH	1.0	0.88	[180]
FeCo-N-C	Co and Fe site	High-temperature pyrolysis method	0.1 M KOH	1.07	0.853	[69]
Fe/Sn(0.14)-PNC	Fe-N_4 and Sn-N_x sites	High-temperature pyrolysis method	0.1M KOH	0.96	0.84	[194]
Fe/Co-SAs-N_x-PCNSs	Fe and Co site	Spatial confinement and thermal activiation	0.1 M KOH, 0.1 M $HClO_4$	1.02, 0.95	0.91, 0.8	[195]
FeCo-NC DAC	Fe-Co	Post-modification strategy	0.1 M KOH	—	0.91	[196]
FeCo-SAs	N_3-Fe-Co-N_4	High-temperature pyrolysis method	0.1 M KOH	—	0.884	[197]
Ce-Se DAs/NC	Ce SA and Se SA	High-temperature pyrolysis method	0.1 M KOH	—	0.886	[198]
PtCo/P_yO_x-KB	P-O and PtCo nanoparticles	Solvothermal method	0.1 M $HClO_4$	—	0.928	[134]
Fe_2/NC	Fe atoms or Fe_2 sites	Sublimation transformation strategy	0.1 M KOH	—	0.92	[36]
Fe_1Sn_1-DAC	Fe and Sn sites	General metal ion recognition strategy	0.1 M KOH	1.02	0.85	[133]
FeCu-NC	FeN_3O-CuN_4	High-temperature pyrolysis method	0.1M KOH	—	0.91	[65]
FeRu-N-C	Fe-Ru	High-temperature pyrolysis method	0.1 M $HClO_4$	1.02	0.86	[87]
PtFe-DAC	$PtFeN_6$ site	High-temperature pyrolysis method	0.1 M KOH	1.04	0.935	[80]
FeAl-RNC	Fe-Al	High-temperature pyrolysis method	0.1 M KOH, 0.5 M H_2SO_4	—, —	0.92, 0.83	[84]
FeMn-N-C	Fe-Mn	Electrospinning-pyrolysis-etching method	0.1M KOH	1.05	0.92	[108]
Fe-Rh_x@NC	Fe-Rh	Spatial confinement strategy	0.1 M KOH	1.01	0.91	[199]
FeNb/c-SNC	Fe-S_1N_3 and Nb-N_4	high-temperature pyrolysis method	0.1 M KOH	1.05	0.922	[81]
Fe_1Cu SAA/NC	Fe-Cu	Wet chemistry pyrolysis method	0.1 M KOH	1.106	0.917	[200]
Fe-Sn-N/C	SnN_4 and FeN_4	high-temperature pyrolysis method	0.1 M KOH, 0.1 M $HClO_4$	—, —	0.92, 0.83	[160]
SeFe-C_2N	Fe and Se sites	High-temperature pyrolysis method	0.1 M KOH	—	0.926	[5]
Co_2-N-HCS-900	Co_2N_5	Double-solvent impregnation method	0.1 M KOH	0.99	0.86	[37]
Fe_2-S_1N_5/SNC	Fe_2-S_1N_5	High-temperature pyrolysis method	0.1 M $HClO_4$	0.929	0.829	[58]
FeSn-C_2N	FeSn	Two-step pyrolysis procedure	0.1 M KOH	—	0.912	[59]
P-FeCo/NC	Fe-P-Co	High-temperature pyrolysis method	0.1 M KOH	1.01	0.95	[60]
FeCo-N_3O_3@C	Fe-N_3 and Co-O_3	One-pot method	0.1 M KOH	—	0.936	[61]
CoMn-N/S-C	CoN_3S-MnN_2S_2	High-temperature pyrolysis method	O_2-saturated 0.1 M KOH	0.936	0.883	[62]
$FeMn_{DSA}$/*d*NC	FeMn dual-atom pairs	High-temperature pyrolysis method	O_2-saturated 0.1 M KOH	1.004	0.921	[201]
Fe-Co DACs	Fe-N_3 and Co-N_3	Molecular chelation and ionic coupling strategies	O_2-saturated 0.5 M H_2SO_4	—	0.852	[163]

specifically chosen to elucidate the mechanisms responsible for the excellent ORR activity of carbon-based ADCs.

By adding Nb and S atoms to a concave cubic carbon support generated from MOF, Chen and co-workers created an asymmetric Fe-Nb double-atom-dot catalyst (referred to as FeNb/c-SNC) [81]. The catalyst exhibits record alkaline ORR activity ($E_{1/2}$ = 0.922 V, Tafel slope = 52 mV·dec^{-1}) (Fig. 12(a)). The practical application of FeNb/c-SNC catalyst was explored by using in zinc-air battery (ZAB) devices (Fig. 12(b)). These results can demonstrate that FeNb/c-SNC not only has an excellent intrinsic ORR performance but also has great application potential in practical battery devices by the analysis of the polarization curves, power density curves and stability test. Theoretical analysis reveals Nb optimizes *OH adsorption via d-band regulation (volcano apex, Fig. 12(c)). COHP confirms strengthened Fe–N bonding (Fig. 12(d)). This work establishes a new paradigm for Fe-based ADCs, outperforming PtFe-DAC ($E_{1/2}$ = 0.935 V), FeMn-N-C/Fe-Sn-N/C ($E_{1/2}$ = 0.92 V), and FeCu/N-C ($E_{1/2}$ = 0.86 V) [80, 108, 160, 161].

Fe_2-S_1N_5/SNC ADCs exhibits high acidic ORR performance with $E_{1/2}$ of 0.829 V and onset potentials of 0.929 V (Fig. 12(e)), with accelerated kinetics confirmed by Tafel analysis [58]. In PEMFCs, it demonstrates exceptional activity/stability. *In situ* EXAFS oscillation was used to observe the change in active site structure in ORR. Three distinct peaks that represent the Fe-N, Fe-S, and Fe-Fe shells, respectively (Fig. 12(f)). The dynamic changes of Fe-Fe shell in ORR process can be explained by the stretching or compression of the Fe–Fe bonds, induced by dynamic reaction processes. The ΔG_{PDS} of the other three reaction routes on Fe_2-S_1N_5/SNC is likewise smaller than that of Fe-S_1N_3/SNC and Fe-N_4/NC, according to theoretical calculations (Fig. 12(g)). Based on the changes of free energy, the changes in OH* adsorption capabilities during the PDS was used to endeavor to comprehend the ORR activity (Fig. 12(h)). The ΔG_{OH^*} of Fe_2-S_1N_5/SNC (0.93 eV) was significantly higher than Fe-N_4/NC (0.54 eV) and Fe-S_1N_3/SNC (0.49 eV). The weak adsorption of OH* enhanced the ORR activity of Fe_2-S_1N_5/SNC catalyst. Therefore, the precise construction of active sites in homonuclear Fe_2-S_1N_5/SNC ADCs leads to superior ORR activity.

Another example is CoMn-N/S-C catalyst with atomically distributed CoN_3S-MnN_2S_2 bimetallic sites [62]. The catalyst exhibits superior alkaline ORR activity (Tafel slope, TOF and EIS verified) (Fig. 12(i)). When CoMn-N/S-C catalyst was assembled into ZABs, which exhibits higher maximum power density (203 mW·cm^{-2}) than that of the commercial Pt/C-based ZAB (131 mW·cm^{-2}) (Fig. 12(j)). DFT calculations were performed to explore the intrinsic activity of the heteronuclear CoMn-N/S-C ADCs. CoN_3S-MnN_2S_2 exhibits a steady downward trend at U = 0.46 V, as shown by the Gibbs free energy diagram (Fig. 12(k)). DFT calculations suggest that the synergistic effect of the Mn and S atoms can induce the asymmetric electron distribution of the Co site and optimize its desorption ability to the *OH intermediate, resulting in good catalytic activity. The electron distribution of the Co site suggests an obvious interaction of the asymmetrical coordination environment and Co site in CoMn-N/S-C (Fig. 12(l)).

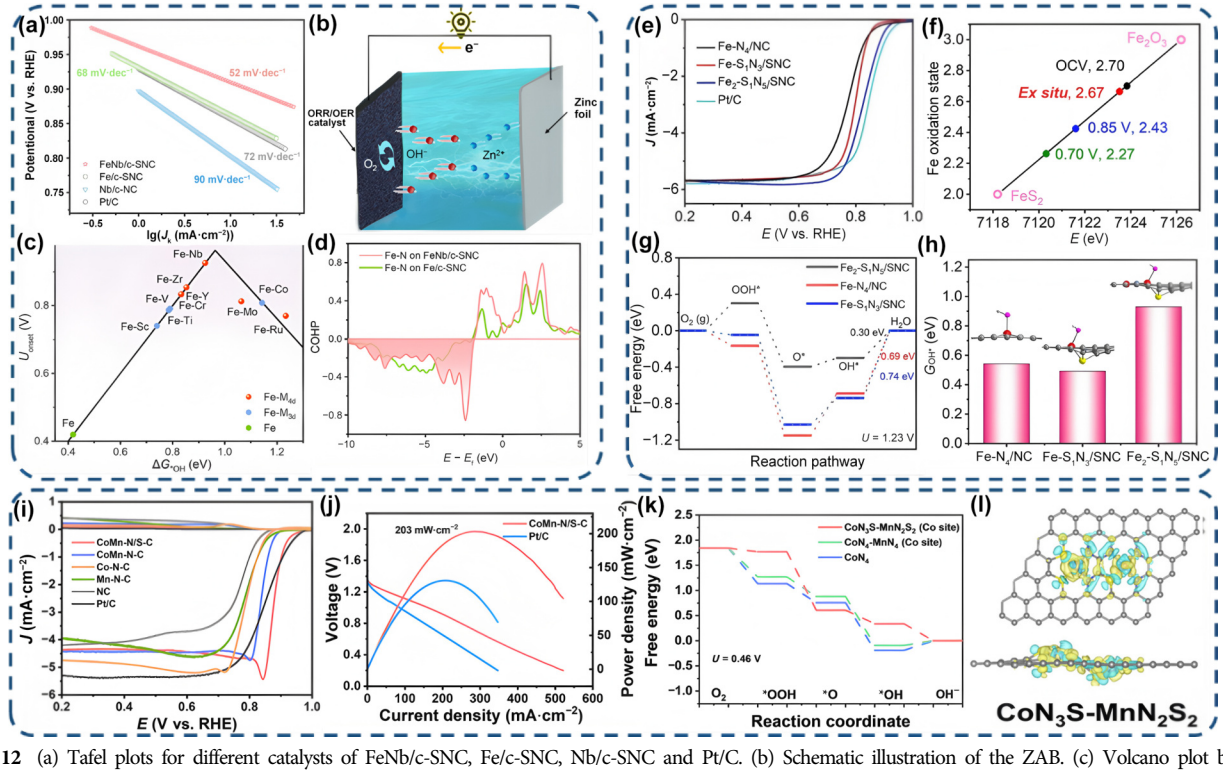

Figure 12 (a) Tafel plots for different catalysts of FeNb/c-SNC, Fe/c-SNC, Nb/c-SNC and Pt/C. (b) Schematic illustration of the ZAB. (c) Volcano plot by DFT theoretical calculations. (d) COHP analysis of Fe-N on Fe-Nb-S-NC and Fe-S-NC. Reproduced with permission from Ref. [81], © American Chemical Society 2024. (e) Polarization curves in ORR performance of Fe-N_4/NC, Fe-S_1N_3/SNC, Pt/C and Fe_2-S_1N_5/SNC were recorded at a rotation speed of 1600 rpm. (f) Correlation between the Fe oxidation state and the energy position of the XANES spectrum of Fe_2-S_1N_5/SNC structure at different applied potentials. (g) The free energy changes of four reaction paths on Fe_2-S_1N_5/SNC. (h) The free energy bar diagram of OH* on Fe-N_4/NC, Fe-S_1N_3/SNC, and Fe_2-S_1N_5/SNC. Reproduced with permission from Ref. [58], © The Royal Society of Chemistry 2024. (i) LSV curves with 95% *iR* correction for CoMn-N/S-C and other catalyst in O_2-saturated 0.1 M KOH. (j) The discharge polarization curves and corresponding power density curves. (k) Free energy diagrams of CoN_4, CoN_4-MnN_4, and $CoN_3SMnN_2S_2$ at U = 0.46 V. (l) Charge density difference diagrams of CoN_3S-MnN_2S_2. Reproduced with permission from Ref. [62], © Tsinghua University Press 2024.

The asymmetric decoration of S atom for Co in CoMn-N/S-C induces the Co center more positive, weakening the adsorption of *OH intermediate and lowering the reaction energy barrier. The d-band center of the Co center can be reduced by the asymmetric coordination, and optimize the desorption behavior of *OH intermediate, which promotes the ORR process of CoMn-N/S-C.

From Table 2, it can be observed that most ADCs used for ORR operate under either acidic or alkaline conditions, while studies simultaneously investigating ORR in acidic, alkaline, and neutral electrolytic conditions are relatively rare [161, 162]. Wang and co-workers reported one asymmetric Mn/Fe dual single-atom catalysts by an MOF-derived strategy for pH-universal ORR [162]. The LSV curve of MnFe-PNC catalyst displays the most positive $E_{1/2}$ of 0.923 V in 0.1 M KOH (Fig. 13(a)), 0.803 V in 0.1 M $HClO_4$, and 0.774 V in 1 M phosphate buffer solution. Eight optimized models were established by the P doping position in DFT calculations. Whether Mn-N_3P and Fe-N_3P in MnFe-PNC are directly connected, their interaction distances are different (short-range: 4.34 A; medium-range: 4.89 Å; a long-range: > 5 Å) (Fig. 13(b)). Fe site shows the stronger adsorption strength than Mn sites in all the catalyst models, which can attribute to their difference in valence electron structure (Fig. 13(c)). The scatter of the rate-determining steps on Mn and Fe atoms mainly distributes in the area of *OH → OH^- from the heat map of overpotential against ΔG_{*OH} and μ (Fig. 13(d)). Comprehensive theoretical calculations demonstrate that the atomic distance-dependent effects through electronic interactions in integrating Fe-N_3P and Mn-N_3P. This study deepens the fundamental understanding of the distance-dependent electronic interactions in ADCs.

Yuan and co-workers synthesized alloyed *T*-FeCo-N-C with strong and directly connected Fe-Co bonds by molecular chelation and ionic coupling strategies (Figs. 13(e) and 13(f)) [163]. The *T*-FeCo-N-C catalyst exhibits the highest catalytic activity and the $E_{1/2}$ up to 0.852 V in acidic ORR performance (Fig. 13(g)). Meanwhile, the catalyst shows a similar electrochemical active area 22.3 mF·cm^{-2}, the data illustrates the highest intrinsic catalytic activity in *T*-FeCo-N-C. The Fe-Co dual-atom sites in alloyed catalyst reveals the Janus effect by the characterization of *in situ* spectroscopy and theoretical calculation. The Co atom serves as the main active center and the Fe atom forms a stable adsorption structure is obtained in the *in situ* ATR-SEIRAS and *in situ* synchrotron-based XAS analysis. The DFT calculations explore the intrinsic catalytic mechanism by the Janus effect of Fe-Co dual-atom sites in alloyed *T*-FeCo-N-C catalyst. From our calculated DFT results, it can be seen that both of pathways I and II exhibit a high overpotential of 1.14 V in Fig. 13(h). And pathways I and II plays a crucial role in the electron rearrangement of Fe-Co active centers in *T*-FeCo-N-C, and their appropriate interaction with the reaction intermediates significantly accelerates the reaction kinetics. The finding Janus effect in dual-atom center has clarified the identification of the configuration-mechanism relationship and guided the design of high-performance ADCs.

Li and co-workers utilized a pH-field coupled microkinetic model to guide the rational design of DACs for ORR with optimal active sites [164]. pH-field activity volcano for DACs was established by the potential of zero charge (PZC) values and their corresponding scaling relationships (Fig. 13(i)). The modeling of the ORR activity achieved a very wide pH range of 13.4 to 1.3

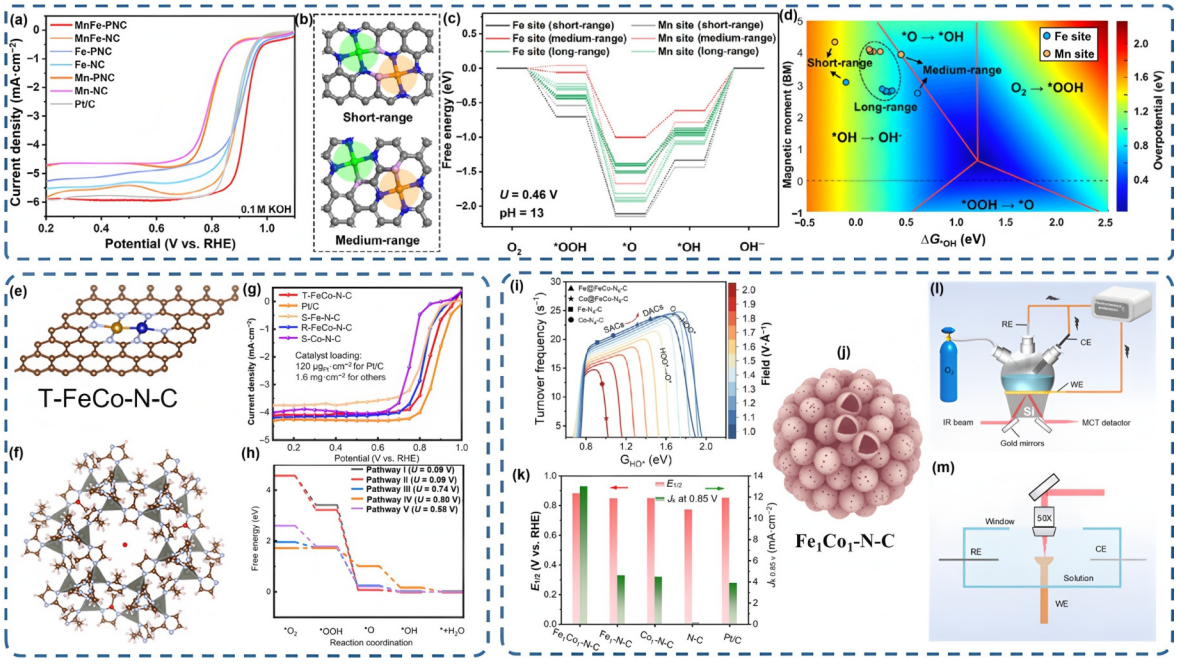

Figure 13 (a) LSV curves of MnFe-PNC, MnFe-NC, Fe-PNC, Fe-NC, Mn-PNC, Mn-NC, and Pt/C catalysts for ORR in 0.1 m KOH. (b) Schematic diagram of short-range and medium-range models. The green, orange, green, pink, blue, and gray balls represent Mn, Fe, P, and C atoms, respectively. (c) Free energy diagrams for ORR on Fe sites and Mn sites. (d) Heat map of overpotential against ΔG_{*OH} and magnetic moment. Reproduced with permission from Ref. [162], © Wiley-VCH GmbH 2025. (e) and (f) The synthesis T-FeCo-N-C by the molecular chelation strategy. (g) ORR polarization curves for different samples in O_2-saturated 0.5 M H_2SO_4 electrolyte. (h) The ORR free energy diagrams of five different pathways considered here, for the Fe-NC, FeCo-NC, and FeCo-NC-OH catalysts. Reproduced with permission from Ref. [163], © Wiley-VCH GmbH 2025. (i) pH-field activity volcano for DACs, highlighting enhanced positioning of the Fe/Co atop site towards peak activity in alkaline solutions. (j) The construction of a porous Fe_1Co_1-N-C DAC by a hard-template method following a CO_2 activation process. (k) Comparison of $E_{1/2}$ and J_k at 0.85 V for Fe_1Co_1-N-C and reference samples (Fe_1-N-C, Co_1-N-C, and Pt/C). (l) and (m) Scheme of the *in situ* ATR-SEIRAS and *in situ* Raman spectroscopy equipment. Reproduced with permission from Ref. [164], © The Royal Society of Chemistry 2025.

through the electric field range of 1.0 to 2.0 V·Å^{-1}, and emphasized the enhancement positioning of the Fe/Co atop site towards peak activity in alkaline solutions. The performance of the active sites in Fe_1-Co_1-N-C is excellent by the obtained optimal adsorption free energy of HO* (1.6 eV) for the most active reaction sites in the ORR volcano plot. A porous Fe_1-Co_1-N-C was constructed by hard-template method and CO_2 activation process (Fig. 13(j)). Interconnected vesicular structure with well-defined mesopores was observed by the microstructure investigation of TEM. The ORR catalytic activity was evaluated by LSV, and it was proved that Fe_1Co_1-N-C DAC exhibits a more positive E_{onset} (1.00 V) and $E_{1/2}$ (0.882 V) than those of other tested catalysts (Fig. 13(k)). Fe_1Co_1-N-C shows a high-efficiency 4e$^-$ ORR pathway and exhibits high selectivity for reducing O_2 to OH^-. Further *in situ* ATR-SEIRAS tests (Fig. 13(l)) and *in situ* Raman spectroscopy tests (Fig. 13(m)) during electrochemical experiments consistent with the proposed ORR mechanism used in the pH-field coupled microkinetic model. The Fe_1Co_1-N-C catalyst participates in the typical 4e$^-$ ORR process, which involves the adsorption of O_2*, the formation of HOO*, the breaking of the O–O bond within HOO*, and the elimination of HO*.

5.2 CO_2RR

The CO_2RR is a potential approach to solve the current energy crisis and carbon emission problems and achieve a carbon-neutral energy cycle [126, 202–208]. single-atom catalysts have attracted attention due to their adjustable active sites and high atomic utilization efficiency [206, 209–212]. However, in multi-intermediate reactions, the presence of single-type active sites limits further development, as it is difficult to achieve optimal adsorption of all reaction intermediates [213, 214]. ADCs, on the other hand, contain two metal atoms with asymmetric structures and electronic properties. These two atoms can act synergistically, with one activating the carbon dioxide molecule and the other promoting the conversion of intermediates, thus accelerating the reaction kinetics [159, 215–217]. The asymmetric electronic structure of ADCs can also adjust the binding energy between active sites and intermediates, control the reaction pathway, and improve the selectivity of target products. ADC_S can achieve high Faradaic efficiency at relatively low potentials. Their Faradaic efficiency for target products, such as carbon monoxide and formic acid, exceeds that of traditional catalysts, and they also exhibit excellent electrochemical stability. Although the application of ADCs in CO_2RR is currently in its infancy, they are expected to become a major trend in future CO_2RR research due to their excellent performance in terms of activity, selectivity, and stability. In this section, we will comprehensively review the progress and prospects of ADCs in CO_2RR. The reported ADCs for CO_2RR are summarized in Table 3, where we have selected five embodiments to illustrate the reasons for the excellent CO_2RR performance of ADCs.

Table 3 Summary of the CO_2RR performance of carbon-based ADCs catalysts along with the corresponding synthesis method, active sites, electrolyte, potential, and FE(product) (%)

Catalyst	Active site	Synthetic method	Electrolyte	Potential (V)	FE (%)	Ref.
Cu-S-Ni/SNC	N_2Cu-S-NiN_2	Freeze-drying and annealing	0.1M $KHCO_3$	−0.65	98.1(CO)	[52]
Cu_2-SNC	CuN_2-CuNS	Reverse-micelle assembly-pyrolysis strategy	0.1M $KHCO_3$	−0.8	62.8(ethanol)	[32]
Zn_1Mn_1-SNC	S/N-coordinated ZnMn	A two-step ligand etch-pyrolysis	0.1M $KHCO_3$	−0.453	97(CO)	[53]
Fe_1-Ni_1-N-C	Fe-N_4 and Ni-N_4	Zn-assisted atomization method	0.5M $KHCO_3$	−0.5	96.2(CO)	[44]
NiFe-DASC	Ni and Fe supported on N-doped graphene	High-temperature pyrolysis strategy	0.5M $KHCO_3$	−0.8	94.5(CO)	[46]
Ni/Fe-N/O-C	Ni and Fe anchored on N/O sites	A two-step wet-chemistry method	0.5M $KHCO_3$	−0.5	99.8(CO)	[45]
Ag-MoPc	Ag and Mo	DFT and ML	—	−0.33	94.3(CO)	[128]
Cu-Fe-N_6-C	CuN_3 and FeN_3	Stirred and annealing treatment	0.5M $KHCO_3$	−0.7	98(CO)	[231]
Fe/Cu-N-C	N_4Fe-CuN_3	Metal-organic framework-assisted synthesis	0.1M $KHCO_3$	−0.8	99(CO)	[70]
NiZn-NC	Ni-Zn-N_6-C	Competitive complexation strategy	0.5M $KHCO_3$	−0.8	99(CO)	[232]
Fe/Mn-NC	Fe/Mn supported on N-doped carbon	Commercial carbon black	0.5M $KHCO_3$	−0.48	95.7(CO)	[233]
CoCu DASC	CoCu-N	Pyrolysis and thermal decomposition	0.5M $KHCO_3$	0.6	99.2(CO)	[83]
Cu_2	copper atoms	The expanded and fluorinated porphyrin structure	0.1M $KHCO_3$	−1.2	35.3(ethanol)	[74]
CuNi NC	CuNi-N_3	A pre-growth-pyrolysis process	0.1M $KHCO_3$	−1.1	99(CO)	[72]
Cu-Ni-DSA-CNFs	CuN_4-NiN_4	Electrospinning technology and chemical vapor deposition	0.1M $KHCO_3$	−0.98	99.6(CO)	[234]
InNi DS/NC	O-In-N_6-Ni	Pyrolyzing zeolitic imidazolate framework	0.5M $KHCO_3$	−0.7	96.7(CO)	[215]
Ni/Mn-N-C	Ni-N-C and Mn-N-C	High-temperature pyrolysis method	0.5M $KHCO_3$	−0.76	96.6(CO)	[235]
MoSA-SeSA	MoN_4-SeN_2	Organic-inorganic multi-conversion method	0.1M $KHCO_3$	−0.6	98.3(CO)	[236]
Ni/Cu-N-C	NiCuN_6	High-temperature pyrolysis method	0.5M $KHCO_3$	−0.7	97.7(CO)	[237]
NiMn@V-g-C_3N_4	NiMn doped on graphitic carbon nitride	High-temperature pyrolysis method	0.1M $KHCO_3$	−0.55	95(ethanol)	[71]

(Continued)

Catalyst	Active site	Synthetic method	Electrolyte	Potential (V)	FE (%)	Ref.
Ni_2-N_xC_y	Ni_2 supported on nitrogen-doped carbon	Pyrolyzing the dinuclear nickel complex	0.5 M $KHCO_3$	0.88	98.9(CO)	[104]
Ni-Ag/PC-N	N_3-Ni-Ag-N_3	High-temperature pyrolysis method	0.1 M $KHCO_3$	−0.8	99.2(CO)	[238]
CuSn/NPC	Cu-Sn supported on N-doped carbon	The dissolution-carbonization method	0.1 M $KHCO_3$	−0.75	99.1(CO)	[216]
CuZn-DAS/NC	CuN_4-ZnN_4	High-temperature pyrolysis method	1 M KOH	−0.6	98.4(CO)	[239]
CuN_4-MN_4	Cu and M supported on N-doped graphene	Density functional theory calculations	0.5 M $KHCO_3$	—	—	[240]
DMCP Fe_1-Mo_1-NC	Fe_1-Mo_1 bimetallic catalytic pair	High-temperature pyrolysis method	0.5 M $KHCO_3$	−1	99.5(CO)	[217]
D-Co/CNT	Double Co atomic sites	Non-covalent anchoring strategy	0.5 M $KHCO_3$	−0.7	91.76(CO)	[241]
NiN_3-CoN_3-NC	Ni-Co atomic pair sites	Cation exchange and cavity adsorption strategy	0.1M $KHCO_3$	0.7	97(CO)	[242]
TeN_2-CuN_3	TeN_2-CuN_3 dual-atomic sites	Sacrificial template and the double-solvent impregnation	0.1 M $KHCO_3$	−0.65	98(CO)	[243]
Zn_1Mn_1-SNC	Zn-N and Mn-N and Zn-S and Mn-S	A two-step ligand etching-pyrolysis method	0.1 M $KHCO_3$	0.435	97(CO)	[53]
NiM-HDAC	Ni and M (Cd, Pt or Pd) diatomic sites	Combination of complexation and pyrolysis methods	0.1 M $KHCO_3$	−0.75	97.1(CO)	[244]
Pr/Ni-NC	Pr-N_4C_2 and Ni-N_4	Improved precipitation-pyrolysis method	0.1 M $KHCO_3$	−0.8–1.1	~ 100(CO)	[110]
Pr/Ni-NC	Co-Ni-N_6	Pyrolysis of ZIF Precursors	0.1 M $KHCO_3$	−0.8	94.1(CO)	[55]
PdZn-N-CMK-3-D	Pd-Zn	High-temperature pyrolysis method	0.5 M $KHCO_3$	−0.52	97.14(CO)	[159]
np-Ag/SnCu	Ag and Sn modified sites on the Cu	Dealloying method of selective etching of Zr atoms	1 M KOH	0.3–1.6	~ 100(CO)	[245]
CoCu-DASC	Co-Cu hetero-diatomic pairs	High-temperature pyrolysis method	0.5 M $KHCO_3$	2.5	99.1(CO)	[83]
Cu-Fe-N_6-C	Cu-Fe diatomic sites coordinated with N	High-temperature pyrolysis method	0.1 M $KHCO_3$	−0.7	98(CO)	[231]
CuNi-DSA/CNFs	CuN_4 and NiN_4	Electrospinning technology and chemical vapor deposition	0.1 M $KHCO_3$	−0.98	99.6(CO)	[234]
Fe_1-Ni_1-N-C	FeN_4 and NiN_4	Zn-assisted atomization strategy	0.5 M $KHCO_3$	−0.5	96.2(CO)	[44]
NiCu-N-C	$NiCuN_6$	A host-guest strategy	0.5 M $KHCO_3$	−0.7	97.7(CO)	[237]
NiFe-DASC	NiN_4 and FeN_4	High-temperature pyrolysis method	0.5 M $KHCO_3$	−0.8	94.5(CO)	[46]
Ni-Zn-N-C	$NiZnN_6$-C	High-temperature pyrolysis method	0.5 M $KHCO_3$	−0.8	99(CO)	[232]
ZnCoNC	Zn and Co	Pyrolysis and acid treatment method	0.5 M $KHCO_3$	−0.5	93.2(CO)	[246]
Zn_1Sn_1/SNC	Zn-Sn bimetallic sites	One-step ligand co-etching method	0.1 M $KHCO_3$	−0.84	94.6(formate)	[247]
Cu/Ni-NC	Ni-NC and Cu-NC	Pregrowth-pyrolysis process	Phosphate buffer, 1M KOH, 0.5 M $KHCO_3$	−1.1 −0.7 −1.2	98.5(CO) 99(CO) 99(CO)	[72]

In 2024, Sun and co-works developed an catalyst (Cu-S-Ni/SNC) with sulfur-bridged Cu-S-Ni bimetallic atom sites (Fig. 14(a)) [52]. The CO_2RR performance of Cu-S-Ni/SNC was tested in a near-neutral electrolyte solution of 0.1 M $KHCO_3$ saturated CO_2 (pH = 6.8). The S-bridged Cu-S-Ni metal site has the best catalytic activity and the highest current density in the LSV measurement from 0 to −1.0 V (versus RHE) (Fig. 14(b)). Compared with CuNi/NC, Cu/SNC and Ni/SNC catalysts, Cu-S-Ni/SNC has outstanding selectivity advantages in the CO_2RR reaction to produce CO a higher peak of 98.1% FE_{CO} at −0.65 V. The reaction mechanism was explored through *in situ* XAS, ATR-SEIRAS and DFT calculations. The *in situ* characterization revealed that the oxidation states of Cu and Ni changed during the reaction, with Cu being the main active site. ATR-SEIRAS was conducted to detect the real-time adsorption and conversion of key reaction intermediates during the reaction process from open-circuit potential OCP to −1.0 V range, indicating that the reaction mainly occurred at the Cu metal site. With the gradual increase in potential, the absorption peak of CO_2 at 2345 cm^{-1} gradually disappeared, while the CO peak 1915 cm^{-1} was enhanced, indicating a strengthened interaction between the CO intermediate and the Cu-S-Ni sites. DFT calculations containing ΔU value, local density of states (DOS), charge density difference and electron density difference showed that the asymmetric N_2Cu-S-NiN_2 site had a low formation energy barrier. During the CO_2RR process, Cu was dual-regulated by S and Ni atoms, which enhanced the adsorption of CO_2 and reduced the energy barrier of CO_2* protonation (Fig. 14(c)). Besides, the charge asymmetry in Cu-S-Ni sites can be observed through the electron

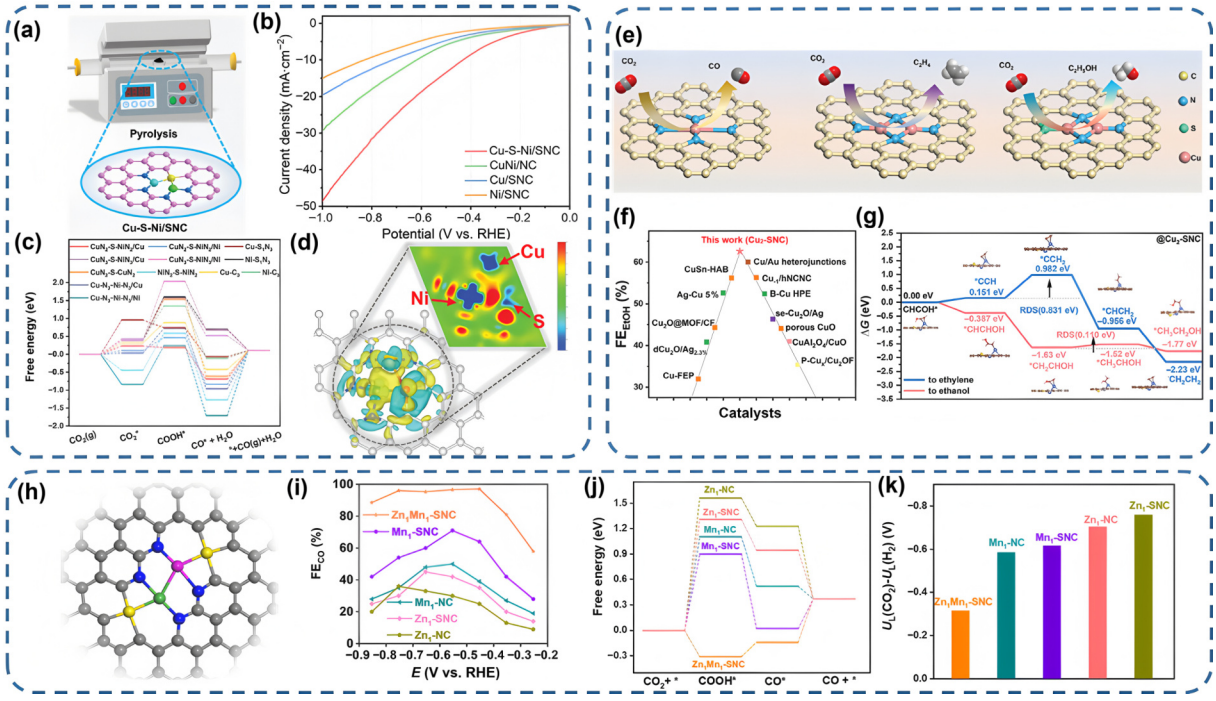

Figure 14 (a) The prepared Cu-S-Ni/SNC by using wool keratin biomass as the base material. (b) LSV curves of Cu-S-Ni/SNC, CuNi/CN, Cu/SCN and Ni/SCN. (c) Free energy diagrams of CuN_2-S-NiN_2 and various reference active sites for CO_2RR to CO in the theoretical calculation. (d) Electron density difference plot of Cu-S-Ni site. Reproduced with permission from Ref. [52], © Wiley-VCH GmbH 2024. (e) The scheme of the selectivity of various products on Cu-NC, Cu_2-NC, and Cu_2-SNC catalysts. (f) FE_{EtOH} for reported Cu-based catalysts and Cu_2-SNC catalysts. (g) Gibbs free energy profiles of all intermediates for the formation of CH_3CH_2OH on Cu_2-SNC. Reproduced with permission from Ref. [32], © Wiley-VCH GmbH 2024. (h) Structure model of the Zn_1Mn_1-SNC dual site (Mn green, Zn purple, N blue, S yellow, C gray). (i) FE_{CO} of Zn_1Mn_1-SNC, Mn_1-SNC, Mn_1-NC, Zn_1-SNC, and Zn_1-NC catalysts. (j) Calculated PES for CO_2RR to CO on the five atomic catalysts in theoretical simulations. (k) Limiting potential difference for CO_2 reduction and HER on the five atomic catalysts. Reproduced with permission from Ref. [53], © Wiley-VCH GmbH 2023.

density difference map (Fig. 14(d)), which emphasize the important regulating role of the S-bridged in electron transfer and charge distribution among the Cu and Ni atoms.

Copper-based catalysts are the choice for producing multi-carbon products during CO_2RR due to its controllable potential of local surface environment, suitable potential of multi-electron reduction and efficient promotion of C–C coupling [11, 218–227]. Chen and co-workers reported a series of copper atom-dispersed catalysts were synthesized by regulating the coordination structure to optimize the selectivity of the CO_2RR in CO_2-saturated 0.1 M $KHCO_3$ [32]. The main products of Cu-NC, Cu_2-NC, and Cu_2-SNC catalysts in CO_2RR are CO, C_2H_4 and C_2H_5OH, respectively (Fig. 14(e)). The FE_{EtOH} of the Cu_2-SNC catalyst and many other reported copper-based catalysts are presented. It can be clearly seen from the figure that the FE_{EtOH} value of the Cu_2-SNC catalyst is significantly higher than that of Fig.14(f) that the FE_{EtOH} value of the Cu_2-SNC catalyst is significantly higher than those of many other comparative copper-based catalysts. DFT calculations show that the S doping in Cu_2-SNC leads to an asymmetric electron distribution around the Cu center, disrupting the chemical environment for the ethylene-forming pathway, making it unstable, and promoting the ethanol-forming pathway. The rate-determining step determines the selectivity of Cu_2-NC and Cu_2-SNC for ethylene and ethanol, respectively (Fig. 14(g)).

In 2024, Pie and colleagues developed an S, N-coordinated yolk-shell structured dual-atom catalyst (Zn_1Mn_1-SNC) using a two-step ligand etching-pyrolysis method [53]. XAS and quantitative EXAFS fitting (Fig. 14(h)) confirmed the coordination environment of Zn and Mn dual sites. Electrochemical measurements show that Zn_1Mn_1-SNC achieves a high Faradaic efficiency for CO (FE_{CO}) of 97% in a H-cell filled with argon-saturated 0.1 M $KHCO_3$ electrolyte (pH = 8.31), significantly outperforming four other catalysts (Fig. 14(i)). These advantages arise from the synergy between structural design and electronic regulation. The CO_2RR to CO involves two electron-proton transfer steps via intermediates like COOH* and CO*. DFT calculations reveal that the energy barriers for COOH* formation on single-atom Zn- and Mn-based catalysts are high: 1.56 (Zn_1-NC), 1.31 (Zn_1-SNC), 1.10 (Mn_1-NC), and 0.90 eV (Mn_1-SNC) (Fig. 14(j)), indicating weak COOH* binding and poor activity. In contrast, Zn_1Mn_1-SNC shows a much lower energy barrier of only −0.31 eV for COOH* formation, suggesting significantly enhanced adsorption. Bader charge analysis supports this, showing that the synergistic interaction between Zn and Mn sites improves the *COOH formation step. According to the free-energy diagram, Zn_1Mn_1-SNC exhibits higher CO_2RR selectivity with the most positive $U_L(CO_2)$-$U_L(H_2)$ value compared to other catalysts (Fig. 14(k)). Theoretical analysis further shows that the asymmetric coordination of Zn and Mn dual sites enhances CO_2RR activity while suppressing the competing HER. Despite these advances, CO_2RR research on ADCs remains in its early stages due to the complexity of the reaction mechanism. Further exploration of ADCs for CO_2RR is both necessary and challenging.

As shown in Table 3, most of the electrochemical ORR of ADCs are carried out under near-neutral and alkaline conditions, while reactions in acidic conditions are relatively rare. The development of CO_2RR under acidic conditions provides a more promising strategy compared to the unavoidable carbonate formation and low

CO_2 utilization efficiency in neutral or alkaline electrolytes. Zhang and colleagues designed Ni-Cu DAC supported on hollow nitrogen-doped carbon by a pregrowth-pyrolysis process for pH-universal CO_2 electroreduction to CO, effectively inhibiting the HER (Fig. 15(a)) [72]. The relatively larger FEs of Cu/Ni-NC and Ni-NC were presented than Cu-NC in full pH range containing acidic (a phosphate buffer at pH = 3.0), alkaline (1 M KOH, pH = 14.0) and neutral (0.5 M $KHCO_3$, pH = 7.5) conditions. The CO_2 utilization efficiency of Cu/Ni-NC catalyst in acidic conditions (64.3%) was about twice higher than that in alkaline electrolyte (33.0%) under an input flow of 5 sccm (Fig. 15(b)). The acidic system circumvent the CO_2 utilization limit in neutral and alkaline systems, thereby enhancing the efficiency of CO_2 utilization. To gain insight into the mechanism, *in situ* ATR-SEIRAS was used to detect reaction intermediates under acidic (Fig. 15(c)) and neutral conditions. Obviously, the absorption peaks of carbonate in acidic medium (1492 cm^{-1}) and those in neutral medium (1382 cm^{-1}) both gradually increase as the potential is more negative, indicating the typical carbonate production under alkaline conditions. The promising pH-universal CO_2 catalyst developed with high efficiency in this work inspires a new exploration for overcoming the CO_2 loss in electrolysis. Besides, the optimized Ni/Fe-N-C catalyst by a gas-phase chemical vapor deposition exhibited remarkable electrocatalytic performance for the CO_2RR, achieving a maximum FE_{CO} of 96% at a current density of 700 $mA{\cdot}cm^{-2}$ in a near-neutral electrolyte (0.1 M $KHCO_3$ saturated CO_2) and FE_{CO} of 95% at a CO partial current density close to 600 $mA{\cdot}cm^{-2}$ in a challenging acidic flow-cellelectrolyzer (0.025 M H_2SO_4 and 3 M KCl as the catholyte and 0.5 M H_2SO_4 as the anolyte) [228].

The *d*-electron coupling in ADCs plays a crucial role in enhancing the activity and selectivity of electrocatalytic CO_2RR. Professor Jun Li and his collaborators conducted extensive DFT calculations to systematically screen heteronuclear M_1/M_2-NC ADCs (M = V, Cr, Mn, Fe, Co, Ni, and Cu) loaded on nitrogen-doped graphene, in order to investigate their catalytic performance for CO_2RR [229]. The calculated the formation energies (E_f) and dissolution potentials (U_{diss}) can evaluate the thermodynamic stability ($E_f < 0$) and electrochemical stability ($U_{diss} > 0$). Apart from V/Cr-NC, V/Mn-NC and Cr/Mn-NC in the optimized 21 possible ADCs, all the other 18 types of ADCs exhibit both excellent thermodynamic and electrochemical stability (Fig. 15(d)). The eight ADCs highlighted in the red circle within the green shaded region are considered promising candidates for further investigation into their CO_2RRcatalytic activity by the comparation of the favorable formation energy ΔG_{*COOH} or ΔG_{*OCHO} with ΔG_{*H} (Fig. 15(e)). Mn/Cu-NC in the above eight ADCs is at the top of the volcano-type curve with the lowest U_L from the volcano-type curve relationship between E_{ads}(*OCHO) and U_L(HCOOH) in Fig. 15(f). Mn/Cu-NC exhibits superior catalytic activity and selectivity for the CO_2RR to product HCOOH, with the U_L values as low as −0.15 V. This outstanding performance is attributed to the d-electron coupling between the Mn and Cu atoms in Mn/Cu-NC, and further the d-band center of the Mn atom shifts close to the Fermi level. Figure 15(g) presented a negative linear relationship between the d-band centers of these Mn atoms adsorbed *OCHO and E_{ads}(*OCHO) and ΔG_{PDS}(HCOOH). The adsorption of the most critical intermediate *OCHO on the Mn atoms was significantly enhanced, then reducing the U_L values and improving the catalytic performance.

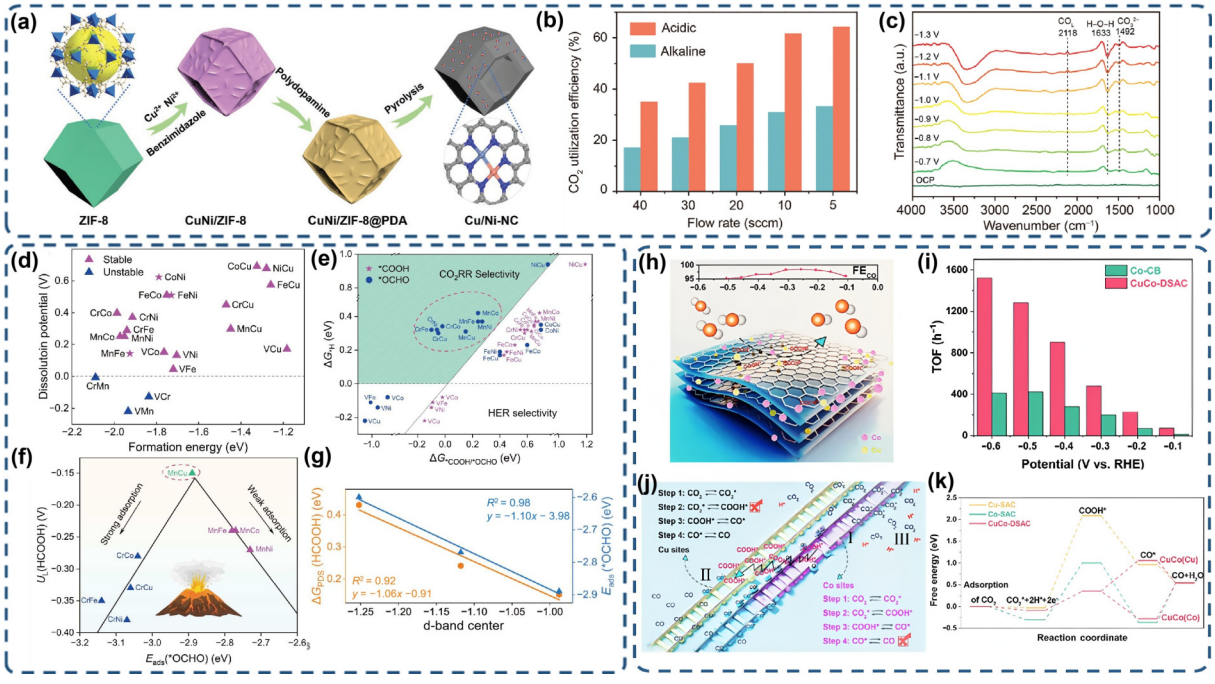

Figure 15 (a) Schematic Illustration for construction of Cu/Ni-NC. (b) Comparation of acid medium and alkaline medium for CO_2 utilization efficiency with different CO_2 flow rates. (c) *In situ* ATR-SEIRAS measurements over Cu/Ni-NC in acidic medium. Reproduced with permission from Ref. [72], © Wiley-VCH GmbH 2023. (d) Formation energy and dissolution potential of M_1/M_2-NC ADCs. (e) Comparison of ΔG_{*H} with ΔG_{*COOH} or ΔG_{*OCHO}. (f) Volcano plot of the adsorption energy of *OCHO on the eight M_1/M_2-NC versus the limiting potential for the generation of HCOOH. (g) The linear relationship between the *d*-band centers of Mn atoms in Mn-NC, Mn/Co-NC and Mn/Cu-NC adsorbed *OCHO and both the ΔG_{PDS} for HCOOH and the E_{ads} of the *OCHO intermediate. Reproduced with permission from Ref. [229], © Science China Press 2025. (h) The process of catalyst CuCo-DSAC promoting the generation of CO from CO_2. (i) Turnover frequency of Co-CB, and CuCo-DSAC. (j) The following schematic illustrates the CO_2 reduction pathways for the copper (yellow rails) and cobalt sites (purple rails). (k) Free energy profiles at $U = 0$ V of CO_2RR. Reproduced with permission from Ref. [230], © Wiley-VCH GmbH 2025.

Professor Dingsheng Wang and his collaborators synthesized a Cu-Co dual single-atom catalyst (CuCo-DSAC) anchored on carbon black by a straightforward pyrolysis strategy can effectively inhibit the competing HER and solve intermediate over-stabilization in electrocatalytic CO_2RR [230]. CuCo-DSAC catalyst synergistically enhance CO_2 electroreduction to CO by tuning electronic structure and facilitating COOH* spillover and achieve 500 mA·cm^{-2} at −0.66 V with 98.5% CO selectivity in a flow cell with 1.0 M KOH (Fig. 15(h)). The TOF 1522 h^{-1} at −0.6 V of CO in CuCo-DSAC catalyst surpassed Co–CB by 3.5-fold (Fig. 15(i)), and preliminary findings from durability tests indicate the FE of CO (less than 6%) and current density (about 0.85 mA·h^{-1}) have a relatively small loss. *In situ* SERS and *In situ* ATR-SEIRAS analyses provide the dynamic transition of key intermediate in CuCo-DSAC catalyst during electrocatalytic CO_2RR. The complementary synergistic interactions of Cu and Co active sites were established by the *in situ* spectroscopic data (Fig. 15(j)). Specifically, Co activates CO_2 and stabilizes *COOH intermediates, while Cu prevents the accumulation of the intermediate by promoting spillover and CO desorption. Free energy profile in Fig. 15(k) by DFT calculations reveals distinct reaction pathways at Cu and Co sites at U = 0 V of CO_2RR. Combined with the analysis of DOS and partial DOS (PDOS), the charge of redistribution between Cu and Co and the optimize of their respective roles in CO_2 activation and intermediate management were confirmed. The work offers novel insights into the development of electrocatalysts for intricate reaction systems, demonstrating the potential of tailored dual-site structures in complex electrocatalytic processes.

5.3 OER

With the increasing demand for clean energy sources such as hydrogen, electrochemical water splitting has garnered significant attention in the field of energy storage and conversion. The OER serves as the anodic half-reaction in this process. OER involves multiple electron transfer steps and exhibits inherently sluggish kinetics, which significantly limits the efficiency of water splitting and hydrogen production [112, 248–253]. As a four-electron transfer process, it requires a minimum thermodynamic potential of 1.23 V to drive the reaction [254]. In general, the overpotential beyond 1.23V at 10 mA·cm^{-2} is used to evaluate the OER performance (η_{10}). However, some Ni- and Co-based electrocatalysts exhibit strong redox peaks within a potential range slightly above 1.23 V [254]. To eliminate this error, the overpotential at a higher specific current density, such as 100 mA·cm^{-2}, is also selected for comparison. Traditionally, OER catalytic activity has been reliant on precious metal oxides catalysts (RuO_2 and IrO_2), which have drawbacks of high cost and poor durability [252, 254, 255]. Currently, ADCs have emerged as an appealing alternative to precious metal catalysts in OER. In this section, we will summarize the application of ADCs in OER. The reported ADCs for OER with the corresponding synthetic method and active sites, electrolyte, η and tafel slope are summarized in Table 4. Several representative examples, such as Fe-Ni, Co-Fe, and Fe-Fe dual-atom catalysts, are selected to elucidate the structural and electronic factors contributing to the superior OER performance of carbon-based ADCs [57, 90, 256].

Gao and colleagues synthesized a series of isostructural molecular complex catalysts by coordinating aromatic carboxylate ligands with Fe and Ni sites on conductive carbon substrates [256]. Strong π–π stacking interactions among the complexes enhance their stability and effectively modulate the coordination environment of Fe and Ni centers. Bader charge analysis confirms that π–π stacking significantly alters the electronic structure of FeNi atomic pairs in FeNi-L_3 (Fig. 16(a)). Electrochemical tests, including LSV curves, Tafel slopes, and TOF values, demonstrate that FeNi-L_3 exhibits superior OER kinetics compared to FeNi-L_1, FeNi-L_2, and FeNi-L_4. Its enhanced catalytic performance is attributed to the FeNi-organic coordination structures regulated by π–π stacking, which also contribute to high OER mass activity and TOF. Operando XAS shows that Fe and Ni K-edges gradually shift to higher energies as the anodic potential increases from OCP to 1.5 V. Notably, oscillations appear when the potential exceeds 1.5 V (Fig. 16(b)), likely due to OH nucleophilic attack induced by active Fe sites. First-principles calculations reveal that the Fe site carries a higher positive charge than Ni (Fig. 16(c)). Gibbs free energy analysis further shows that π–π stacking significantly influences the

Table 4 Summary of the OER performance of carbon-based ADCs catalysts along with the corresponding synthesis method, active sites, electrolyte, η and tafel slope

Catalyst	Synthetic method	Active site	Electrolyte	η (mV)	Tafel slope (mV·dec^{-1})	Ref.
VB-FeNiP	Hydrothermal borohydride immersion and phosphating process	Fe-Ni dual sites	1M KOH	175(η_{100})	57.64	[257]
Ru/Co-N-C	Self-assembly and nitridation processes	RuN_4 sites	0.5 M H_2SO_4 1 M KOH	232(η_{10}) 247(η_{10})	23.3 27.8	[258]
S/N-CMF@$Fe_xCo_yNi_{1-x-y}$-MOF	Cation exchange strategy	$Fe_xCo_yNi_{1-x-y}$	1M KOH	296(η_{10})	53.5	[259]
Co/Fe-SNC	Microemulsion-co-precipitation reaction and pyrolysis method	Co sites	1M KOH	240(η_{10})	47.92	[90]
NiAl LDH	Hydrothermal process	NiO_6 octahedron	1M KOH	330(η_{10})	83	[260]
DA-FC-NG	Freeze-drying and annealing strategy	Fe-O-Co bridge	1M KOH	268(η_{10})	50	[261]
FeNi-L_3	Self-assembly strategy	Fe-Ni dual sites	1M KOH	253(η_{100})	41	[256]
Ir-$SrMnO_3$	Cation exchange method	Ir-Mn dual sites	0.5 M H_2SO_4	207(η_{10})	81	[262]
Fe-$NiCo_2S_4/Ni_3S_2$	Hydrothermal process	Fe-CoNiOOH	1M KOH	210(η_{100})	48.86	[263]
Ni-BDC/NM88B(Fe)	Hydrothermal process	Ni-O-Fe bonds	1M KOH	232(η_{100})	33.5	[264]
NiFe-LS	Hydrothermal process	Fe and Ni sites	1M KOH	220(η_{100})	35.93	[265]
A-$Fe_2S_1N_5$/SNC	High-temperature pyrolysis method	Fe-Fe dual sites	1M KOH	193(η_{10})	61	[57]

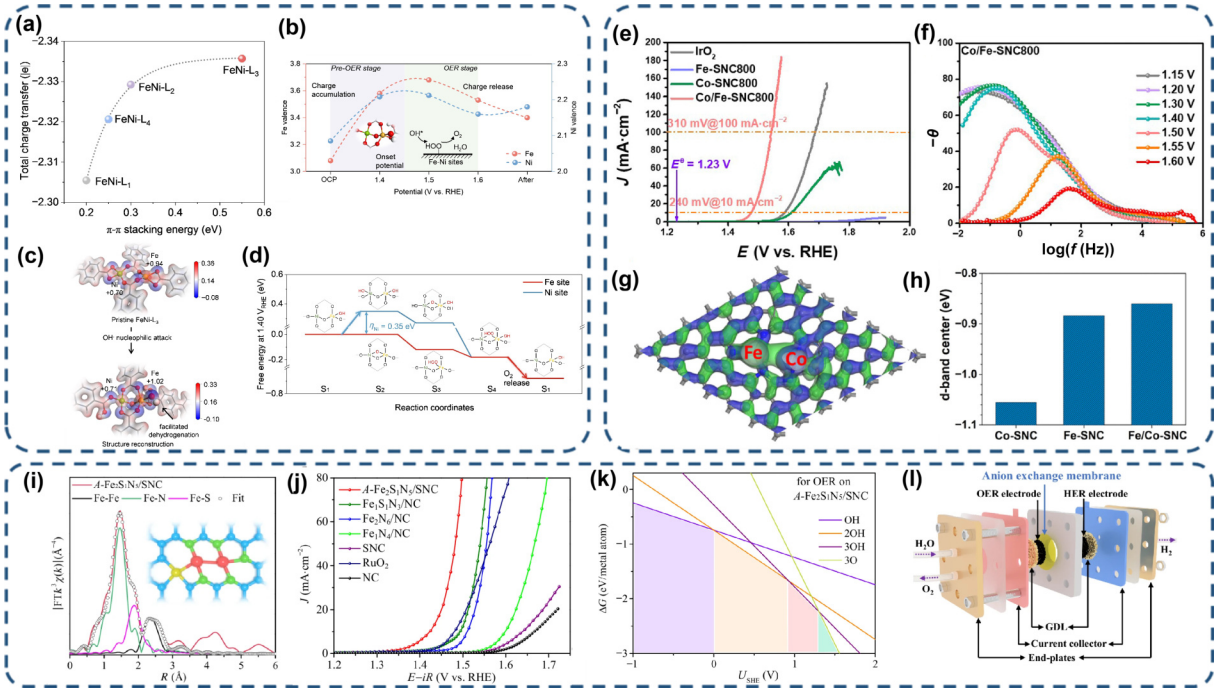

Figure 16 (a) Relationship between calculated π–π stacking energy and total charge transfer. (b) The valence states of Fe and Ni species at different potentials of FeNi-L_3. (c) The electrostatic potential of FeNi-L_3 in initial stage and pre-OER stage. 3). (d) Free energy evolution of FeNi-L_3 with Fe or Ni site as active center for OER process under an electrode potential of 1.40 V. Reproduced with permission from Ref. [256], © Wiley-VCH GmbH 2024. (e) The LSV curves of Fe-SNC800, Co-SNC800, Co/Fe-SNC800 and reference catalysts at 1600 rpm. (f) Bode plots of Co/FeSNC800 under various applied potentials in the analysis of OER catalytic mechanism. (g) 3D contour plot of bonding and anti-bonding orbitals near the Fermi level in Co/Fe-SNC. (h) Comparison of d-band center for Co/Fe-SNC, Co-SNC and Fe-SNC. Reproduced with permission from Ref. [90], © The Royal Society of Chemistry 2023. (i) WT-EXAFS plots of *A*-$Fe_2S_1N_5$/SNC, Fe foil, FePc, and FeS_2. Inset: atomic configuration model of *A*-$Fe_2S_1N_5$/SNC. (j) LSV curves of the prepared catalysts. (k) Free energy of a series of coverage fraction surfaces sampled for the *A*-$Fe_2S_1N_5$/SNC catalysts. (l) Schematic illustration of the assembled AEM electrolyzer (GDL, gas diffusion layer). Reproduced with permission from Ref. [57], © Zhang, L. L. et al. 2024.

Fe-OH* dehydrogenation process. Thermodynamic calculations indicate that Fe sites have a lower reaction Gibbs free energy than Ni sites, suggesting more favorable oxygen evolution on Fe (Fig. 16(d)). Combined theoretical and experimental results suggest that successive OH attacks and dehydrogenation on highly oxidized Fe sites lead to dynamic Fe-O-Ni species reconstruction at low potentials during OER. The reduced valence states of these species are linked to rapid oxygen generation.

Chen and colleagues synthesized a well-dispersed $Fe(OH)_x$/$Co(OH)_x$@SNC precursor via a microemulsion-co-precipitation method. After pyrolysis at 800 °C and subsequent acid leaching to remove metal or metal oxide nanoparticles, a catalyst with fully exposed bimetallic sites, Co/Fe-SNC800, was obtained [90]. XANES and EXAFS analyses revealed the local electronic structure, confirming a ring-like coordination model where Fe and Co are coordinated with N and S, respectively, and indirectly linked by N-C-N bridges. The catalyst exhibited excellent OER performance, with an onset potential of 1.42 V (vs. RHE) at 0.1 mA·cm^{-2}, surpassing that of single-atom catalysts Fe-SNC800 and Co-SNC800. At mA·cm^{-2}, its overpotential was as low as 240 mV, outperforming commercial IrO_2 (Fig. 16(e)). Bode plots under various potentials (Fig. 16(f)) indicate that both Fe and Co sites participate in the catalytic process. A plausible OER mechanism on Co/Fe-SNC800 is proposed: (Fe_{site} + 3OH − 3e$^-$ = $Fe_{site}OOH$ + H_2O; $Fe_{site}OOH$ + Co_{site} = $Co_{site}OOH$ + Fe_{site} and $Co_{site}OOH$ + OH − e$^-$ = Co_{site} + O_2 + H_2O). Strong orbital coupling between Co and Fe single-atom sites near the Fermi level was observed (Fig. 16(g)). DFT calculations further confirmed that the introduction of non-metallic S and N plays a crucial role in enhancing OER performance. The catalyst exhibits the highest d-band center at 0.86 eV (Fig. 16(h)), indicating superior electrical activity. The coordination of Co with S/N, Fe with N, and the unique asymmetric coordination environment not only facilitate efficient electron transfer but also stabilize the structure, thereby ensuring high OER activity and durability.

Zhang and co-workers introduced numerous defects and a high content of non-metal heteroatoms into *A*-$Fe_2S_1N_5$/SNC through a continuous two-step pyrolysis and carbonization process [57]. The specific atomic structure of *A*-$Fe_2S_1N_5$/SNC catalysts contain direct Fe–Fe bonding, one Fe bonded with one S atom and two N atoms, and the other Fe connected by three N atoms (Fig. 16(i)). Asymmetric Fe-Fe dual-metal sites serve as the active sites for the OER, resulting in a low overpotential of 193 mV at 10 mA·cm^{-2}, which exceeds that of commercial ruthenium dioxide catalysts (Fig. 16(j)). DFT calculations revealed that unconventional chemical intermediates, such as 2*OH, *O+OH, 2O, or *O_2, were more stable than classical ones, including *O and *OOH species (Fig. 16(k)). During the OER process, *A*-$Fe_2S_1N_5$/SNC demonstrated extraordinary stability, retaining over 97% of its activity for more than 2000 h. An alkaline AEMWE (anion exchange membrane water electrolyzer) was further assembled to expand the electrochemical applications of *A*-$Fe_2S_1N_5$/SNC catalysts (Fig. 16(l)). As expected, the *A*-$Fe_2S_1N_5$/SNC-based battery displayed better performance than Pt/C+RuO_2 battery, and it has certain potential in commercial applications.

5.4 HER

The HER plays a critical role in the global energy transition. As a

key process for sustainable hydrogen production, it is considered a promising solution to the energy crisis and an essential component of environmental protection [266, 267]. In HER, the crucial reaction steps follow different mechanisms depending on the medium.[229, 268–271] In alkaline media, it adheres to the Volme–Heyrovsky mechanism: ($H_2O + e^- + * \rightarrow H^* + OH^-$; $H_2O + H^* + e^- \rightarrow H_2 + OH^-$). In acidic media, it follows either the Volmer–Tafel mechanism: ($H^+ + e^- + * \rightarrow H^*$; $2H^* \rightarrow H_2$) or the Volmer–Heyrovsky mechanism: ($H^+ + e^- + * \rightarrow H^*$; $H^* + H^+ + e^- \rightarrow H_2$) [272, 273]. Platinum (Pt), as the most widely used catalyst in HER, also has its own drawbacks, such as low abundance and high cost, which limit its wide application [274, 275]. Therefore, developing efficient and low-cost alternative catalysts is challenging. ADCs have recently emerged as a novel class of catalysts in the field of electrocatalysis. ADCs show great potential in HER, which can significantly improve catalytic performance through synergistic effects and tunability. These catalysts are expected to become substitutes for platinum-based catalysts. The overpotential at a current density of 10 mA·cm^{-2} (η_{10}) in HER is a key parameter to evaluate the HER performance, and a lower η_{10} indicates a more efficient catalyst. The synergistic effect between the two metal atoms in ADCs is a significant advantage. This synergy can lower the activation energy of the rate-determining step in HER. By working together, the two metal atoms can break the reaction pathway into more favorable steps, each with a lower energy barrier. The reported ADCs for HER are summarized in Table 5, where we have selected five embodiments to illustrate the reasons for the excellent HER performance of ADCs.

Liu and coworkers reported a strategy of *in situ* confined pyrolysis to synthesize hetero-diatomic Ir and Ni metal sites anchored on nitrogen doped carbon support (IrNi-N-C) [276]. The optimized IrNi-N-C structural model can be determined by the Ni K-edge XANES simulation parameters from XAFS analysis (Fig. 17(a)). Notably, the chronopotentiometry curves of IrNi-N-C at different cathodic current densities for each 20 h was shown in Fig. 17(b). The result demonstrated a negligible increase of the applied potential at the specified current density during each 20 h period and indicated the excellent long-term stability of the IrNi-N-C catalyst. The calculated adsorption free energy profiles of HER on the active sites of Ni-N-C, Ir-N-C, Ni_ IrNi-N-C, and Ir_IrNi-N-C in an acidic environment through DFT calculations was shown in Fig. 17(c). For IrNi-N-C, both atomic Ir(Ir_IrNi-N-C) and Ni(Ni_IrNi-N-C) sites exhibit smaller ΔG_{H^*} values of 0.22 and 1.15 eV, respectively, compared to those of Ir-N-C and Ni-N-C. Notably, Ir_IrNi-N-C has the smallest ΔG_{H^*}, signifying a moderate H* adsorption, which makes it the major active site for enhanced HER catalytic activity. According to the schematic DOS diagram after hydrogen adsorption on Ir-N-C and IrNi-N-C catalysts, lowering the energy position of antibonding states of IrNi-N-C can generate the higher occupancy (Fig. 17(d)). The intrinsic communication and electronic coupling in hetero-diatomic IrNi-N-C catalyst is important for the production of superior HER catalytic activity.

Li and coworkers used multi-metal single-crystal ordered macroporous MOFs as precursors to synthesize CoNi SAs@NPs-NC, and employed DFT calculations to explore its HER activity mechanism [277]. In the synthesis of multi-metal SOM MOFs, a small amount of acid is introduced to inhibit crystallization, then, ammonia/methanol induces crystallization of SOM ZnCoNi-ZIFs. Finally, high-temperature carbonization then converts it to CoNi SAs@NPs-NC (Fig. 17(e)). The HER polarization curves in 1 M KOH show CoNi SAs@NPs-NC (η_{10} = 90 mV) outperforms CoNi SAs-NC (η_{10} = 755 mV), showing the NP-SA synergy (Fig. 17(f)). In the DFT calculations, single-layer graphene doped with Co-N_4 and Ni-N_4 SAs was utilized as the computational model of CoNi SAs-NC (Fig. 17(g)). According to the Gibbs free energy (ΔG_H) evaluation of the intermediate hydrogen adsorption, it can obtain that hydrogen atoms preferentially adsorb atop Co SAs across all models. CoNi SAs@NPs-NC (ΔG_{H^*} = 0.086 eV) is closer to the ideal 0 eV than CoNi SAs-NC (0.357 eV), indicating enhanced HER activity (Fig. 17(h)). Co SAs@NPs-NC (ΔG_{H^*} = 0.075 eV) shows a favorable hydrogen adsorption energy pathway. In addition, the synergistic interaction at the NiCo-SAD atomic interface synthesized by Kim and colleagues enables fast water dissociation and optimal proton adsorption, thereby enhancing HER kinetics in both acidic and alkaline environments [278].

Zhao and coworkers reported a surface-modification strategy to construct a dual-atom electrocatalyst with an MXene substrate for efficient HER and OER [279]. Figure 17(i) shows the synthesis process. L-tryptophan was attached to $Ti_3C_2T_x$ MXene to form Try-$Ti_3C_2T_x$, and then $CoCl_2$ and $NiCl_2$ were added via a freezing-UV method to fabricate CoNi-$Ti_3C_2T_x$. Surface modification enhanced metal atom adsorption, achieving a 5.6 wt.% metal loading. Figure 17(j) presents the OER LSV curves of CoNi-$Ti_3C_2T_x$, Ni-

Table 5 Summary of the HER performance of carbon-based ADCs catalysts along with the corresponding synthesis method, active site, electrolyte, η_{10} and tafel slope

Catalysts	Synthetic method	Active site	η_{10} (mV)	Tafel slope (mV·dec^{-1})	Ref.
W_1Mo_1-NG	Controllable self-assembly and nitridation processes	W-O-Mo-O-C	24	30	[284]
FR-NCS	Top-down strategy	Rh-Fe-N moiety	36	26	[285]
CNs@CoPt	*In situ* synthesis and pyrolysis treatment	CoPt alloy structure	4.2	85.4	[286]
IrNi-N-C	*In situ* confined pyrolysis	Ni and Ir sites	28	38	[276]
M-NM/g-CN, HDACs	Machine learning method	Diatomic center	—	—	[287]
FeMo@CoNi-OH/Ni_3S_2	Hydrothermal method and epitaxial Growth	Fe and Mo sites	89	73.5	[288]
Ni_3N-CeO_2/NF	Hydrothermal and nitriding process	Ni sites and NiOOH	30	42.79	[289]
RuBi SAA/Bi@OG	One-step pyrolysis method	Ru atom	17.5	29.2	[9]
CoNi SAs@NPs-NC	Carbonization of metal-organic frameworks	CoNi NPs	64	37	[277]
CoNi-$Ti_3C_2T_x$	Surface modification strategy	Ni and Co atoms	31	33	[279]
NiCo-SAD-NC	Facile two-step synthesis strategy	Ni-Co atomic interface	54.7	55	[278]
Pt-Ru dimers	Atomic layer deposited method	Pt-Ru dimers	50	28.9	[290]

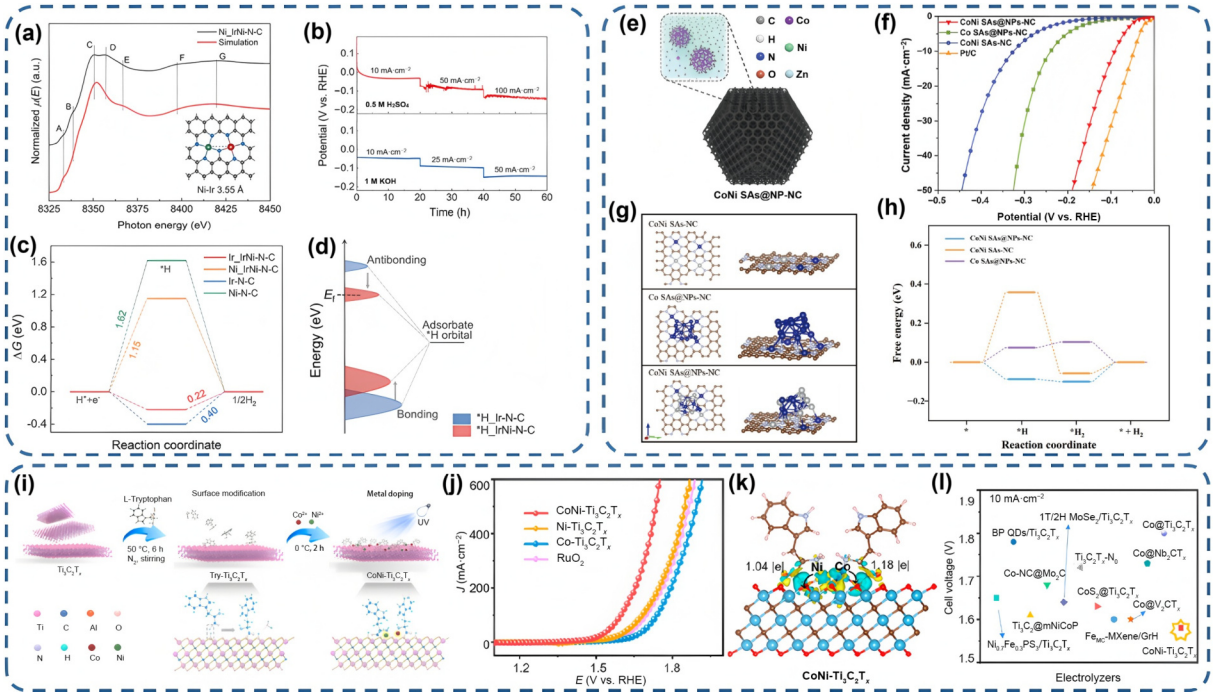

Figure 17 (a) Comparison between the Ni K edge XANES experimental spectrum of IrNi-N-C and theoretical spectrum calculated on the basis of the optimized Ir-N-Ni-N_6-C motif as shown in inset. (b) Chronopotentiometry curves of IrNi-N-C at different cathodic current densities for each 20 h. (c) Calculated adsorption free energy profiles of HER on the active sites of Ni-N-C, Ir-N-C, Ni_IrNi-N-C and Ir_IrNi-N-C in acidic electrolytes. (d) Schematic DOS diagram illustrating the bonding and antibonding states as a result of the interaction between Ir and adsorbed H intermediate for Ir-N-C and IrNi-N-C. Reproduced with permission from Ref. [276], © Elsevier Ltd. 2022, all rights reserved. (e) The prepared ZnCoNi-ZIFs by utilizing the deprotonation to control the crystallization process between metal ions and ligands. (f) HER polarization curves of CoNi SAs@NPs-NC, Co SAs@NPs-NC, CoNi SAs-NC and Pt/C in 1 M KOH. (g) Optimized structures of CoNi SAs-NC, Co SAs@NPs-NC and CoNi SAs@NPs-NC. (h) Free energies of the HER process in 0.5 M H_2SO_4. Reproduced with permission from Ref. [277], © Science China Press 2024. (i) Schematic illustration of the dual-atom CoNi$Ti_3C_2T_x$ composites by $Ti_3C_2T_x$ MXene as a substrate. (j) OER LSV curves of Co-Ni-$Ti_3C_2T_x$, Ni-$Ti_3C_2T_x$, Co-$Ti_3C_2T_x$, and RuO_2 electrodes at 5 mV·s^{-1}. (k) The charge density difference and the calculated Bader charges of active sites for CoNi$Ti_3C_2T_x$ electrocatalysts. (l) Cell voltage comparison between the Co-Ni-$Ti_3C_2T_x$(+,–) electrodes and previously reported MXene-based electrolyzers at a current density of 10 mA·cm^{-2}. Reproduced with permission from Ref. [279], © American Chemical Society 2024.

$Ti_3C_2T_x$, Co-$Ti_3C_2T_x$, and commercial RuO_2 electrodes. Co-Ni-$Ti_3C_2T_x$ electrode displayed an OER overpotential of 241 mV at 10 mA·cm^{-2}, which was smaller than those of other catalysts. Co and Ni centers in Co-Ni-$Ti_3C_2T_x$ show lower electron density in the calculation of charge density difference plots, which demonstrated that electrons are transferred from Co/Ni atoms to Try-$Ti_3C_2T_x$ (Fig. 17(k)). The synergetic interaction between Co and Ni atoms results in a higher degree of an electron transfer, which is beneficial for lowering the energy barrier for both OER and HER processes. Figure 17(l) compares the cell voltage of the Co-Ni-$Ti_3C_2T_x$ electrodes with previously reported MXene-based electrolyzers at 10 mA·cm^{-2}. Co-Ni-$Ti_3C_2T_x$ required a small voltage of only 1.58 V to reach this current density. The Co-Ni-$Ti_3C_2T_x$ based electrolyzer also exhibited high energy efficiency and good durability. Overall, the surface-modified dual-atom CoNi electrocatalyst on $Ti_3C_2T_x$ has excellent HER and OER performance, guiding the development of high-performance electrocatalysts.

Atomically dispersed asymmetric catalysts have broad applications. Beyond electrocatalysis, their uses in other reactions are various. Atomic-level dispersed RuM (M = Ni, Co, Cu, and Fe)-MXene catalysts construct a high-performance catalytic platform for hydrogen oxidation reaction (HOR) and phenylacetylene hydrogenation and achieve the adaptation of catalyst active centers in the two reaction systems [280]. Among them, the RuNi atomically dispersed clusters-Ti_3C_2 with multisites showed the high of activation and conversion of hydrogen. DFT studies indicate that the RuNi clusters and Ti_3C_2 MXene are dependable platforms for the activation and conversion of H_2 in HOR. Atomically dispersed asymmetric bimetallic-ternary-structured catalysts ($Ru_{1+n}M_1$-TiO_2, M = Co, Cu, Fe, and Ni) via a simple impregnation reduction method can facilitate the efficient generation of negative hydrogen in nitrobenzene hydrogenation transfer process under moderate conditions [281]. The $Ru_{1+n}Co_1$-TiO_2 catalysts exhibited highest activity for H_2 production form ammonia borane hydrolysis and achieved high yields in converting nitrobenzene to anilines using ammonia borane. The energy barrier calculations in DFT studies indicated that atomically dispersed Co optimized the structure of the active sites in $Ru_{1+n}Co_1$-TiO_2 catalysts, which reduced the activation energy to its minimum value (0.5 eV), thus effectively improving the reaction efficiency. The investigation demonstrated bimetallic-ternary-structured catalysts provided an effective direction for hydrogen generation process in chemical hydrogen storage materials. The dual-metal asymmetric atomic pairs DAP-(M,Rh)/CN (M = V, Cr, Mn, Fe, Co, Ni, and Cu) supported on nitrogen-doped carbon demonstrated the cooperative effects in formic acid oxidation reaction [282]. Formic acid oxidized on Rh-M pairs through the formate route with the subsidiary M sites binding the HCOO species in the most suitable adsorption strength and Rh atom accepting the H atoms by DFT and *in situ* FTIR analysis. The two spontaneous elementary steps in dual atomic active centers accelerated the formic acid oxidation reaction rates. Atomically Precise Cu-Pd sites appeared efficient methanol

electrooxidation reaction with a CO-free pathway by adjacent-ligand tuning [283]. Ligand modulation leads to charge transfer and the rapid migration of OH greatly improves the selectivity of non-CO pathways by the analysis of structural characterization and *in situ* experiment.

6 Summary and prospect

6.1 Summary

ADCs, featuring adjacent homonuclear or heteronuclear metal active atoms anchored to stable supports, represent a promising frontier in catalysis. This robust coordination structure prevents metal atom migration or aggregation, ensuring enhanced catalyst longevity. Crucially, the spatial misalignment of dual active sites permits the simultaneous binding of distinct reactants or intermediates, inducing cooperative effects that lower reaction energy barriers and accelerate overall kinetics. Both heteronuclear and homonuclear diatomic sites leverage their unique coordination environments to precisely modulate intermediate adsorption strength through electron transfer and orbital hybridization. The resulting synergistic interaction between bimetallic centers fundamentally restructures catalytic pathways, significantly boosting electrocatalytic efficiency.

This review systematically categorizes ADCs configurations (homonuclear vs. heteronuclear) and associated synthesis methodologies (Fig. 18). We comprehensively evaluate: (i) established synthesis strategies, (ii) essential and complementary characterization techniques, and (iii) performance across four major electrocatalytic applications: ORR, CO_2RR, OER, and HER. Notably, the integration of AI is advancing the rational and accelerated design of high-performance ADCs. Within our primary focus on electrocatalysis, mechanistic insights are derived by integrating analysis of key electrochemical parameters—including LSV, EIS, FE, and $E_{1/2}$—with DFT calculations. This multidisciplinary approach elucidates reaction mechanisms through detailed examination of intermediate adsorption configurations, orbital coupling, and charge transfer dynamics. Despite their exceptional synergistic performance, ADCs face significant challenges in scalable synthesis and practical implementation for energy technologies. Addressing these limitations is critical for realizing the full potential of ADCs-based systems.

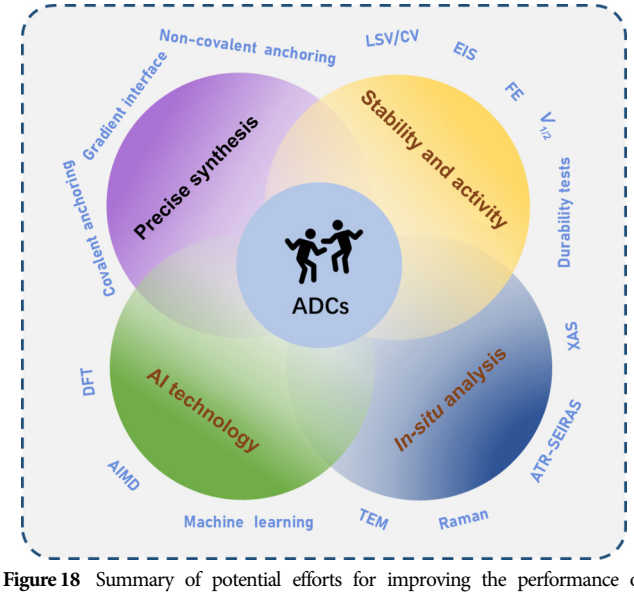

Figure 18 Summary of potential efforts for improving the performance of ADCs.

6.2 Prospect

(1) The precise synthesis of ADCs remains a significant challenge, necessitating continuous advancements in synthesis methods. In the synthesis process, attention should be paid to the dispersion of the dual active site, and the isolated anchoring is very important. For heteronuclear ADCs, it is also necessary to control the content ratio of the dual active metal site and the regulation of the specific coordination configuration microenvironment, which directly affect the activity and selectivity of synthetic ADCs in electrocatalysis. The existing synthesis methods of ADCs have certain limitations and complexity, the selection of metal precursors and supports, and the development of low temperature synthesis strategies to avoid the destruction of diatomic structures at high temperatures are all problems that need to be considered. It is very important to develop a more universal and economical method for accurate synthesis of ADCs to promote the application of ADCs in electrocatalysis. In the future, new strategies for the design of new support and interfaces in ADCs can be further studied from the following aspects: dynamic interface regulation strategies for adaptive coordination environments, covalent anchoring strategies through nitrogen or/and non-metallic fixed diatoms, non-covalent anchoring strategies by π–π stacking or electrostatic adsorption of precursors, and gradient interface design strategies for multi-stage mass transfer optimization. Such as, introducing heteroatoms into ADCs could affect the coordination configuration and charge density of the metal centers, thereby creating better catalytic performance [291]. Thus, there is a longing demand to develop general preparation principles to expand the application of ADCs to practical industrial implementations, especially for the degradation of various organic substances in environmental pollutants.

(2) The electrochemical stability (activity/selectivity) and thermodynamic stability (stability/durability) of ADCs are interrelated yet contradictory. In practical applications, a balance must be struck among the importance two aspects to achieve the maximum application value. The activity and selectivity of ADCs usually depend on the asymmetric coordination environment or electronic imbalance at the bimetallic sites. However, such structures are prone to atomic migration or aggregation and electron transfer under reaction conditions (such as high temperature, strong acids/alkalis), which leads to inactivation and results in poor stability of ADCs. Compared with the significant breakthroughs of activity and selectivity, the stability and durability of ADCs have not received sufficient attention [24]. Stability refers to the ability to resist changes in a short period of time, while durability reflects the performance degradation over a long-term cycle. Adopting specific strategies based on rational design can address these stability and durability challenges through the strategy of "structure limited domain, electron regulation and mass transfer optimization", such as the design of new stable support and interface between the active site and the supporting atoms, the design of the stability of active sites by physical or chemical methods, the design of porous electrodes for enhancing mass transfer efficiency, the design of reasonable surface modification strategies. The stability and durability are interrelated yet distinct from each other, which of them need to be analyzed in depth for green catalysis and conversion. The catalytic pathway can be

optimally enhanced through the collaborative optimization of electronic tuning and spatial confinement, thereby strengthening the positive correlation between the thermodynamic and electrochemical stability of ADCs.

(3) The dynamic interaction behavior of the asymmetric diatomic active sites in ADCs is a key determinant of catalytic performance. Tracking and identifying the dynamic changes of bimetal active sites during catalysis by accurate *in situ* and operando analysis method is an effective means to understand the reaction mechanism and optimize the reaction process. The existing *in situ* and operando characterization techniques include TEM, Raman, ATR-SEIRAS, XAS and the steady-state isotopic transient kinetic analysis (SSITKA), which provide direct experimental basis for the design of DACs at different levels of real-time structure and morphology. The rational combination of different real-time characterization techniques can enable shed light on a systematic understanding of the dynamic behavior of active sites in ADCs [24]. However, for these *in situ* and operando characterization methods, local characterization results are often difficult to represent the overall uniformity of ADCs, which requires a combination of large-scale statistical analysis and theoretical simulation. In the future, it is necessary to develop the combined technology of *in situ* and operando characterization techniques with higher spatial and temporal resolution to meet the needs of more real-time tracking analysis of precise atomic-level control over these dynamic changes in ADCs systems.

(4) The artificial intelligence (AI) technology that integrates quantum computing and machine learning is applied to the study of ADCs, which can used to facilitate the prediction and screening of highly active metal sites. Through theoretical calculation methods such as DFT and ab initio molecular dynamics (AIMD), the charge distribution and orbital hybridization of bimetallic active sites in ADCs can be accurately analyzed, and the synergistic effect of charge transfer and orbital coupling between the two active sites in electrocatalysis can be revealed. The theoretical calculation optimizes the reaction path by simulating the key intermediates and transition states in electrocatalysis. Machine learning generally predicts highly active and selective ADCs through high-throughput screening, and then establishes the quantitative relationship between the geometric structure, electronic characteristics and electrocatalytic performance of bimetallic active sites in ADCs through structure-activity relationship modeling. However, in practical application, the theoretical calculation is faced with problems such as the difficulty of predicting complex systems, the difficulty of accurately describing the quantitative prediction of special structures, the difference between the dynamic simulation of catalysis and the real environment, and the lack of coordination between theory and experiment. In the future, it is necessary to combine the electrocatalytic process of ADCs with machine learning to predict the dynamic evolutionary path of bimetallic sites. It is also necessary to optimize the combination of theoretical and experimental studies to promote rational design of ADCs. It is necessary to reverse design support materials with machine learning, and develop dynamic interface engineering to realize the leap from "accurate synthesis" to "intelligent response".

Data availability

Not applicable.

Acknowledgements

This work was Sponsored by Natural Science Foundation of Henan (No. 252300421175), University Natural Science Research Project of Anhui Province (No. 2024AH040186), Application Project of Bengbu University (No. 2024YYX28QD), and the Financial Program of BJAST (No. 25CA002).

Declaration of competing interest

The authors declare that they have no known competing financial interests or personal relationships that could have appeared to influence the work reported in this paper.

Author contribution statement

Y. G.: Data curation, project administration, validation, writing manuscript, funding acquisition, review design. J. L. G.: Project administration, writing manuscript. T. T. C.: Project administration, writing manuscript. J. J. J.: Project administration, writing manuscript. Y. M. H.: Project administration, writing manuscript. H. S. S.: Project administration, validation, writing manuscript, review design. X. W. L.: Project administration, validation, writing manuscript, funding acquisition, review design. All the authors have approved the final manuscript.

Use of AI statement

None.

References

[1] Wan, J.; Song, Y. X.; Chen, W. P.; Guo, H. J.; Shi, Y.; Guo, Y. J.; Shi, J. L.; Guo, Y. G.; Jia, F. F.; Wang, F. Y. et al. Micromechanism in all-solid-state alloy-metal batteries: Regulating homogeneous lithium precipitation and flexible solid electrolyte interphase evolution. *J. Am. Chem. Soc.* **2020**, *143*, 839–848.

[2] Shang, H. S.; Liu, D. Atomic design of carbon-based dual-metal site catalysts for energy applications. *Nano Res.* **2023**, *16*, 6477–6506.

[3] Song, Z. X.; Li, J. J.; Zhang, Q. L.; Li, Y. L.; Ren, X. Z.; Zhang, L.; Sun, X. L. Progress and perspective of single-atom catalysts for membrane electrode assembly of fuel cells. *Carbon Energy* **2023**, *5*, e342.

[4] Fang, W. S.; Guo, W.; Lu, R. H.; Yan, Y.; Liu, X. K.; Wu, D.; Li, F. M.; Zhou, Y. S.; He, C. H.; Xia, C. F. et al. Durable CO_2 conversion in the proton-exchange membrane system. *Nature* **2024**, *626*, 86–91.

[5] Wang, X. C.; Zhang, N.; Shang, H. S.; Duan, H. J.; Sun, Z. Y.; Zhang, L. L.; Lei, Y. T.; Luo, X.; Zhang, L.; Zhang, B. et al. Precisely designing asymmetrical selenium-based dual-atom sites for efficient oxygen reduction. *Nat. Commun.* **2025**, *16*, 470.

[6] Zhao, X. L.; Wu, G.; Zheng, X. S.; Jiang, P.; Yi, J. D.; Zhou, H.; Gao, X. P.; Yu, Z. Q.; Wu, Y. E. A double atomic-tuned RuBi SAA/Bi@OG nanostructure with optimum charge redistribution for efficient hydrogen evolution. *Angew. Chem., Int. Ed.* **2023**, *62*, e202300879.

[7] Liu, K. Y.; Sun, Z. Y.; Peng, X. J.; Liu, X. D.; Zhang, X.; Zhou, B. R.; Yu, K. D.; Chen, Z. B.; Zhou, Q.; Zhang, F. et al. Tailoring asymmetric RuCu dual-atom electrocatalyst toward ammonia synthesis from nitrate. *Nat. Commun.* **2025**, *16*, 2167.

[8] Sha, Q. H.; Wang, S. Y.; Yan, L.; Feng, Y. S.; Zhang, Z.; Li, S. H.; Guo, X. L.; Li, T. S.; Li, H.; Zhuang, Z. B. et al. 10,000-h-stable intermittent alkaline seawater electrolysis. *Nature* **2025**, *639*, 360–367.

[9] Chen, L.; Yu, C.; Song, X. D.; Dong, J. T.; Mu, J. W.; Qiu, J. S.

Integrated electrochemical and chemical system for ampere-level production of terephthalic acid alternatives and hydrogen. *Nat. Commun.* **2024**, *15*, 8072.

[10] Liu, X. C.; Wu, G.; Han, X.; Wang, Y.; Wu, B.; Wang, G. M.; Mu, Y.; Hong, X. High-entropy metal interstitials activate TiO_2 for robust catalytic oxidation. *Adv. Mater.* **2025**, *37*, 2416749.

[11] Li, Q.; Wu, J. B.; Yang, C. Y.; Li, S. Y.; Long, C.; Zhuang, Z. C.; Li, Q.; Guo, Z. Q.; Huang, X. W.; Tang, Z. Y. et al. Ultralow coordination ccopper sites compartmentalized within ordered pores for highly efficient electrosynthesis of *n*-propanol from CO_2. *J. Am. Chem. Soc.* **2025**, *147*, 6688–6697.

[12] Wang, L. G.; Wu, J. B.; Wang, S. W.; Liu, H.; Wang, Y.; Wang, D. S. The reformation of catalyst: From a trial-and-error synthesis to rational design. *Nano Res.* **2024**, *17*, 3261–3301.

[13] Shen, J.; Chen, J.; Qian, Y. P.; Wang, X. Q.; Wang, D. S.; Pan, H. G.; Wang, Y. G. Atomic engineering of single-atom nanozymes for biomedical applications. *Adv. Mater.* **2024**, *36*, 2313406.

[14] Gan, T.; Wang, D. S. Atomically dispersed materials: Ideal catalysts in atomic era. *Nano Res.* **2024**, *17*, 18–38.

[15] Zhang, T. Y.; Wang, D. S.; Liu, J. F. Periodic single-metal site catalysts: Creating homogeneous and ordered atomic-precision structures. *Adv. Mater.* **2024**, *36*, 2408259.

[16] Lang, Z. Q.; Wang, X. X.; Jabeen, S.; Cheng, Y. Y.; Liu, N. Y.; Liu, Z. H.; Gan, T.; Zhuang, Z. C.; Li, H. T.; Wang, D. S. Destabilization of single-atom catalysts: Characterization, mechanisms, and regeneration strategies. *Adv. Mater.* **2025**, *37*, 2418942.

[17] Kong, K. J.; Zhang, H.; Han, A. L.; Li, F.; Wang, D. S. Atomically dispersed metal cocatalysts for solar energy conversion. *Energy Environ. Sci.* **2024**, *17*, 7649–7680.

[18] Hu, Y. M.; Chao, T. T.; Dou, Y. H.; Xiong, Y. L.; Liu, X. W.; Wang, D. S. Isolated metal centers activate small molecule electrooxidation: Mechanisms and applications. *Adv. Mater.* **2025**, *37*, 2418504.

[19] Li, M. H.; Li, J.; Zheng, X. Y.; Zhou, Y. Local environment regulation of transition metal dichalcogenide-based single-atom catalysts. *Rare Metals* **2024**, *43*, 4019–4037.

[20] Deng, Z. W.; Liu, Y.; Lin, J.; Chen, W. X. Rational design and energy catalytic application of high-loading single-atom catalysts. *Rare Metals* **2024**, *43*, 4844–4866.

[21] Zhao, Q.; Gan, R.; Ran, Y. L.; Ma, Q. L.; Chen, W. W.; Guo, Y. X.; Zhang, Y.; Wang, D. S. Single-atom catalysts: Controlled synthesis and dynamic mechanism in electrochemical oxygen evolution substitution reactions. *Rare Metals* **2024**, *43*, 4903–4920.

[22] Wang, L. G.; Wang, D. S.; Li, Y. D. Single-atom catalysis for carbon neutrality. *Carbon Energy* **2022**, *4*, 1021–1079.

[23] Ahmad, M.; Chen, J. H.; Liu, J. W.; Zhang, Y.; Song, Z. X.; Afzal, S.; Raza, W.; Zeb, L.; Mehmood, A.; Hussain, A. et al. Metal-organic framework-based single-atom electro-/photocatalysts: Synthesis, energy applications, and opportunities. *Carbon Energy* **2024**, *6*, e382.

[24] Liu, J. J.; Yang, J. R.; Dou, Y. H.; Liu, X. W.; Chen, S. H.; Wang, D. S. Deactivation mechanism and mitigation strategies of single-atom site electrocatalysts. *Adv. Mater.* **2025**, *37*, 2420383.

[25] Liu, K. Y.; Wang, L. P.; Chen, W. X.; Sun, Z. Y.; Geng, H. L.; Li, Y. Q.; Deng, Z. W.; Jiang, S.; Zhou, B. R.; Yu, K. D. et al. The roadmap of carbon-based single-atom catalysts: Rational design and electrochemical applications. *Rare Metals* **2025**, *44*, 7987–8132.

[26] Huang, S. Q.; Lin, F. M.; Wang, S. T.; Zeng, X. F.; Ling, H.; Hu, X. Y.; Shen, Z. G.; Cao, D. P. Asymmetric microenvironment tailoring strategies of atomically dispersed dual-site catalysts for oxygen reduction and CO_2 reduction reactions. *Adv. Mater.* **2024**, *36*, 2407974.

[27] Li, Y. Z.; Li, Y. J.; Sun, H.; Gao, L. Y.; Jin, X. R.; Li, Y. P.; Lv, Z.; Xu, L. J.; Liu, W.; Sun, X. M. Current status and perspectives of dual-atom catalysts towards sustainable energy utilization. *Nano-Micro Lett.* **2024**, *16*, 139.

[28] Wang, Y. C.; Wang, Q. C.; Wu, J.; Zhao, X.; Xiong, Y.; Luo, F. H.; Lei, Y. P. Asymmetric atomic sites make different: Recent progress in electrocatalytic CO_2 reduction. *Nano Energy* **2022**, *103*, 107815.

[29] Pu, T. C.; Ding, J. Q.; Zhang, F. X.; Wang, K.; Cao, N.; Hensen, E. J. M.; Xie, P. F. Dual atom catalysts for energy and environmental applications. *Angew. Chem., Int. Ed.* **2023**, *62*, e202305964.

[30] Zhong, D. C.; Wang, Y. C.; Wang, M.; Lu, T. B. Precise synthesis of dual-atom catalysts for better understanding the enhanced catalytic performance and synergistic mechanism. *Acc. Chem. Res.* **2025**, *58*, 1379–1391.

[31] Wu, J. X.; Chen, W. X.; He, C. T.; Zheng, K.; Zhuo, L. L.; Zhao, Z. H.; Zhang, J. P. Atomically dispersed dual-metal sites showing unique reactivity and dynamism for electrocatalysis. *Nano-Micro Lett.* **2023**, *15*, 120.

[32] Chen, C. L.; Sun, Z. Y.; Qin, G. Z.; Wang, B. C.; Liu, M. G.; Liang, Q. R.; Li, X. Y.; Pang, R. Z.; Guo, Y. S.; Li, Y. J. et al. Asymmetrically coordinated Cu dual-atom-sites enables selective CO_2 electroreduction to ethanol. *Adv. Mater.* **2024**, *36*, 2409797.

[33] Sun, Z. Y.; Luo, X.; Shang, H. S.; Wang, Z. D.; Zhang, L.; Chen, W. X. Atomic printing strategy achieves precise anchoring of dual-copper atoms on C_2N structure for efficient CO_2 reduction to ethylene. *Angew. Chem., Int. Ed.* **2024**, *63*, e202405778.

[34] Wang, J.; Huang, Z. Q.; Liu, W.; Chang, C. R.; Tang, H. L.; Li, Z. J.; Chen, W. X.; Jia, C. J.; Yao, T.; Wei, S. Q. et al. Design of N-coordinated dual-metal sites: A stable and active Pt-free catalyst for acidic oxygen reduction reaction. *J. Am. Chem. Soc.* **2017**, *139*, 17281–17284.

[35] Tang, J. Z.; Zeng, Z. H.; Liang, H. K.; Wang, Z. H.; Nong, W.; Yang, Z.; Qi, C. Z.; Qiao, Z. P.; Li, Y.; Wang, C. X. Simultaneously enhancing catalytic performance and increasing density of bifunctional CuN_3 active sites in dopant-free 2D C_3N_3Cu for oxygen reduction/evolution reactions. *ACS Omega* **2022**, *7*, 19794–19803.

[36] Yan, L.; Mao, Y.; Li, Y. X.; Sha, Q. H.; Sun, K.; Li, P. P.; Waterhouse, G. I. N.; Wang, Z. Y.; Tian, S. B.; Sun, X. M. Sublimation transformation synthesis of dual-atom Fe catalysts for efficient oxygen reduction reaction. *Angew. Chem., Int. Ed.* **2025**, *64*, e202413179.

[37] Wang, X. K.; Xu, L. L.; Li, C.; Zhang, C. H.; Yao, H. X.; Xu, R.; Cui, P. X.; Zheng, X. S.; Gu, M.; Lee, J. et al. Developing a class of dual atom materials for multifunctional catalytic reactions. *Nat. Commun.* **2023**, *14*, 7210.

[38] Gong, Y. N.; Cao, C. Y.; Shi, W. J.; Zhang, J. H.; Deng, J. H.; Lu, T. B.; Zhong, D. C. Modulating the electronic structures of dual-atom catalysts via coordination environment engineering for boosting CO_2 electroreduction. *Angew. Chem.* **2022**, *134*, e202215187.

[39] Qiao, B. T.; Wang, A. Q.; Yang, X. F.; Allard, L. F.; Jiang, Z.; Cui, Y. T.; Liu, J. Y.; Li, J.; Zhang, T. Single-atom catalysis of CO oxidation using Pt_1/FeO_x. *Nat. Chem.* **2011**, *3*, 634–641.

[40] Wang, J. Y.; Kang, X. X.; Chu, Z. Q.; Wu, P. F.; Chen, Z. H.; Duan, X. M.; Li, Y. M.; Huang, Q.; Guo, L. L.; Chen, W. X. et al. Machine learning driven high-throughput screening of asymmetric dinuclear cobalt for nitrate-to-ammonia reduction with near-100% selectivity. *Adv. Energy Mater.* **2026**, doi:*10.1002/aenm.202506009*.

[41] Chen, Y.; Hu, S. Q.; Nichols, F.; Bridges, F.; Kan, S. T.; He, T.; Zhang, Y.; Chen, S. W. Carbon aerogels with atomic dispersion of binary iron-cobalt sites as effective oxygen catalysts for flexible zinc-air batteries. *J. Mater. Chem. A* **2020**, *8*, 11649–11655.

[42] Zhu, X. F.; Zhang, D. T.; Chen, C. J.; Zhang, Q. R.; Liu, R. S.; Xia, Z. H.; Dai, L. M.; Amal, R.; Lu, X. Y. Harnessing the interplay of Fe–Ni atom pairs embedded in nitrogen-doped carbon for bifunctional oxygen electrocatalysis. *Nano Energy* **2020**, *71*, 104597.

[43] Sarkar, S.; Biswas, A.; Purkait, T.; Das, M.; Kamboj, N.; Dey, R. S. Unravelling the role of Fe–Mn binary active sites electrocatalyst for efficient oxygen reduction reaction and rechargeable Zn-air batteries. *Inorg. Chem.* **2020**, *59*, 5194–5205.

[44] Jiao, L.; Zhu, J. T.; Zhang, Y.; Yang, W. J.; Zhou, S. Y.; Li, A. W.; Xie, C. F.; Zheng, X. S.; Zhou, W.; Yu, S. H. et al. Non-bonding

interaction of neighboring Fe and Ni single-atom pairs on MOF-derived N-doped carbon for enhanced CO_2 electroreduction. *J. Am. Chem. Soc.* **2021**, *143*, 19417–19424.

[45] Gong, Q. F.; Wang, Y. J.; Ren, X. Z.; He, C. X.; Liu, J. H.; Zhang, Q. L. Ultra-low-loaded Ni–Fe dimer anchored to nitrogen/oxygen sites for boosting electroreduction of carbon dioxide. *ChemSusChem* **2021**, *14*, 4499–4506.

[46] Zeng, Z. P.; Gan, L. Y.; Yang, H. B.; Su, X. Z.; Gao, J. J.; Liu, W.; Matsumoto, H.; Gong, J.; Zhang, J. M.; Cai, W. Z. et al. Orbital coupling of hetero-diatomic nickel-iron site for bifunctional electrocatalysis of CO_2 reduction and oxygen evolution. *Nat. Commun.* **2021**, *12*, 4088.

[47] Song, K. X.; Feng, Y.; Zhou, X. Y.; Qin, T. T.; Zou, X.; Qi, Y. G.; Chen, Z. J.; Rao, J. C.; Wang, Z. Z.; Yue, N. L. et al. Exploiting the trade-offs of electron transfer in MOF-derived single Zn/Co atomic couples for performance-enhanced zinc-air battery. *Appl. Catal. B: Environ.* **2022**, *316*, 121591.

[48] Kong, F. P.; Si, R. T.; Chen, N.; Wang, Q.; Li, J. J.; Yin, G. P.; Gu, M.; Wang, J. J.; Liu, L. M.; Sun, X. L. Origin of hetero-nuclear Au–Co dual atoms for efficient acidic oxygen reduction. *Appl. Catal. B: Environ.* **2022**, *301*, 120782.

[49] Li, M.; Zhu, H. Y.; Yuan, Q.; Li, T. Y.; Wang, M. M.; Zhang, P.; Zhao, Y. L.; Qin, D. L.; Guo, W. Y.; Liu, B. et al. Proximity electronic effect of Ni/Co diatomic sites for synergistic promotion of electrocatalytic oxygen reduction and hydrogen evolution. *Adv. Funct. Mater.* **2023**, *33*, 2210867.

[50] Miao, Q. Y.; Chen, Z. X.; Li, X. W.; Liu, M. H.; Liu, G. J.; Yang, X. B.; Guo, Z. Y.; Yu, C. B.; Xu, Q.; Zeng, G. F. Construction of catalytic Fe_2N_5P sites in covalent organic framework-derived carbon for catalyzing the oxygen reduction reaction. *ACS Catal.* **2023**, *13*, 11127–11135.

[51] Chen, C.; Li, Y. F.; Huang, A. J.; Liu, X. R.; Li, J. Z.; Zhang, Y.; Chen, Z. Q.; Zhuang, Z. W.; Wu, Y.; Cheong, W. C. et al. Engineering molecular heterostructured catalyst for oxygen reduction reaction. *J. Am. Chem. Soc.* **2023**, *145*, 21273–21283.

[52] Sun, Z. Y.; Li, C.; Wei, Z. H.; Zhang, F.; Deng, Z. W.; Zhou, K. J.; Wang, Y.; Guo, J. H.; Yang, J. Y.; Xiang, Z. Q. et al. Sulfur-bridged asymmetric CuNi bimetallic atom sites for CO_2 reduction with high efficiency. *Adv. Mater.* **2024**, *36*, 2404665.

[53] Pei, J. J.; Yang, L.; Lin, J.; Zhang, Z. D.; Sun, Z. Y.; Wang, D. S.; Chen, W. X. Integrating host design and tailored electronic effects of yolk-shell Zn–Mn diatomic sites for efficient CO_2 electroreduction. *Angew. Chem., Int. Ed.* **2024**, *63*, e202316123.

[54] Han, H.; Lee, S.; Im, J.; Lee, M.; Lee, T.; Hyun, S. T.; Hong, J.; Seok, T.; Choo, D. Large-scale CO_2-to-CO electroconversion on highly efficient diatomic catalysts. *Chem. Eng. J.* **2024**, *479*, 147603.

[55] Chen, J. P.; Ahasan, M. R.; Oh, J. S.; Tan, J. A.; Hennessey, S.; Kaid, M. M.; El-Kaderi, H. M.; Zhou, L.; Lao, K. U.; Wang, R. G. et al. Highly efficient CO_2 electrochemical reduction on dual metal (Co–Ni)-nitrogen sites. *J. Mater. Chem. A* **2024**, *12*, 4601–4609.

[56] Hua, J. H.; Dai, Z. Q.; Cheng, K. H.; Wang, Z. L.; Shao, C. F.; Jiang, Y.; Dai, K.; Wang, L. Ag Atom induces microstrain environment around Cd sites to construct diatomic sites for almost 100% CO_2-to-CO electroreduction. *Nano Lett.* **2024**, *24*, 14363–14372.

[57] Zhang, L. L.; Zhang, N.; Shang, H. S.; Sun, Z. Y.; Wei, Z. H.; Wang, J. T.; Lei, Y. T.; Wang, X. C.; Wang, D.; Zhao, Y. F. et al. High-density asymmetric iron dual-atom sites for efficient and stable electrochemical water oxidation. *Nat. Commun.* **2024**, *15*, 9440.

[58] Li, Y. Q.; Luo, X.; Wei, Z. H.; Zhang, F.; Sun, Z. Y.; Deng, Z. W.; Zhan, Z. H.; Zhao, C. F.; Sun, Q.; Zhang, L. et al. Precisely constructing charge-asymmetric dual-atom Fe sites supported on hollow porous carbon spheres for efficient oxygen reduction. *Energy Environ. Sci.* **2024**, *17*, 4646–4657.

[59] Wang, X. C.; Zhang, N.; Guo, S. H.; Shang, H. S.; Luo, X.; Sun, Z. Y.; Wei, Z. H.; Lei, Y. T.; Zhang, L. L.; Wang, D. et al. p-d orbital hybridization induced by asymmetrical FeSn dual atom sites promotes the oxygen reduction reaction. *J. Am. Chem. Soc.* **2024**, *146*, 21357–21366.

[60] Wang, N.; Mei, R. G.; Chen, L. Q.; Yang, T.; Chen, Z. W.; Lin, X. D.; Liu, Q. X. P-bridging asymmetry diatomic catalysts sites drive efficient bifunctional oxygen electrocatalysis for zinc-air batteries. *Small* **2024**, *20*, 2400327.

[61] Tang, B.; Zhou, Y. N.; Ji, Q. Q.; Zhuang, Z. C.; Zhang, L.; Wang, C.; Hu, H. B.; Wang, H. J.; Mei, B. B.; Song, F. et al. A Janus dual-atom catalyst for electrocatalytic oxygen reduction and evolution. *Nat. Synth.* **2024**, *3*, 878–890.

[62] Sun, C. T.; Liu, Y. R.; Lv, Z. H.; Liu, R.; Wang, C. L.; Li, L. H.; Wang, J. M.; Zhang, Y.; Yang, W. X.; Wang, B. Coordination-environment regulation of atomic Co–Mn dual-sites for efficient oxygen reduction reaction. *Nano Res.* **2024**, *17*, 6841–6848.

[63] Xiao, M. L.; Zhu, J. B.; Li, S.; Li, G. R.; Liu, W. W.; Deng, Y. P.; Bai, Z. Y.; Ma, L.; Feng, M.; Wu, T. P. et al. 3d-orbital occupancy regulated Ir–Co atomic pair toward superior bifunctional oxygen electrocatalysis. *ACS Catal.* **2021**, *11*, 8837–8846.

[64] Huang, S. Q.; Qiao, Z. L.; Sun, P. P.; Qiao, K. W.; Pei, K.; Yang, L.; Xu, H. X.; Wang, S. T.; Huang, Y.; Yan, Y. S. et al. The strain induced synergistic catalysis of FeN_4 and MnN_3 dual-site catalysts for oxygen reduction in proton- /anion- exchange membrane fuel cells. *Appl. Catal. B: Environ.* **2022**, *317*, 121770.

[65] Liu, Y. R.; Yuan, S.; Sun, C. T.; Wang, C. L.; Liu, X. J.; Lv, Z. H.; Liu, R.; Meng, Y. Z.; Yang, W. X.; Feng, X. et al. Optimizing Fe-3d electron delocalization by asymmetric Fe–Cu diatomic configurations for efficient anion exchange membrane fuel cells. *Adv. Energy Mater.* **2023**, *13*, 2302719.

[66] Zhu, P.; Xiong, X.; Wang, X. L.; Ye, C. L.; Li, J. Z.; Sun, W. M.; Sun, X. H.; Jiang, J. J.; Zhuang, Z. B.; Wang, D. S. et al. Regulating the FeN_4 moiety by constructing Fe–Mo dual-metal atom sites for efficient electrochemical oxygen reduction. *Nano Lett.* **2022**, *22*, 9507–9515.

[67] He, T. W.; Puente Santiago, A. R.; Du, A. J. Atomically embedded asymmetrical dual-metal dimers on N-doped graphene for ultra-efficient nitrogen reduction reaction. *J. Catal.* **2020**, *388*, 77–83.

[68] Yang, X. B.; Li, X. W.; Liu, M. H.; Yang, S.; Xu, Q.; Zeng, G. F. Confined synthesis of dual-atoms within pores of covalent organic frameworks for oxygen reduction reaction. *Small* **2024**, *20*, 2306295.

[69] Liu, H. Q.; Huang, J. Z.; Feng, K.; Xiong, R.; Ma, S. Y.; Wang, R.; Fu, Q.; Rafique, M.; Liu, Z. G.; Han, J. C. et al. Reconstructing the coordination environment of Fe/Co dual-atom sites towards efficient oxygen electrocatalysis for Zn-air batteries. *Angew. Chem., Int. Ed.* **2025**, *64*, e202419595.

[70] Feng, M. M.; Wu, X. M.; Cheng, H. Y.; Fan, Z. H.; Li, X. C.; Cui, F. J.; Fan, S.; Dai, Y.; Lei, G. P.; He, G. H. Well-defined Fe–Cu diatomic sites for efficient catalysis of CO_2 electroreduction. *J. Mater. Chem. A* **2021**, *9*, 23817–23827.

[71] Roongcharoen, T.; Mano, P.; Jitwatanasirikul, T.; Sikam, P.; Butburee, T.; Takahashi, K.; Namuangruk, S. Theoretical insight on why N-vacancy promotes the selective CO_2 reduction to ethanol on NiMn doped graphitic carbon nitride sheets. *Appl. Surf. Sci.* **2022**, *595*, 153527.

[72] Zhang, L. B.; Feng, J. Q.; Liu, S. J.; Tan, X. X.; Wu, L. M.; Jia, S. H.; Xu, L.; Ma, X. D.; Song, X. N.; Ma, J. et al. Atomically dispersed Ni–Cu catalysts for pH-universal CO_2 electroreduction. *Adv. Mater.* **2023**, *35*, 2209590.

[73] Liu, Y.; Yang, Y.; Lin, X. N.; Lin, Y. T.; Zhuo, Z. W.; Liu, D.; Mao, J. J.; Jiang, J. The geometric-electronic coupled design of diatomic catalyst towards oxygen reduction reaction. *Nat. Commun.* **2025**, *16*, 5158.

[74] Yang, B. Y.; Chen, L.; Xue, S. L.; Sun, H.; Feng, K.; Chen, Y. F.; Zhang, X.; Xiao, L.; Qin, Y. Z.; Zhong, J. et al. Electrocatalytic CO_2 reduction to alcohols by modulating the molecular geometry and Cu coordination in bicentric copper complexes. *Nat. Commun.* **2022**, *13*, 5122.

[75] Xiao, Z. Y.; Sun, P. P.; Qiao, Z. L.; Qiao, K. W.; Xu, H. X.; Wang,

S. T.; Cao, D. P. Atomically dispersed Fe–Cu dual-site catalysts synergistically boosting oxygen reduction for hydrogen fuel cells. *Chem. Eng. J.* **2022**, *446*, 137112.

[76] Li, D. Y.; Sun, P. P.; Xu, H. X.; Yun, J.; Cao, D. P. A revised high-throughput screening model on oxygen reduction reaction over dual atom catalysts based on the axial pre-adsorption and O_2 adsorption. *Adv. Energy Mater.* **2025**, *15*, 2403524.

[77] Zhou, X. Y.; Gao, J. J.; Hu, Y. X.; Jin, Z. Y.; Hu, K. L.; Reddy, K. M.; Yuan, Q. H.; Lin, X.; Qiu, H. J. Theoretically revealed and experimentally demonstrated synergistic electronic interaction of CoFe dual-metal sites on N-doped carbon for boosting both oxygen reduction and evolution reactions. *Nano Lett.* **2022**, *22*, 3392–3399.

[78] Yang, G. G.; Zhu, J. W.; Yuan, P. F.; Hu, Y. F.; Qu, G.; Lu, B. A.; Xue, X. Y.; Yin, H. B.; Cheng, W. Z.; Cheng, J. Q. et al. Regulating Fe-spin state by atomically dispersed Mn–N in Fe–N–C catalysts with high oxygen reduction activity. *Nat. Commun.* **2021**, *12*, 1734.

[79] Zhou, X. Y.; Chu, S. F.; Jin, Z. Y.; Hu, K. L.; Liu, P.; Qiu, H. J.; Lin, X. Revealing the synergistic enhancement effect of dual metal RuFe(Co) sites for bifunctional oxygen catalysis. *ACS Materials Lett.* **2023**, *5*, 1656–1664.

[80] Zhang, Z. Y.; Dai, Y. K.; Guo, P.; Liu, B.; Xia, Y. F.; Tu, F. D.; Zhang, W. C.; Ma, M.; Liu, B.; Zhang, Y. L. et al. Noncovalent assembly strategy for efficient synthesis of dual-atom catalysts. *Adv. Funct. Mater.* **2024**, *34*, 2407128.

[81] Sui, R.; Liu, B.; Chen, C.; Tan, X.; He, C.; Xin, D. Y.; Chen, B. W.; Xu, Z. Y.; Li, J. Z.; Chen, W. X. et al. Constructing asymmetric Fe–Nb diatomic sites to enhance ORR activity and durability. *J. Am. Chem. Soc.* **2024**, *146*, 26442–26453.

[82] Du, J. N.; Han, G. K.; Zhang, W.; Li, L. F.; Yan, Y. Q.; Shi, Y. X.; Zhang, X.; Geng, L.; Wang, Z. J.; Xiong, Y. P. et al. CoIn dual-atom catalyst for hydrogen peroxide production via oxygen reduction reaction in acid. *Nat. Commun.* **2023**, *14*, 4766.

[83] Yi, J. D.; Gao, X. P.; Zhou, H.; Chen, W.; Wu, Y. E. Design of Co–Cu diatomic site catalysts for high-efficiency synergistic CO_2 electroreduction at industrial-level current density. *Angew. Chem., Int. Ed.* **2022**, *61*, e202212329.

[84] Liu, Y. R.; Li, J. X.; Lv, Z. H.; Fan, H. Y.; Dong, F. L.; Wang, C. L.; Chen, X. C.; Liu, R.; Tian, C.; Feng, X. et al. Efficient proton-exchange membrane fuel cell performance of atomic Fe sites via p-d hybridization with Al dopants. *J. Am. Chem. Soc.* **2024**, *146*, 12636–12644.

[85] Jiao, L.; Li, X. F.; Wei, W. B.; Zhou, S. H.; Han, S. G.; Ma, D. D.; Mao, Y.; Xu, Q.; Wu, X. T.; Zhu, Q. L. Hierarchically ordered porous superstructure embedded with readily accessible atomic pair sites for enhanced CO_2 electroreduction. *Appl. Catal. B: Environ.* **2023**, *330*, 122638.

[86] Kong, F. T.; Wang, M.; Huang, Y. F.; Meng, G.; Chen, M. X.; Tian, H.; Chen, Y. F.; Chen, C.; Chang, Z. W.; Cui, X. Z. et al. Cu–N-bridged Fe-3d electron state regulations for boosted oxygen reduction in flexible battery and PEMFC. *Energy Storage Mater.* **2023**, *54*, 533–542.

[87] Li, L. F.; Zhu, J. M.; Kong, F. P.; Wang, Y. J.; Kang, C.; Xu, M.; Du, C. Y.; Yin, G. P. Tailoring atomic strain environment for high-performance acidic oxygen reduction by Fe–Ru dual atoms communicative effect. *Matter* **2024**, *7*, 1517–1532.

[88] Li, Z. J.; Ji, S. Q.; Wang, C.; Liu, H. X.; Leng, L. P.; Du, L.; Gao, J. C.; Qiao, M.; Horton, J. H.; Wang, Y. Geometric and electronic engineering of atomically dispersed copper-cobalt diatomic sites for synergistic promotion of bifunctional oxygen electrocatalysis in zinc-air batteries. *Adv. Mater.* **2023**, *35*, 2300905.

[89] Wu, Y. Y.; Ye, C. C.; Yu, L.; Liu, Y. F.; Huang, J. F.; Bi, J. B.; Xue, L.; Sun, J. W.; Yang, J.; Zhang, W. Q. et al. Soft template-directed interlayer confinement synthesis of a Fe–Co dual single-atom catalyst for Zn-air batteries. *Energy Storage Mater.* **2022**, *45*, 805–813.

[90] Chen, C. L.; Sun, M. Z.; Zhang, F.; Li, H. J.; Sun, M. R.; Fang, P.; Song, T. L.; Chen, W. X.; Dong, J. C.; Rosen, B. et al. Adjacent Fe site boosts electrocatalytic oxygen evolution at Co site in single-atom-catalyst through a dual-metal-site design. *Energy Environ. Sci.* **2023**, *16*, 1685–1696.

[91] Xia, C.; Qiu, Y. R.; Xia, Y.; Zhu, P.; King, G.; Zhang, X.; Wu, Z. Y.; Kim, J. Y.; Cullen, D. A.; Zheng, D. X. et al. General synthesis of single-atom catalysts with high metal loading using graphene quantum dots. *Nat. Chem.* **2021**, *13*, 887–894.

[92] Wang, Y.; Ma, F. Y.; Zhang, G. Q.; Zhang, J. W.; Zhao, H.; Dong, Y. M.; Wang, D. S. Precise synthesis of dual atom sites for electrocatalysis. *Nano Res.* **2024**, *17*, 9397–9427.

[93] Fan, H. S.; Ma, F. X.; Liu, Z. H.; Wang, W. H.; Liu, Z. Q.; Liang, X. Y.; Du, Y.; Li, Y. Y.; Zhen, L.; Xu, C. Y. ZIF-derived N-doped carbon nanorods supporting bimetallic CoFe single-atoms/nanoclusters as bifunctional oxygen electrocatalysts for stable Zn-air batteries. *Rare Metals* **2024**, *43*, 5769–5780.

[94] Zhang, N.; Zhou, T. P.; Ge, J. K.; Lin, Y.; Du, Z. Y.; Zhong, C.; Wang, W. J.; Jiao, Q. Y.; Yuan, R. L.; Tian, Y. C. et al. High-density planar-like Fe_2N_6 structure catalyzes efficient oxygen reduction. *Matter* **2020**, *3*, 509–521.

[95] Yan, H.; Lin, Y.; Wu, H.; Zhang, W. H.; Sun, Z. H.; Cheng, H.; Liu, W.; Wang, C. L.; Li, J. J.; Huang, X. H. et al. Bottom-up precise synthesis of stable platinum dimers on graphene. *Nat. Commun.* **2017**, *8*, 1070.

[96] Lee, Y. H.; Zhang, X. Q.; Zhang, W. J.; Chang, M. T.; Lin, C. T.; Chang, K. D.; Yu, Y. C.; Wang, J. T. W.; Chang, C. S.; Li, L. J. et al. Synthesis of large-area MoS_2 atomic layers with chemical vapor deposition. *Adv. Mater.* **2012**, *24*, 2320–2325.

[97] Li, S. B.; Zhang, P.; Wang, Y. F.; Sarvari, H.; Liu, D. T.; Wu, J.; Yang, Y. J.; Wang, Z. M.; Chen, Z. D. Interface engineering of high efficiency perovskite solar cells based on ZnO nanorods using atomic layer deposition. *Nano Res.* **2017**, *10*, 1092–1103.

[98] Yan, H.; Cheng, H.; Yi, H.; Lin, Y.; Yao, T.; Wang, C. L.; Li, J. J.; Wei, S. Q.; Lu, J. L. Single-atom Pd_1/graphene catalyst achieved by atomic layer deposition: Remarkable performance in selective hydrogenation of 1, 3-butadiene. *J. Am. Chem. Soc.* **2015**, *137*, 10484–10487.

[99] Fang, Z. B.; Liu, T. T.; Liu, J. X.; Jin, S. Y.; Wu, X. P.; Gong, X. Q.; Wang, K. C.; Yin, Q.; Liu, T. F.; Cao, R. et al. Boosting interfacial charge-transfer kinetics for efficient overall CO_2 photoreduction via rational design of coordination spheres on metal-organic frameworks. *J. Am. Chem. Soc.* **2020**, *142*, 12515–12523.

[100] Gu, J.; Hsu, C. S.; Bai, L. C.; Chen, H. M.; Hu, X. L. Atomically dispersed Fe^{3+} sites catalyze efficient CO_2 electroreduction to CO. *Science* **2019**, *364*, 1091–1094.

[101] Wan, X.; Liu, X. F.; Li, Y. C.; Yu, R. H.; Zheng, L. R.; Yan, W. S.; Wang, H.; Xu, M.; Shui, J. L. Fe–N–C electrocatalyst with dense active sites and efficient mass transport for high-performance proton exchange membrane fuel cells. *Nat. Catal.* **2019**, *2*, 259–268.

[102] Zhao, C. M.; Dai, X. Y.; Yao, T.; Chen, W. X.; Wang, X. Q.; Wang, J.; Yang, J.; Wei, S. Q.; Wu, Y. E.; Li, Y. D. Ionic exchange of metal-organic frameworks to access single nickel sites for efficient electroreduction of CO_2. *J. Am. Chem. Soc.* **2017**, *139*, 8078–8081.

[103] Li, S. Y.; Huang, J.; Yan, J.; Li, S.; Liu, M. H.; Tan, H.; Zhou, H. Q.; Su, H. Electronic bridges-stabilized Fe–Cu twin-sites circumvent scaling relationship for robust acidic oxygen reduction. *ACS Catal.* **2026**, *16*, 2124–2134.

[104] Gong, Y. N.; Cao, C. Y.; Shi, W. J.; Zhang, J. H.; Deng, J. H.; Lu, T. B.; Zhong, D. C. Modulating the electronic structures of dual-atom catalysts via coordination environment engineering for boosting CO_2 electroreduction. *Angew. Chem., Int. Ed.* **2022**, *61*, e202215187.

[105] Gloag, L.; Somerville, S. V.; Gooding, J. J.; Tilley, R. D. Co-catalytic metal-support interactions in single-atom electrocatalysts. *Nat. Rev. Mater.* **2024**, *9*, 173–189.

[106] Wang, Y. Y.; Li, Z. G.; Zhang, P.; Pan, Y.; Zhang, Y.; Cai, Q.; Silva, S. R. P.; Liu, J.; Zhang, G. X.; Sun, X. M. et al. Flexible carbon

nanofiber film with diatomic Fe–Co sites for efficient oxygen reduction and evolution reactions in wearable zinc-air batteries. *Nano Energy* **2021**, *87*, 106147.

[107] Wang, Y. Y.; Kumar, A.; Ma, M.; Jia, Y.; Wang, Y.; Zhang, Y.; Zhang, G. X.; Sun, X. M.; Yan, Z. F. Hierarchical peony-like FeCo-NC with conductive network and highly active sites as efficient electrocatalyst for rechargeable Zn-air battery. *Nano Res.* **2020**, *13*, 1090–1099.

[108] Hu, C.; Xing, G. Y.; Han, W. T.; Hao, Y. X.; Zhang, C. C.; Zhang, Y.; Kuo, C. H.; Chen, H. Y.; Hu, F.; Li, L. L. et al. Inhibiting demetalation of Fe–N–C via Mn sites for efficient oxygen reduction reaction in zinc-air batteries. *Adv. Mater.* **2024**, *36*, 2405763.

[109] Chen, Z.; Liao, X. B.; Sun, C. L.; Zhao, K. N.; Ye, D. X.; Li, J. T.; Wu, G.; Fang, J. H.; Zhao, H. B.; Zhang, J. J. Enhanced performance of atomically dispersed dual-site Fe–Mn electrocatalysts through cascade reaction mechanism. *Appl. Catal. B: Environ.* **2021**, *288*, 120021.

[110] Zhang, H.; Cao, Y. J.; Sun, M.; Liu, Y.; Wang, Y.; Li, H. R.; Zhang, R. G.; Gu, X. J.; Zeng, S. H. Heterobimetallic praseodymium-nickel active sites with Pr-N_4C_2 and Ni-N_4 moieties enabling synergistic catalysis of CO_2 electroreduction. *Chem. Eng. J.* **2024**, *490*, 151706.

[111] Wang, D.; Xu, H.; Yang, P. X.; Lu, X. Y.; Ma, J. Y.; Li, R. P.; Xiao, L. H.; Zhang, J. Q.; An, M. Z. Fe-N_4 and Co-N_4 dual sites for boosting oxygen electroreduction in Zn-air batteries. *J. Mater. Chem. A* **2021**, *9*, 13678–13687.

[112] Yang, S. Y.; Luo, J.; Xu, Y. H.; Wu, M. J.; Yang, Y. K. Oxygen evolution reaction performance misjudgment caused by the self-oxidation process. *Nano Res. Energy* **2024**, *3*, e9120136.

[113] Lin, X. Y.; Du, X. W.; Wu, S. C.; Zhen, S. Y.; Liu, W.; Pei, C. L.; Zhang, P.; Zhao, Z. J.; Gong, J. L. Machine learning-assisted dual-atom sites design with interpretable descriptors unifying electrocatalytic reactions. *Nat. Commun.* **2024**, *15*, 8169.

[114] Zhang, L. H.; Bing, Q. M.; Qin, H.; Yu, L.; Li, H. B.; Deng, D. H. Artificial intelligence for catalyst design and synthesis. *Matter* **2025**, *8*, 102138.

[115] Li, X. T.; Chen, L.; Shang, C.; Liu, Z. P. *In situ* surface structures of PdAg catalyst and their influence on acetylene semihydrogenation revealed by machine learning and experiment. *J. Am. Chem. Soc.* **2021**, *143*, 6281–6292.

[116] Chen, P. C.; Tang, Z. Y.; Zeng, Z. M.; Hu, X. F.; Xiao, L. P.; Liu, Y.; Qian, X. D.; Deng, C. Y.; Huang, R. Y.; Zhang, J. Z. et al. Machine-learning-guided morphology engineering of nanoscale metal-organic frameworks. *Matter* **2020**, *2*, 1651–1666.

[117] Guo, Y.; He, X. R.; Su, Y. M.; Dai, Y. H.; Xie, M. C.; Yang, S. L.; Chen, J. W.; Wang, K.; Zhou, D.; Wang, C. Machine-learning-guided discovery and optimization of additives in preparing Cu catalysts for CO_2 reduction. *J. Am. Chem. Soc.* **2021**, *143*, 5755–5762.

[118] Jiao, D. X.; Li, X. Y.; Sun, M. Z.; Liu, L.; Fan, J. C.; Zhao, J. X.; Huang, B. L.; Cui, X. Q. Machine learning driven rational design of dual atom catalysts on graphene for carbon dioxide electroreduction. *Nano Res.* **2025**, *18*, 94907044.

[119] Chen, K.; Liang, Y. Q.; Pan, D.; Huang, J. H.; Gao, J. Y.; Lu, Z. W.; Liu, X.; Chen, J. X.; Zhang, H.; Hu, X. et al. Mass transportation facilitated porous Fe/Co dual-site catalytic cathodes for ultrahigh-power-density Al-air fuel cells. *Adv. Energy Mater.* **2025**, *15*, 2404140.

[120] Moosavi, S. M.; Jablonka, K. M.; Smit, B. The role of machine learning in the understanding and design of materials. *J. Am. Chem. Soc.* **2020**, *142*, 20273–20287.

[121] Butler, K. T.; Davies, D. W.; Cartwright, H.; Isayev, O.; Walsh, A. Machine learning for molecular and materials science. *Nature* **2018**, *559*, 547–555.

[122] Li, H. B.; Jiao, Y.; Davey, K.; Qiao, S. Z. Data-driven machine learning for understanding surface structures of heterogeneous catalysts. *Angew. Chem., Int. Ed.* **2023**, *62*, e202216383.

[123] Li, Y.; Wang, S. R.; Lv, Z.; Wang, Z. J.; Zhao, Y. B.; Xie, Y.; Xu, Y.; Qian, L.; Yang, Y. D.; Zhao, Z. Q. et al. Transforming the synthesis of carbon nanotubes with machine learning models and automation. *Matter* **2025**, *8*, 101913.

[124] Xue, X.; Sun, H. Y.; Yang, M. J.; Liu, X.; Hu, H. Y.; Deng, Y. F.; Wang, X. J. Advances in the application of artificial intelligence-based spectral data interpretation: A perspective. *Anal. Chem.* **2023**, *95*, 13733–13745.

[125] Lobato, I.; Friedrich, T.; Van Aert, S. Deep convolutional neural networks to restore single-shot electron microscopy images. *npj Comput. Mater.* **2024**, *10*, 10.

[126] Qu, J. P.; Cao, X. J.; Gao, L.; Li, J. Y.; Li, L.; Xie, Y. H.; Zhao, Y. F.; Zhang, J. Q.; Wu, M. H.; Liu, H. Electrochemical carbon dioxide reduction to ethylene: From mechanistic understanding to catalyst surface engineering. *Nano-Micro Lett.* **2023**, *15*, 178.

[127] Seh, Z. W.; Kibsgaard, J.; Dickens, C. F.; Chorkendorff, I.; Nørskov, J. K.; Jaramillo, T. F. Combining theory and experiment in electrocatalysis: Insights into materials design. *Science* **2017**, *355*, eaad4998.

[128] Wan, X. H.; Zhang, Z. F.; Niu, H.; Yin, Y. H.; Kuai, C. G.; Wang, J.; Shao, C.; Guo, Y. Z. Machine-learning-accelerated catalytic activity predictions of transition metal phthalocyanine dual-metal-site catalysts for CO_2 reduction. *J. Phys. Chem. Lett.* **2021**, *12*, 6111–6118.

[129] Zhong, M.; Tran, K.; Min, Y. M.; Wang, C. H.; Wang, Z. Y.; Dinh, C. T.; De Luna, P.; Yu, Z. Q.; Rasouli, A. S.; Brodersen, P. et al. Accelerated discovery of CO_2 electrocatalysts using active machine learning. *Nature* **2020**, *581*, 178–183.

[130] Secor, M.; Soudackov, A. V.; Hammes-Schiffer, S. Density matrix-based features as descriptors for oxygen reduction and evolution catalysts. *J. Phys. Chem. C* **2023**, *127*, 15246–15256.

[131] Xing, M. J.; Zhang, Y. J.; Li, S. Y.; He, H.; Sun, S. R. Prediction of carbon dioxide reduction catalyst using machine learning with a few-feature model: WLEDZ. *J. Phys. Chem. C* **2022**, *126*, 17025–17035.

[132] Fang, Z. L.; Li, S. Y.; Zhang, Y. J.; Wang, Y. X.; Meng, K.; Huang, C. Y.; Sun, S. R. The DFT and machine learning method accelerated the discovery of DMSCs with high ORR and OER catalytic activities. *J. Phys. Chem. Lett.* **2024**, *15*, 281–289.

[133] Wang, B. Q.; Yang, X.; Xie, C. B.; Liu, H.; Ma, C.; Zhang, Z. D.; Zhuang, Z. C.; Han, A. J.; Zhuang, Z. B.; Li, L. B. et al. A general metal ion recognition strategy to mediate dual-atomic-site catalysts. *J. Am. Chem. Soc.* **2024**, *146*, 24945–24955.

[134] Hu, S. N.; Xu, W. C.; Tian, N.; Chen, S. M.; Li, M. Y.; Shen, J. F.; Lin, J. X.; Guo, S. L.; Huang, X. Y.; Zhou, Z. Y. et al. A P–O functional group anchoring Pt–Co electrocatalyst for high-durability PEMFCs. *Energy Environ. Sci.* **2024**, *17*, 3099–3111.

[135] Yoon, A.; Bai, L. C.; Yang, F. L.; Franco, F.; Zhan, C.; Rüscher, M.; Timoshenko, J.; Pratsch, C.; Werner, S.; Jeon, H. S. et al. Revealing catalyst restructuring and composition during nitrate electroreduction through correlated operando microscopy and spectroscopy. *Nat. Mater.* **2025**, *24*, 762–769.

[136] Yang, Y.; Louisia, S.; Yu, S.; Jin, J. B.; Roh, I.; Chen, C. B.; Fonseca Guzman, M. V.; Feijóo, J.; Chen, P. C.; Wang, H. S. et al. Operando studies reveal active Cu nanograins for CO_2 electroreduction. *Nature* **2023**, *614*, 262–269.

[137] Yang, H. C.; Duan, P. F.; Zhuang, Z. C.; Luo, Y. W.; Shen, J.; Xiong, Y. L.; Liu, X. W.; Wang, D. S. Understanding the dynamic evolution of active sites among single atoms, clusters, and nanoparticles. *Adv. Mater.* **2025**, *37*, 2415265.

[138] Liu, F. L.; Zhou, J. T.; Gao, X. T.; Shi, R.; Guo, Z. X.; Tse, E. C. M.; Chen, Y. Modulating adsorption behavior by single-site Pt on RuO_2 for efficient electrosynthesis of glycolic acid from plastic wastes. *Angew. Chem., Int. Ed.* **2025**, *64*, e202422183.

[139] Chen, P. C.; Chen, C. B.; Yang, Y.; Maulana, A. L.; Jin, J. B.; Feijoo, J.; Yang, P. D. Chemical and structural evolution of AgCu catalysts in electrochemical CO_2 reduction. *J. Am. Chem. Soc.* **2023**,

145, 10116–10125.

[140] Lyu, L. L.; Hu, X.; Fan, W. Q.; Shao, B.; Wang, Q. C.; Kim, G.; Chung, J. W.; Zhou, Z.; Kang, Y. M. *Operando* hydroxylation of the Sn–Co diatomic catalyst boosting ultrastable Zn-air batteries. *Nano Lett.* **2025**, *25*, 11164–11173.

[141] Cheng, K. H.; Shen, D.; Xia, Y. P.; Dai, K.; Shao, C. F.; Jiang, Y.; Chen, Y. Operando XAFS deciphering dynamic evolution of heteronuclear Cu-Ni from atomic sites to atomic clusters for enhanced CO_2 electroreduction. *Angew. Chem., Int. Ed.* **2025**, *64*, e202508932.

[142] Jiang, Z. L.; Sun, W. M.; Shang, H. S.; Chen, W. X.; Sun, T. T.; Li, H. J.; Dong, J. C.; Zhou, J.; Li, Z.; Wang, Y. et al. Atomic interface effect of a single atom copper catalyst for enhanced oxygen reduction reactions. *Energy Environ. Sci.* **2019**, *12*, 3508–3514.

[143] Zhong, H. X.; Ly, K. H.; Wang, M. C.; Krupskaya, Y.; Han, X. C.; Zhang, J. C.; Zhang, J.; Kataev, V.; Büchner, B.; Weidinger, I. M. et al. A phthalocyanine-based layered two-dimensional conjugated metal-organic framework as a highly efficient electrocatalyst for the oxygen reduction reaction. *Angew. Chem., Int. Ed.* **2019**, *58*, 10677–10682.

[144] Zhang, Z. P.; Sun, J. T.; Wang, F.; Dai, L. M. Efficient oxygen reduction reaction (ORR) catalysts based on single iron atoms dispersed on a hierarchically structured porous carbon framework. *Angew. Chem.* **2018**, *130*, 9176–9181.

[145] Guo, H.; Zhang, P.; Huang, S. Y.; Li, M.; Sun, G. X.; Li, J. Y.; Lin, Y.; Liu, B.; Pan, Y. Achilles' heel of single atom catalysts towards practical PEMFC application: Degradation mechanisms and regulatory strategies. *Nano Res. Energy* **2025**, *4*, e9120144.

[146] Mohideen, M. M.; Radhamani, A. V.; Ramakrishna, S.; Wei, Y.; Liu, Y. Recent insights on iron based nanostructured electrocatalyst and current status of proton exchange membrane fuel cell for sustainable transport. *J. Energy Chem.* **2022**, *69*, 466–489.

[147] Cui, P. B.; Zhao, L. J.; Long, Y. D.; Dai, L. M.; Hu, C. G. Carbon-based electrocatalysts for acidic oxygen reduction reaction. *Angew. Chem., Int. Ed.* **2023**, *62*, e202218269.

[148] Kundu, A.; Kuila, T.; Murmu, N. C.; Samanta, P.; Das, S. Metal-organic framework-derived advanced oxygen electrocatalysts as air-cathodes for Zn-air batteries: Recent trends and future perspectives. *Mater. Horiz.* **2023**, *10*, 745–787.

[149] Miao, Z. P.; Li, S. Z.; Priest, C.; Wang, T. Y.; Wu, G.; Li, Q. Effective approaches for designing stable M-N_x/C oxygen-reduction catalysts for proton-exchange-membrane fuel cells. *Adv. Mater.* **2022**, *34*, 2200595.

[150] Xu, B. Y.; Zhang, Y.; Li, L. G.; Shao, Q.; Huang, X. Q. Recent progress in low-dimensional palladium-based nanostructures for electrocatalysis and beyond. *Coord. Chem. Rev.* **2022**, *459*, 214388.

[151] Hong, Y. S.; Li, L. B.; Huang, B. Y.; Tang, X. N.; Zhai, W. J.; Hu, T.; Yuan, K.; Chen, Y. W. Molecular control of carbon-based oxygen reduction electrocatalysts through metal macrocyclic complexes functionalization. *Adv. Energy Mater.* **2021**, *11*, 2100866.

[152] Zhan, F.; Hu, K. S.; Mai, J. H.; Zhang, L. S.; Zhang, Z. G.; He, H.; Liu, X. H. Recent progress of Pt-based oxygen reduction reaction catalysts for proton exchange membrane fuel cells. *Rare Metals* **2024**, *43*, 2444–2468.

[153] Jin, X. R.; Li, Y. J.; Sun, H.; Gao, X. X.; Li, J. Z.; Lü, Z.; Liu, W.; Sun, X. M. Phosphorus induced activity-enhancement of Fe-N-C catalysts for high temperature polymer electrolyte membrane fuel cells. *Nano Res.* **2023**, *16*, 6531–6536.

[154] Cheng, Y. J.; Wang, H.; Song, H. Q.; Zhang, K.; Waterhouse, G. I. N.; Chang, J. W.; Tang, Z. Y.; Lu, S. Y. Design strategies towards transition metal single atom catalysts for the oxygen reduction reaction-a review. *Nano Res. Energy* **2023**, *2*, e9120082.

[155] Li, H. Y.; Fang, L. Z.; Wang, T.; Bai, R.; Zhang, J.; Li, T.; Duan, Z. Y.; Chen, K. J.; Pan, F. P. *In situ* modulated nickel single atoms on bicontinuous porous carbon fibers and sheets networks for acidic CO_2 reduction. *Adv. Mater.* **2025**, *37*, 2416337.

[156] Wei, S. J.; Zhu, J. X.; Chen, X. B.; Yang, R. Y.; Gu, K. L.; Li, L.; Chiang, C. Y.; Mai, L.; Chen, S. H. Planar chlorination engineering induced symmetry-broken single-atom site catalyst for enhanced CO_2 electroreduction. *Nat. Commun.* **2025**, *16*, 1652.

[157] Liu, Z. Y.; Yin, H. C.; Sun, J. H.; Bai, L. L.; Li, Z.; Zhao, X. M.; Yan, X. D.; Zhao, M.; Jing, L. Q. Engineering single Cu atoms anchored via N-heterocyclic carbene in COF mesopores for modulating electron kinetics of CO_2 photoconversion. *Adv. Energy Mater.* **2024**, *14*, 2401713.

[158] Zhao, S. H.; Pan, Y. Principles of coordination structure design of single-atom catalysts in electrocatalytic oxygen reduction reaction. *Rare Metals* **2025**, *44*, 2900–2920.

[159] Gong, Y. L.; Yang, X. H.; Zhang, Y.; Li, J. Y.; Xu, L.; Li, S.; Fu, H. T.; An, X. Z. Constructing asymmetric-electron-density Pd–Zn dual-atoms on N-doped defective mesoporous carbon for electrochemical reduction of CO_2. *Chem. Eng. J.* **2024**, *500*, 156603.

[160] Krishnamoorthy, V.; Sabhapathy, P.; Raghunath, P.; Huang, C. Y.; Sabbah, A.; Hussien, M. K.; Syum, Z.; Muthusamy, S.; Lin, M. C.; Wu, H. L. et al. Synergistic electronic interaction of nitrogen coordinated Fe-Sn double-atom sites: An efficient electrocatalyst for oxygen reduction reaction. *Small Methods* **2024**, *8*, 2301674.

[161] Wang, L. L.; An, Q.; Sheng, X. L.; Mei, Z. Y.; Jing, Q.; Zhao, X. Y.; Xu, Q. J.; Duan, L. Y.; Zou, X. X.; Guo, H. Modulation of electronic spin state and construction of dual-atomic tandem reaction for enhanced pH-universal oxygen reduction. *Appl. Catal. B: Environ.* **2024**, *343*, 123509.

[162] Wang, Q. C.; Chu, B. X.; Shang, C. Y.; Shao, B.; Yang, F.; Dang, D.; Li, L.; Gu, M.; Xiao, X.; Xu, Q. Asymmetric Mn/Fe dual single-atom catalysts for pH-universal oxygen electroreduction and sustainable metal-air batteries. *Adv. Mater.* **2025**, *37*, e14343.

[163] Yuan, L. J.; Miao, Z. Y.; Sui, X. L.; Lee, C. F.; Li, Q.; Yin, M. J.; Shen, L. X.; Lu, Y. R.; Zhao, Z. G.; Liu, Y. Z. et al. Janus effect of FeCo dual atom catalyst with Co as active center in acidic oxygen reduction reaction. *Nat. Commun.* **2025**, *16*, 7198.

[164] Li, T. T.; Zhang, D.; Zhang, Y.; Yang, D. L.; Li, R. X.; Yu, F. Y.; Zhong, K. Q.; Su, X. Z.; Song, T. W.; Jiao, L. et al. A pH-dependent microkinetic modeling guided synthesis of porous dual-atom catalysts for efficient oxygen reduction in Zn-air batteries. *Energy Environ. Sci.* **2025**, *18*, 4949–4961.

[165] Lu, Z. Y.; Wang, B.; Hu, Y. F.; Liu, W.; Zhao, Y. F.; Yang, R. O.; Li, Z. P.; Luo, J.; Chi, B.; Jiang, Z. et al. An isolated zinc-cobalt atomic pair for highly active and durable oxygen reduction. *Angew. Chem., Int. Ed.* **2019**, *58*, 2622–2626.

[166] Hu, R. M.; Li, Y. C.; Zeng, Q. W.; Shang, J. X. Role of active sites in N-coordinated Fe–Co dual-metal doped graphene for oxygen reduction and evolution reactions: A theoretical insight. *Appl. Surf. Sci.* **2020**, *525*, 146588.

[167] Ma, M.; Kumar, A.; Wang, D. N.; Wang, Y. Y.; Jia, Y.; Zhang, Y.; Zhang, G. X.; Yan, Z. F.; Sun, X. M. Boosting the bifunctional oxygen electrocatalytic performance of atomically dispersed Fe site via atomic Ni neighboring. *Appl. Catal. B: Environ.* **2020**, *274*, 119091.

[168] Luo, Y.; Zhang, J.; Chen, J. W.; Chen, Y. H.; Zhang, C. Y.; Luo, Y. J.; Wang, G.; Wang, R. L. Bi-functional electrocatalysis through synergetic coupling strategy of atomically dispersed Fe and Co active sites anchored on 3D nitrogen-doped carbon sheets for Zn-air battery. *J. Catal.* **2021**, *397*, 223–232.

[169] Hu, B. T.; Huang, A. J.; Zhang, X. J.; Chen, Z.; Tu, R. Y.; Zhu, W.; Zhuang, Z. B.; Chen, C.; Peng, Q.; Li, Y. D. Atomic Co/Ni dual sites with N/P-coordination as bifunctional oxygen electrocatalyst for rechargeable zinc-air batteries. *Nano Res.* **2021**, *14*, 3482–3488.

[170] Tong, M. M.; Sun, F. F.; Xie, Y.; Wang, Y.; Yang, Y. Q.; Tian, C. G.; Wang, L.; Fu, H. G. Operando cooperated catalytic mechanism of atomically dispersed Cu-N_4 and Zn-N_4 for promoting oxygen reduction reaction. *Angew. Chem., Int. Ed.* **2021**, *60*, 14005–14012.

[171] Jose, V.; Hu, H. M.; Edison, E.; Manalastas, W.; Ren, H.;

Kidkhunthod, P.; Sreejith, S.; Jayakumar, A.; Nsanzimana, J. M. V.; Srinivasan, M. et al. Modulation of single atomic Co and Fe sites on hollow carbon nanospheres as oxygen electrodes for rechargeable Zn-air batteries. *Small Methods* **2021**, *5*, 2000751.

[172] Cao, L. J.; Wang, X. L.; Yang, C.; Lu, J. J.; Shi, X. Y.; Zhu, H. W.; Liang, H. P. Highly active Fe/Pt single-atom bifunctional electrocatalysts on biomass-derived carbon. *ACS Sustainable Chem. Eng.* **2021**, *9*, 189–196.

[173] Li, L.; Li, Y. M.; Huang, R.; Cao, X. R.; Wen, Y. H. Boosting the electrocatalytic activity of Fe-Co dual-atom catalysts for oxygen reduction reaction by ligand-modification engineering. *ChemCatChem* **2021**, *13*, 4645–4651.

[174] Li, H. X.; Wen, Y. L.; Jiang, M.; Yao, Y.; Zhou, H. H.; Huang, Z. Y.; Li, J. W.; Jiao, S. Q.; Kuang, Y. F.; Luo, S. L. Understanding of neighboring Fe-N_4-C and Co-N_4-C dual active centers for oxygen reduction reaction. *Adv. Funct. Mater.* **2021**, *31*, 2011289.

[175] Yu, D. S.; Ma, Y. C.; Hu, F.; Lin, C. C.; Li, L. L.; Chen, H. Y.; Han, X. P.; Peng, S. J. Dual-sites coordination engineering of single atom catalysts for flexible metal-air batteries. *Adv. Energy Mater.* **2021**, *11*, 2101242.

[176] Li, H. G.; Wang, J.; Qi, R. J.; Hu, Y. F.; Zhang, J.; Zhao, H. B.; Zhang, J. J.; Zhao, Y. F. Enhanced Fe 3d delocalization and moderate spin polarization in Fe Ni atomic pairs for bifunctional ORR and OER electrocatalysis. *Appl. Catal. B: Environ.* **2021**, *285*, 119778.

[177] Xu, J.; Lai, S. H.; Qi, D. F.; Hu, M.; Peng, X. Y.; Liu, Y. F.; Liu, W.; Hu, G. Z.; Xu, H.; Li, F. et al. Atomic Fe–Zn dual-metal sites for high-efficiency pH-universal oxygen reduction catalysis. *Nano Res.* **2021**, *14*, 1374–1381.

[178] Zhong, X. W.; Ye, S. L.; Tang, J.; Zhu, Y. M.; Wu, D. J.; Gu, M.; Pan, H.; Xu, B. M. Engineering Pt and Fe dual-metal single atoms anchored on nitrogen-doped carbon with high activity and durability towards oxygen reduction reaction for zinc-air battery. *Appl. Catal. B: Environ.* **2021**, *286*, 119891.

[179] Cheng, X.; Wang, Y. S.; Lu, Y.; Zheng, L. R.; Sun, S. R.; Li, H. Y.; Chen, G.; Zhang, J. J. Single-atom alloy with Pt–Co dual sites as an efficient electrocatalyst for oxygen reduction reaction. *Appl. Catal. B: Environ.* **2022**, *306*, 121112.

[180] Chen, Z. Y.; Su, X. Z.; Ding, J.; Yang, N.; Zuo, W. B.; He, Q. Y.; Wei, Z. M.; Zhang, Q.; Huang, J.; Zhai, Y. M. Boosting oxygen reduction reaction with Fe and Se dual-atom sites supported by nitrogen-doped porous carbon. *Appl. Catal. B: Environ.* **2022**, *308*, 121206.

[181] Jiang, M.; Wang, F.; Yang, F.; He, H.; Yang, J.; Zhang, W.; Luo, J. Y.; Zhang, J.; Fu, C. P. Rationalization on high-loading iron and cobalt dual metal single atoms and mechanistic insight into the oxygen reduction reaction. *Nano Energy* **2022**, *93*, 106793.

[182] Wang, Y. N.; Wan, X.; Liu, J. Y.; Li, W. W.; Li, Y. C.; Guo, X.; Liu, X. F.; Shang, J. X.; Shui, J. L. Catalysis stability enhancement of Fe/Co dual-atom site via phosphorus coordination for proton exchange membrane fuel cell. *Nano Res.* **2022**, *15*, 3082–3089.

[183] He, Y. T.; Yang, X. X.; Li, Y. S.; Liu, L. T.; Guo, S. W.; Shu, C. Y.; Liu, F.; Liu, Y. N.; Tan, Q.; Wu, G. Atomically dispersed Fe–Co dual metal sites as bifunctional oxygen electrocatalysts for rechargeable and flexible Zn-air batteries. *ACS Catal.* **2022**, *12*, 1216–1227.

[184] Cai, H. Z.; Zhang, G. H.; Zhang, X.; Chen, B. B.; Lu, Z.; Xu, H. J.; Gao, R.; Shi, C. Engineering the local coordination environment and density of FeN_4 sites by Mn cooperation for electrocatalytic oxygen reduction. *Small* **2022**, *18*, 2200911.

[185] Dai, C. C.; Yin, Q. Z.; Yang, M. S.; Li, G. C.; Lian, J. B.; Zhao, Y.; Bu, Y. F.; Hu, M. J.; Yang, S. L. Gradually anchoring N and Fe, Zn atoms on monodispersed carbon nanospheres: Their contribution to the oxygen reduction reaction under analogous structure. *Ind. Eng. Chem. Res.* **2022**, *61*, 7513–7522.

[186] Li, H. G.; Di, S. L.; Niu, P.; Wang, S. L.; Wang, J.; Li, L. A durable half-metallic diatomic catalyst for efficient oxygen reduction. *Energy Environ. Sci.* **2022**, *15*, 1601–1610.

[187] Sun, Z. G.; Zhang, H. J.; Cao, L. L.; Liu, X. K.; Wu, D.; Shen, X. Y.; Zhang, X.; Chen, Z. H.; Ru, S.; Zhu, X. Y. et al. Understanding synergistic catalysis on Cu–Se dual atom sites via operando X-ray absorption spectroscopy in oxygen reduction reaction. *Angew. Chem., Int. Ed.* **2023**, *62*, e202217719.

[188] Zhang, Y. X.; Zhang, S. B.; Huang, H. L.; Liu, X. L.; Li, B. B.; Lee, Y.; Wang, X. D.; Bai, Y.; Sun, M. Z.; Wu, Y. F. et al. General synthesis of a diatomic catalyst library via a macrocyclic precursor-mediated approach. *J. Am. Chem. Soc.* **2023**, *145*, 4819–4827.

[189] Chi, B.; Zhang, L. H.; Yang, X. X.; Zeng, Y. C.; Deng, Y. J.; Liu, M. R.; Huo, J. L.; Li, C. Z.; Zhang, X. R.; Shi, X. D. et al. Promoting ZIF-8-derived Fe-N-C oxygen reduction catalysts via Zr doping in proton exchange membrane fuel cells: Durability and activity enhancements. *ACS Catal.* **2023**, *13*, 4221–4230.

[190] Wang, Z.; Jin, X. Y.; Xu, R. J.; Yang, Z. B.; Ma, S. D.; Yan, T.; Zhu, C.; Fang, J.; Liu, Y. P.; Hwang, S. J. et al. Cooperation between dual metal atoms and nanoclusters enhances activity and stability for oxygen reduction and evolution. *ACS Nano* **2023**, *17*, 8622–8633.

[191] Niu, Z. Q.; Lu, Z. K.; Qiao, Z. L.; Xing, M. H.; Han, L. K.; Wang, S. T.; Cao, D. P. Long-range regulation of Se doping for oxygen reduction of atomically dispersed Sb catalysts for ultralow-temperature solid-state Zn-air batteries. *ACS Catal.* **2023**, *13*, 7122–7131.

[192] Zhao, Y. X.; Wen, J. H.; Li, P.; Zhang, P. F.; Wang, S. N.; Li, D. C.; Dou, J. M.; Li, Y. W.; Ma, H. Y.; Xu, L. Q. A "pre-division metal clusters" strategy to mediate efficient dual-active sites ORR catalyst for ultralong rechargeable Zn-air battery. *Angew. Chem., Int. Ed.* **2023**, *62*, e202216950.

[193] Yang, H. Z.; Huang, H.; Wang, Q.; Shang, L.; Zhang, T. R.; Wang, S. G. Fe, Cu dual-metal single atom catalyst on commercial carbon black for efficient oxygen reduction reaction. *J. Mater. Chem. A* **2023**, *11*, 6191–6197.

[194] Xia, F.; Li, B. M.; An, B. W.; Zachman, M. J.; Xie, X. H.; Liu, Y. Q.; Xu, S. C.; Saha, S.; Wu, Q.; Gao, S. Y. et al. Cooperative atomically dispersed Fe-N_4 and Sn-N_x moieties for durable and more active oxygen electroreduction in fuel cells. *J. Am. Chem. Soc.* **2024**, *146*, 33569–33578.

[195] Zhao, J. Y.; Li, P.; Fan, K. C.; Wei, W. J.; Lu, F. H.; Zhao, H. M.; Li, B.; Zong, L. B.; Wang, L. Spatial confinement of zeolitic imidazolate framework deposits by porous carbon nanospheres for dual-atom catalyst towards high-performance oxygen reduction reaction. *Nano Res.* **2023**, *16*, 11464–11472.

[196] Wang, J.; Liu, X. Y.; Zhao, C. X.; Song, Y. W.; Liu, J. N.; Li, X. Y.; Bi, C. X.; Wan, X.; Shui, J. L.; Peng, H. J. et al. A post-modification strategy to precisely construct dual-atom sites for oxygen reduction electrocatalysis. *J. Energy Chem.* **2024**, *90*, 511–517.

[197] Li, Z. T.; Zhong, X. W.; Gao, L. Y.; Hu, J. J.; Peng, W. B.; Wang, X. Z.; Zhou, G. M.; Xu, B. M. Asymmetric coordination of bimetallic Fe–Co single-atom pairs toward enhanced bifunctional activity for rechargeable zinc-air batteries. *ACS Nano* **2024**, *18*, 13006–13018.

[198] Yin, L. L.; Zhang, S.; Sun, M. Z.; Wang, S. Y.; Huang, B. L.; Du, Y. P. Non-bonding modulations between single atomic cerium and monodispersed selenium sites towards efficient oxygen reduction. *Nano Res.* **2024**, *17*, 4753–4763.

[199] Liu, T.; Chen, Y. D.; Xu, A. R.; Liu, X. K.; Liu, D.; Li, S. C.; Huang, H.; Xu, L.; Jiang, S. W.; Luo, Q. Q. et al. Regulating atomic Fe–Rh site distance for efficient oxygen reduction reaction. *Sci. China Chem.* **2024**, *67*, 1352–1359.

[200] Niu, X. D.; Wei, J.; Xu, D. Y.; Pei, J. J.; Sui, R. Charge-asymmetry Fe_1Cu single-atom alloy catalyst for efficient oxygen reduction reaction. *Nano Res.* **2024**, *17*, 4702–4710.

[201] Liu, M. X.; Li, Y.; Yang, L.; Zhao, P. C.; Li, J. S.; Tian, L. T.; Cao, D. P.; Chen, Z. W. Defect-triggered orbital hybridization in FeMn dual-atom catalysts toward sabatier-optimized oxygen reduction.

Angew. Chem., Int. Ed. **2025**, *64*, e202505268.
[202] Wang, H. X.; Tzeng, Y. K.; Ji, Y. F.; Li, Y. B.; Li, J.; Zheng, X. L.; Yang, A. K.; Liu, Y. Y.; Gong, Y. J.; Cai, L. L. et al. Synergistic enhancement of electrocatalytic CO_2 reduction to C_2 oxygenates at nitrogen-doped nanodiamonds/Cu interface. *Nat. Nanotechnol.* **2020**, *15*, 131–137.
[203] Zu, X. L.; Li, X. D.; Liu, W.; Sun, Y. F.; Xu, J. Q.; Yao, T.; Yan, W. S.; Gao, S.; Wang, C. M.; Wei, S. Q. et al. Efficient and robust carbon dioxide electroreduction enabled by atomically dispersed $Sn^{\delta+}$ sites. *Adv. Mater.* **2019**, *31*, 1808135.
[204] Zhang, S.; Fan, Q.; Xia, R.; Meyer, T. J. CO_2 reduction: From homogeneous to heterogeneous electrocatalysis. *Acc. Chem. Res.* **2020**, *53*, 255–264.
[205] Filippi, M.; Ju, W.; Möller, T.; Liang, L.; Wang, X. L.; Strasser, P. Tandem architectures for electrochemical CO_2 reduction: from coupled atomic sites to tandem electrolysers. *Nat. Nanotechnol.* **2026**, *21*, 1–14.
[206] Shen, J.; Wang, D. S. How to select heterogeneous CO_2 reduction electrocatalyst. *Nano Res. Energy* **2024**, *3*, e9120096.
[207] Zhao, Z. B.; Zhang, J. G.; Lei, M.; Lum, Y. Reviewing the impact of halides on electrochemical CO_2 reduction. *Nano Res. Energy* **2023**, *2*, e9120044.
[208] Cui, T. T.; Wang, Y. C.; Xu, R. F.; Duan, M. Y.; Yu, Y. M.; Wang, L. Q.; Li, G. J.; Han, H. M.; Wang, H. Z.; Tu, Y. C. et al. Metalloid coordination reinforcing electronic synergy in dual-atom sites for large-scale CO_2 electrolysis. *Angew. Chem., Int. Ed.* **2026**, *65*, e16353.
[209] Jiang, Z. L.; Wang, T.; Pei, J. J.; Shang, H. S.; Zhou, D. N.; Li, H. J.; Dong, J. C.; Wang, Y.; Cao, R.; Zhuang, Z. B. et al. Discovery of main group single Sb–N_4 active sites for CO_2 electroreduction to formate with high efficiency. *Energy Environ. Sci.* **2020**, *13*, 2856–2863.
[210] Liu, J. Y.; Kong, X.; Zheng, L. R.; Guo, X.; Liu, X. F.; Shui, J. L. Rare earth single-atom catalysts for nitrogen and carbon dioxide reduction. *ACS Nano* **2020**, *14*, 1093–1101.
[211] Zhang, E. H.; Wang, T.; Yu, K.; Liu, J.; Chen, W. X.; Li, A.; Rong, H. P.; Lin, R.; Ji, S. F.; Zheng, X. S. et al. Bismuth single atoms resulting from transformation of metal-organic frameworks and their use as electrocatalysts for CO_2 reduction. *J. Am. Chem. Soc.* **2019**, *141*, 16569–16573.
[212] Gandionco, K. A.; Kim, J.; Bekaert, L.; Hubin, A.; Lim, J. Single-atom catalysts for the electrochemical reduction of carbon dioxide into hydrocarbons and oxygenates. *Carbon Energy* **2024**, *6*, e410.
[213] Jiao, J. Q.; Lin, R.; Liu, S. J.; Cheong, W. C.; Zhang, C.; Chen, Z.; Pan, Y.; Tang, J. G.; Wu, K. L.; Hung, S. F. et al. Copper atom-pair catalyst anchored on alloy nanowires for selective and efficient electrochemical reduction of CO_2. *Nat. Chem.* **2019**, *11*, 222–228.
[214] Wang, C. W.; Geng, L. H.; Bi, Y. P. Highly active oxygen evolution integrating with highly selective CO_2-to-CO reduction. *Nano-Micro Lett.* **2025**, *17*, 184.
[215] Fan, Z. Z.; Luo, R. C.; Zhang, Y. X.; Zhang, B.; Zhai, P. L.; Zhang, Y. T.; Wang, C.; Gao, J. F.; Zhou, W.; Sun, L. C. et al. Oxygen-bridged indium-nickel atomic pair as dual-metal active sites enabling synergistic electrocatalytic CO_2 reduction. *Angew. Chem., Int. Ed.* **2023**, *62*, e202216326.
[216] Liu, W.; Li, H. Q.; Ou, P. F.; Mao, J.; Han, L. L.; Song, J.; Luo, J.; Xin, H. L. Isolated Cu–Sn diatomic sites for enhanced electroreduction of CO_2 to CO. *Nano Res.* **2023**, *16*, 8729–8736.
[217] Ding, J.; Li, F. H.; Zhang, J. C.; Zhang, Q.; Liu, Y. H.; Wang, W. J.; Liu, W.; Wang, B. B.; Cai, J.; Su, X. Z. et al. Circumventing CO_2 reduction scaling relations over the heteronuclear diatomic catalytic pair. *J. Am. Chem. Soc.* **2023**, *145*, 11829–11836.
[218] Ma, F. Y.; Zhang, P. F.; Zheng, X. B.; Chen, L.; Li, Y. R.; Zhuang, Z. C.; Fan, Y. M.; Jiang, P.; Zhao, H.; Zhang, J. W. et al. Steering the site distance of atomic Cu-Cu pairs by first-shell halogen coordination boosts CO_2-to-C_2 selectivity. *Angew. Chem., Int. Ed.* **2024**, *63*, e202412785.
[219] Chen, S. H.; Zheng, X. B.; Zhu, P.; Li, Y. P.; Zhuang, Z. C.; Wu, H. J.; Zhu, J. X.; Xiao, C. H.; Chen, M. Z.; Wang, P. S. et al. Copper atom pairs stabilize *OCCO dipole toward highly selective CO_2 electroreduction to C_2H_4. *Angew. Chem., Int. Ed.* **2024**, *63*, e202411591.
[220] Chen, S. H.; Ye, C. L.; Wang, Z. W.; Li, P.; Jiang, W. J.; Zhuang, Z. C.; Zhu, J. X.; Zheng, X. B.; Zaman, S.; Ou, H. H. et al. Selective CO_2 reduction to ethylene mediated by adaptive small-molecule engineering of copper-based electrocatalysts. *Angew. Chem.* **2023**, *135*, e202315621.
[221] Wang, G.; Wu, Y.; Li, Z. J.; Lou, Z. Z.; Chen, Q. Q.; Li, Y. F.; Wang, D. S.; Mao, J. J. Engineering a copper single-atom electron bridge to achieve efficient photocatalytic CO_2 conversion. *Angew. Chem., Int. Ed.* **2023**, *62*, e202218460.
[222] Zhang, R. R.; Ma, H. B.; Han, S. H.; Wu, Z. T.; Zhou, X.; Chen, Z. X.; Liu, J.; Xiao, Y. K.; Chen, W.; Loh, K. P. Dynamically stable $Cu^0Cu^{\delta+}$ pair sites based on *in situ*-exsolved Cu nanoclusters on $CaCO_3$ for efficient CO_2 electroreduction. *Angew. Chem.* **2025**, *137*, e202421860.
[223] Wang, Q.; Wei, H. H.; Liu, P.; Su, Z. X.; Gong, X. Q. Recent advances in copper-based catalysts for electrocatalytic CO_2 reduction toward multi-carbon products. *Nano Res. Energy* **2024**, *3*, e9120112.
[224] Ahmad, T.; Liu, S.; Sajid, M.; Li, K.; Ali, M.; Liu, L.; Chen, W. Electrochemical CO_2 reduction to C_{2+} products using Cu-based electrocatalysts: A review. *Nano Res. Energy* **2022**, *1*, 9120021.
[225] Li, L. L.; Hasan, I. M. U.; Farwa; He, R. N.; Peng, L. W.; Xu, N. N.; Niazi, N. K.; Zhang, J. N.; Qiao, J. L. Copper as a single metal atom based photo-, electro-, and photoelectrochemical catalyst decorated on carbon nitride surface for efficient CO_2 reduction: A review. *Nano Res. Energy* **2022**, *1*, 9120015.
[226] Cao, X. J.; He, P. L. Revealing the effect of hybrid oxide coatings on copper catalysts for CO_2 electroreduction. *Rare Metals* **2025**, *44*, 2861–2864.
[227] Yan, J. C.; Wang, F. M.; Yin, S.; Zhang, J.; Jiang, W.; Liu, G. G. Copper/metal oxide heterostructures for electrochemical carbon dioxide reduction. *Rare Metals* **2025**, *44*, 2239–2267.
[228] Qi, M. M.; Zachman, M. J.; Li, Y. X.; Zeng, Y. C.; Hwang, S.; Liang, J. S.; Lyons, M.; Zhao, Q.; Mao, Y.; Shao, Y. Y. et al. Highly dense atomic Fe–Ni dual metal sites for efficient CO_2 to CO electrolyzers at industrial current densities. *Energy Environ. Sci.* **2025**, *18*, 5643–5656.
[229] Li, B.; Ren, Y.; Wang, H. Y.; Zhu, C.; Liang, J. X.; Li, J. Importance of d-electron coupling in dual-atom catalysts for electrocatalytic CO_2 reduction reaction. *Sci. China Mater.* **2025**, *68*, 1918–1928.
[230] Yang, Y.; Zhang, W. J.; Wu, G. C.; Huang, Q.; Wen, J. H.; Wang, D. S.; Liu, M. Y. Electronic structure tuning in Cu–Co dual single atom catalysts for enhanced COOH* spillover and electrocalytic CO_2 reduction activity. *Angew. Chem., Int. Ed.* **2025**, *64*, e202504423.
[231] Yun, R. R.; Zhan, F. Y.; Wang, X. J.; Zhang, B. B.; Sheng, T.; Xin, Z. F.; Mao, J. J.; Liu, S. J.; Zheng, B. S. Design of binary Cu–Fe sites coordinated with nitrogen dispersed in the porous carbon for synergistic CO_2 electroreduction. *Small* **2021**, *17*, 2006951.
[232] Li, Y. Z.; Wei, B.; Zhu, M. H.; Chen, J. C.; Jiang, Q. K.; Yang, B.; Hou, Y.; Lei, L. C.; Li, Z. J.; Zhang, R. F. et al. Synergistic effect of atomically dispersed Ni–Zn pair sites for enhanced CO_2 electroreduction. *Adv. Mater.* **2021**, *33*, 2102212.
[233] Wu, M. F.; Ruan, Q. H.; Jiang, H. X.; Zhang, L. S.; Wang, D. K.; Zou, J. P. A co-carbonization strategy for confining ultralow-loaded Fe/Mn dual sites in hierarchically porous N-doped carbon for synergistic CO_2 electroreduction. *J. Mater. Chem. A* **2022**, *10*, 25463–25470.
[234] Hao, J. C.; Zhuang, Z. C.; Hao, J. C.; Wang, C.; Lu, S. L.; Duan, F.; Xu, F. P.; Du, M. L.; Zhu, H. Interatomic electronegativity offset dictates selectivity when catalyzing the CO_2 reduction reaction. *Adv. Energy Mater.* **2022**, *12*, 2200579.
[235] Yang, Y.; Tang, T.; Lyu, Z. H.; Zheng, L. R.; Zhang, Q. H.; Fu, J. J.;

Hu, J. S. Buffering the local pH via single-atomic Mn–N auxiliary sites to boost CO_2 electroreduction. *Chem. Sci.* **2022**, *13*, 13172–13177.

[236] Sun, K. A.; Yu, K.; Fang, J. J.; Zhuang, Z. W.; Tan, X.; Wu, Y.; Zeng, L. Y.; Zhuang, Z. B.; Pan, Y.; Chen, C. Nature-inspired design of molybdenum-selenium dual-single-atom electrocatalysts for CO_2 reduction. *Adv. Mater.* **2022**, *34*, 2206478.

[237] Zhu, J. B.; Xiao, M. L.; Ren, D. Z.; Gao, R.; Liu, X. Z.; Zhang, Z.; Luo, D.; Xing, W.; Su, D.; Yu, A. P. et al. Quasi-covalently coupled Ni–Cu atomic pair for synergistic electroreduction of CO_2. *J. Am. Chem. Soc.* **2022**, *144*, 9661–9671.

[238] Guo, Z. Y.; Zhu, H. W.; Yang, G.; Wu, A. J.; Chen, Q. H.; Yan, Z. J.; Loon Fow, K.; Do, H.; Hirst, J. D.; Wu, T. et al. Synergistic engineering of heteronuclear Ni–Ag dual-atom catalysts for high-efficiency CO_2 electroreduction with nearly 100% CO selectivity. *Chem. Eng. J.* **2023**, *476*, 146556.

[239] Hao, J. C.; Zhu, H.; Zhao, Q.; Hao, J. C.; Lu, S. L.; Wang, X. F.; Duan, F.; Du, M. L. Interatomic electron transfer promotes electroreduction CO_2-to-CO efficiency over a CuZn diatomic site. *Nano Res.* **2023**, *16*, 8863–8870.

[240] Zhao, Q.; Crespo-Otero, R.; Di Tommaso, D. The role of copper in enhancing the performance of heteronuclear diatomic catalysts for the electrochemical CO_2 conversion to C1 chemicals. *J. Energy Chem.* **2023**, *85*, 490–500.

[241] Hong, L. M.; Liu, X.; Chi, B. Z.; Xia, G. M.; Wang, H. M. Diatomic molecule catalysts toward synergistic electrocatalytic carbon dioxide reduction. *J. Mater. Chem. A* **2023**, *11*, 6321–6328.

[242] Zhang, Q. C.; Liu, D.; Zhang, Y. P.; Guo, Z. L.; Chen, M. P.; Chen, Y. Y.; Jin, B.; Song, Y. Z.; Pan, H. Insight into coupled Ni–Co dual-metal atom catalysts for efficient synergistic electrochemical CO_2 reduction. *J. Energy Chem.* **2023**, *87*, 509–517.

[243] Jiao, J. Q.; Yuan, Q.; Tan, M. J.; Han, X. Q.; Gao, M. B.; Zhang, C.; Yang, X.; Shi, Z. L.; Ma, Y. B.; Xiao, H. et al. Constructing asymmetric double-atomic sites for synergistic catalysis of electrochemical CO_2 reduction. *Nat. Commun.* **2023**, *14*, 6164.

[244] Yao, Z. B.; Cheng, H.; Xu, Y. F.; Zhan, X. Y.; Hong, S.; Tan, X. Y.; Wu, T. S.; Xiong, P.; Soo, Y. L.; Li, M. M. J. et al. Hydrogen radical-boosted electrocatalytic CO_2 reduction using Ni-partnered heteroatomic pairs. *Nat. Commun.* **2024**, *15*, 9881.

[245] Xie, F.; Wang, Z.; Kao, C. W.; Lan, J.; Lu, Y. R.; Tan, Y. W. Asymmetric local electric field induced by dual heteroatoms on copper boosts efficient CO_2 reduction over ultrawide potential window. *Angew. Chem., Int. Ed.* **2024**, *63*, e202407661.

[246] Zhu, W. J.; Zhang, L.; Liu, S. H.; Li, A.; Yuan, X. T.; Hu, C. L.; Zhang, G.; Deng, W. Y.; Zang, K. T.; Luo, J. et al. Enhanced CO_2 electroreduction on neighboring Zn/Co monomers by electronic effect. *Angew. Chem., Int. Ed.* **2020**, *59*, 12664–12668.

[247] Peng, B.; She, H.; Wei, Z. H.; Sun, Z. Y.; Deng, Z. W.; Sun, Z. T.; Chen, W. X. Sulfur-doping tunes p-*d* orbital coupling over asymmetric Zn–Sn dual-atom for boosting CO_2 electroreduction to formate. *Nat. Commun.* **2025**, *16*, 2217.

[248] Chung, D. Y.; Lopes, P. P.; Farinazzo Bergamo Dias Martins, P.; He, H. Y.; Kawaguchi, T.; Zapol, P.; You, H.; Tripkovic, D.; Strmcnik, D.; Zhu, Y. S. et al. Dynamic stability of active sites in hydr(oxy)oxides for the oxygen evolution reaction. *Nat. Energy* **2020**, *5*, 222–230.

[249] Hu, Q.; Wang, Z. Y.; Huang, X. W.; Qin, Y. J.; Yang, H. P.; Ren, X. Z.; Zhang, Q. L.; Liu, J. H.; He, C. X. A unique space confined strategy to construct defective metal oxides within porous nanofibers for electrocatalysis. *Energy Environ. Sci.* **2020**, *13*, 5097–5103.

[250] Han, J. Y.; Guan, J. Q. Multicomponent transition metal oxides and (oxy)hydroxides for oxygen evolution. *Nano Res.* **2023**, *16*, 1913–1966.

[251] Wu, H. J.; Zheng, W. Q.; Zhu, R.; Zhou, M.; Ren, X. C.; Wang, Y. H.; Cheng, C.; Zhou, H. J.; Cao, S. J. Modulating coordination structures and metal environments of MOFs-engineered electrocatalysts for water electrolysis. *Chem. Eng. J.* **2023**, *452*, 139475.

[252] Wang, C. S.; Zhang, Q.; Yan, B.; You, B.; Zheng, J. J.; Feng, L.; Zhang, C. M.; Jiang, S. H.; Chen, W.; He, S. J. Facet engineering of advanced electrocatalysts toward hydrogen/oxygen evolution reactions. *Nano-Micro Lett.* **2023**, *15*, 52.

[253] Li, J. T. Oxygen evolution reaction in energy conversion and storage: Design strategies under and beyond the energy scaling relationship. *Nano-Micro Lett.* **2022**, *14*, 112.

[254] Huang, Z. F.; Song, J. J.; Du, Y. H.; Xi, S. B.; Dou, S.; Nsanzimana, J. M. V.; Wang, C.; Xu, Z. J.; Wang, X. Chemical and structural origin of lattice oxygen oxidation in Co–Zn oxyhydroxide oxygen evolution electrocatalysts. *Nat. Energy* **2019**, *4*, 329–338.

[255] Guo, B. R.; Ding, Y. N.; Huo, H. H.; Wen, X. X.; Ren, X. Q.; Xu, P.; Li, S. W. Recent advances of transition metal basic salts for electrocatalytic oxygen evolution reaction and overall water electrolysis. *Nano-Micro Lett.* **2023**, *15*, 57.

[256] Gao, Y.; Yang, C. D.; Sun, F. L.; He, D. P.; Wang, X. Q.; Chen, J.; Zheng, X. B.; Liu, R. C.; Pan, H. G.; Wang, D. S. Ligand-tuning metallic sites in molecular complexes for efficient water oxidation. *Angew. Chem., Int. Ed.* **2025**, *64*, e202415755.

[257] Zhang, H. Y.; Zhou, H.; Wang, H.; Wang, Y. K.; Yang, X. H.; Wu, D.; Yuan, P.; He, M. S.; Wei, W. X.; Yang, T. Multihybridization for enhancing Fe–Ni bimetal electrocatalyst in water oxidation. *Adv. Energy Mater.* **2025**, *15*, 2403464.

[258] Rong, C. L.; Shen, X. J.; Wang, Y.; Thomsen, L.; Zhao, T. W.; Li, Y. B.; Lu, X. Y.; Amal, R.; Zhao, C. Electronic structure engineering of eingle-atom Ru sites via Co–N_4 sites for bifunctional pH-universal water splitting. *Adv. Mater.* **2022**, *34*, 2110103.

[259] Zhao, Y. F.; Lu, X. F.; Wu, Z. P.; Pei, Z. H.; Luan, D. Y.; Lou, X. W. Supporting trimetallic metal-organic frameworks on S/N-doped carbon macroporous fibers for highly efficient electrocatalytic oxygen evolution. *Adv. Mater.* **2023**, *35*, 2207888.

[260] Meng, H. Y.; Li, J. H.; Wu, C.; Zhang, Q.; Wang, Z.; Tang, Y.; Zou, A. Q.; Zhang, Y. M.; Ma, R.; Yu, Z. G. et al. Hydrothermal-induced cationic vacancies in NiAl hydroxide for enhanced oxygen evolution activities through optimization of e_g* band broadening. *ACS Appl. Mater. Interfaces* **2024**, *16*, 63602–63611.

[261] Tang, T. M.; Han, J. Y.; Wang, Z. L.; Niu, X. D.; Guan, J. Q. Diatomic Fe–Co catalysts synergistically catalyze oxygen evolution reaction. *Nano Res.* **2024**, *17*, 3794–3800.

[262] Liu, W. B.; Long, G. F.; Xiang, Z. P.; Ren, T. L.; Piao, J.; Wan, K.; Fu, Z. Y.; Liang, Z. X. Extremely active and robust Ir–Mn dual-atom electrocatalyst for oxygen evolution reaction by oxygen-oxygen radical coupling mechanism. *Angew. Chem.* **2024**, *136*, e202411014.

[263] Wang, Y. H.; Chen, N. N.; Du, X. Q.; Han, X. H.; Zhang, X. S. Transition metal atoms M (M = Mn, Fe, Cu, Zn) doped nickel-cobalt sulfides on the Ni foam for efficient oxygen evolution reaction and urea oxidation reaction. *J. Alloys Compd.* **2022**, *893*, 162269.

[264] Bao, Y. J.; Ru, H. F.; Wang, Y. F.; Zhang, K. X.; Yu, R. T.; Wu, Q.; Yu, A. M.; Li, D. S.; Sun, C. H.; Li, W. W. et al. Hetero MOF-on-MOF of Ni-BDC/NH_2-MIL-88B(Fe) enables efficient electrochemical seawater oxidation. *Adv. Funct. Mater.* **2024**, *34*, 2314611.

[265] Wang, Y. H.; Li, S. Q.; Hou, X.; Cui, T. T.; Zhuang, Z. C.; Zhao, Y. H.; Wang, H. Z.; Wei, W.; Xu, M.; Fu, Q. et al. Low-spin Fe^{3+} evoked by multiple defects with optimal intermediate adsorption attaining unparalleled performance in water oxidation. *Adv. Mater.* **2024**, *36*, 2412598.

[266] Ishaq, H.; Dincer, I.; Crawford, C. A review on hydrogen production and utilization: Challenges and opportunities. *Int. J. Hydrogen Energy* **2022**, *47*, 26238–26264.

[267] Zhang, C. H.; Guo, Z. W.; Tian, Y.; Yu, C. M.; Liu, K. S.; Jiang, L. Engineering electrode wettability to enhance mass transfer in hydrogen evolution reaction. *Nano Res. Energy* **2023**, *2*, e9120063.

[268] Li, Y. P.; Niu, S. W.; Liu, P. G.; Pan, R. R.; Zhang, H. K.; Ahmad,

N.; Shi, Y.; Liang, X.; Cheng, M. Y.; Chen, S. H. et al. Ruthenium nanoclusters and single atoms on α-MoC/N-doped carbon achieves low-input/input-free hydrogen evolution via decoupled/coupled hydrazine oxidation. *Angew. Chem., Int. Ed.* **2024**, *63*, e202316755.

[269] Zhou, C. A.; Ma, K.; Zhuang, Z. C.; Ran, M. L.; Shu, G. Q.; Wang, C.; Song, L.; Zheng, L. R.; Yue, H. R.; Wang, D. S. Tuning the local environment of Pt species at CNT@MO_{2-x} (M = Sn and Ce) heterointerfaces for boosted alkaline hydrogen evolution. *J. Am. Chem. Soc.* **2024**, *146*, 21453–21465.

[270] Ajmal, S.; Rasheed, A.; Sheng, W. X.; Dastgeer, G.; Nguyen, Q. A. T.; Wang, P. H.; Chen, P.; Liu, S. J.; Bui, V. Q.; Zhu, M. Z. et al. Synergetic modulation of electronic properties of cobalt oxide via "Tb" single atom for uphill urea and water electrolysis. *Adv. Mater.* **2025**, *37*, 2412173.

[271] Gou, W. K.; Sun, H. M.; Cheng, F. Y. Dual active sites engineering of electrocatalysts for alkaline hydrogen evolution. *Nano Res. Energy* **2024**, *3*, e9120121.

[272] Dubouis, N.; Grimaud, A. The hydrogen evolution reaction: From material to interfacial descriptors. *Chem. Sci.* **2019**, *10*, 9165–9181.

[273] Jiao, M. Y.; Chen, Z. P.; Wang, N. L.; Liu, L. C. DFT calculation screened CoCu and CoFe dual-atom catalysts with remarkable hydrogen evolution reaction activity. *Appl. Catal. B: Environ.* **2023**, *324*, 122244.

[274] Aggarwal, P.; Sarkar, D.; Awasthi, K.; Menezes, P. W. Functional role of single-atom catalysts in electrocatalytic hydrogen evolution: Current developments and future challenges. *Coord. Chem. Rev.* **2022**, *452*, 214289.

[275] Liu, Y. D.; Vijayakumar, P.; Liu, Q. Y.; Sakthivel, T.; Chen, F. Y.; Dai, Z. F. Shining light on anion-mixed nanocatalysts for efficient water electrolysis: Fundamentals, progress, and perspectives. *Nano-Micro Lett.* **2022**, *14*, 43.

[276] Liu, D. B.; Zhao, Y.; Wu, C. Q.; Xu, W. J.; Xi, S. B.; Chen, M. X.; Yang, L.; Zhou, Y. Z.; He, Q.; Li, X. Y. et al. Triggering electronic coupling between neighboring hetero-diatomic metal sites promotes hydrogen evolution reaction kinetics. *Nano Energy* **2022**, *98*, 107296.

[277] Li, Q.; Zhang, P.; Li, H. G.; Wang, Y.; Tang, D. S.; Li, Q.; Wu, J. B. Maximizing hydrogen evolution via Co–Ni dual atoms and nanoclusters on hierarchically ordered porous carbon framework. *Sci. China Mater.* **2024**, *67*, 3197–3205.

[278] Kumar, A.; Bui, V. Q.; Lee, J.; Wang, L. L.; Jadhav, A. R.; Liu, X. H.; Shao, X. D.; Liu, Y.; Yu, J. M.; Hwang, Y. et al. Moving beyond bimetallic-alloy to single-atom dimer atomic-interface for all-pH hydrogen evolution. *Nat. Commun.* **2021**, *12*, 6766.

[279] Zhao, X.; Li, W. P.; Cao, Y. H.; Portniagin, A.; Tang, B.; Wang, S. X.; Liu, Q.; Yu, D. Y. W.; Zhong, X. Y.; Zheng, X. R. et al. Dual-atom Co/Ni electrocatalyst anchored at the surface-modified $Ti_3C_2T_x$ MXene enables efficient hydrogen and oxygen evolution reactions. *ACS Nano* **2024**, *18*, 4256–4268.

[280] Guan, S. Y.; Liu, Y. Y.; Liu, S. L.; Zhuang, Z. C.; Shen, R. F.; Zhang, H. H.; Liang, E. J.; Fan, Y. P.; Jiang, J. C.; Liu, B. Z. et al. MXene-supported Ru–Ni: A common active site for hydrolysis, hydrogen oxidation, and hydrogenation. *Angew. Chem., Int. Ed.* **2025**, *64*, e202506869.

[281] Shen, J.; Tang, M. H.; Shi, Z. H.; Guan, S. Y.; Shi, Y. J.; Zhuang, Z. C.; Li, R. Z.; Yang, J. R.; He, D. P.; Liu, B. Z. et al. Efficient generation of negative hydrogen with bimetallic-ternary-structured catalysts for nitrobenzene hydrogenation. *Angew. Chem., Int. Ed.* **2025**, *64*, e202423626.

[282] Ma, R. Z.; Zhang, J.; Gong, J. X.; Lin, Y. X.; Zhang, J. L.; Huang, Z. Q.; Chang, C. R.; Liu, S. J.; Zhu, W.; Wang, Y. X. et al. The cooperative effects of the Rh–M dual-metal atomic pairs in formic acid oxidation. *Angew. Chem., Int. Ed.* **2025**, *64*, e202503095.

[283] Qin, Y. L.; Yu, K. D.; Wang, G.; Zhuang, Z. C.; Dou, Y. H.; Wang, D. S.; Chen, Z. B. Adjacent-ligand tuning of atomically precise Cu–Pd sites enables efficient methanol electrooxidation with a CO-Free pathway. *Angew. Chem., Int. Ed.* **2025**, *64*, e202420817.

[284] Yang, Y.; Qian, Y. M.; Li, H. J.; Zhang, Z. H.; Mu, Y. W.; Do, D.; Zhou, B.; Dong, J.; Yan, W. J.; Qin, Y. et al. O-coordinated W–Mo dual-atom catalyst for pH-universal electrocatalytic hydrogen evolution. *Sci. Adv.* **2020**, *6*, eaba6586.

[285] Zhou, Y.; Song, E. H.; Chen, W.; Segre, C. U.; Zhou, J. D.; Lin, Y. C.; Zhu, C.; Ma, R. G.; Liu, P.; Chu, S. F. et al. Dual-metal interbonding as the chemical facilitator for single-atom dispersions. *Adv. Mater.* **2020**, *32*, 2003484.

[286] Li, S. J.; Xie, W. F.; Song, Y. K.; Li, Y.; Song, Y. J.; Li, J. Z.; Shao, M. F. Integrated CoPt electrocatalyst combined with upgrading anodic reaction to boost hydrogen evolution reaction. *Chem. Eng. J.* **2022**, *437*, 135473.

[287] Zhang, L. H.; Guo, X. Y.; Zhang, S. L.; Frauenheim, T.; Huang, S. P. Hybrid double atom catalysts for hydrogen evolution reaction: A sweet marriage of metal and nonmetal. *Adv. Energy Mater.* **2024**, *14*, 2302754.

[288] Fang, W. H.; Wu, Y.; Xin, S. X.; Hu, Y.; Dang, J. Q.; Li, M.; Chen, B. Z.; Zhao, H.; Li, Z. X. Fe and Mo dual-site single-atom catalysts for high-efficiency wide-pH hydrogen evolution and alkaline overall water splitting. *Chem. Eng. J.* **2023**, *468*, 143605.

[289] Ding, X.; Jiang, R.; Wu, J. L.; Xing, M. H.; Qiao, Z. L.; Zeng, X. F.; Wang, S. T.; Cao, D. P. Ni_3N–CeO_2 heterostructure bifunctional catalysts for electrochemical water splitting. *Adv. Funct. Mater.* **2023**, *33*, 2306786.

[290] Zhang, L.; Si, R. T.; Liu, H. S.; Chen, N.; Wang, Q.; Adair, K.; Wang, Z. Q.; Chen, J. T.; Song, Z. X.; Li, J. J. et al. Atomic layer deposited Pt–Ru dual-metal dimers and identifying their active sites for hydrogen evolution reaction. *Nat. Commun.* **2019**, *10*, 4936.

[291] Liu, J. J.; Wei, Z. X.; Gong, Z. C.; Yan, M. M.; Hu, Y. F.; Zhao, S. L.; Ye, G. L.; Fei, H. L. Single-atom CoN_4 sites with elongated bonding induced by phosphorus doping for efficient H_2O_2 electrosynthesis. *Appl. Catal. B: Environ.* **2023**, *324*, 122267.